SYNTHESIS OF TITANIA, DOPED-TIO2, AND BORON NITRIDE NANOPARTICLES BY PULSED-LASER DECOMPOSITION IN LIQUID PRECURSOR SOLUTIONS

by

MUSTAFA MOHSIN MOZAEL

A dissertation submitted to the

School of Graduate Studies

Rutgers, the State University of New Jersey

In partial fulfillment of the requirements

for the degree of

Doctor of Philosophy

Graduate Program in Mechanical and Aerospace Engineering

Written under the direction of

Stephen D. Tse

and approved by

_____

_____

_____

_____

New Brunswick, New Jersey

October, 2019

ABSTRACT OF THE DISSERTATION

SYNTHESIS OF TITANIA, DOPED-TiO_2, AND BORON NITRIDE NANOPARTICLES BY PULSED-LASER DECOMPOSITION IN LIQUID PRECURSOR SOLUTIONS

By Mustafa Mohsin Mozael

Dissertation Director:

Stephen D. Tse

Titanium dioxide (TiO_2) belongs to the transition-metal oxide family and crystallographically can form several polymorphs, including anatase (tetragonal), brookite (orthorhombic), and rutile (tetragonal). In comparison with other polymorphs, anatase-TiO_2 is preferable for diverse applications because of its high electron mobility, low dielectric constant, and low density.

In this research, amorphous and far-from-stoichiometric titania nanoparticles and films are produced by a novel method of pulsed-laser decomposition of liquid titanium tetra-isopropoxide (TTIP) precursor. Nanoparticles are formed innately, whereby the submerged laser-induced plasma generates vaporized species from the TTIP solution and

are then rapidly quenched by the same surrounding (chilled) liquid precursor TTIP. Relatively-dense films are formed on glass substrates placed above the surface of the liquid TTIP by vapor transport and condensation of pyrolyzed species. Upon post-annealing at 400ºC (~ 0.3 TM) in ambient air, transformation of the amorphous non-stoichiometric titania nanoparticles into novel anatase-TiO_2 morphologies, such as layered nanotubes and onion-like nanospheres, occurs. Chemical analysis of the nanostructured particles/films show that they are rich in oxygen and carbon relative to stoichiometric TiO_2. Evidently, the amorphous-to-anatase phase transformation during heat treatment in air starts at the surfaces of the nanoparticles, irrespective of their morphologies, and propagates into the interior. In-situ reaction of trapped-in species likely yields gaseous products (e.g., CO, CH_4, H_2O) that diffuse out of the particles, leaving sufficient Ti and O to enable crystallization of anatase-TiO_2. Further annealing at 800ºC in air transforms anatatase-TiO_2 to rutile-TiO_2. Catalytic activity is examined by heterogeneous hydrogen generation from water reduction with methanol as a sacrificial agent. Decreased band-gap energy of the nanopowder, as well as increased absorbance in both the high-energy (i.e., 200 nm – 250 nm) and low energy (i.e., 340 nm – 440 nm) UV regions, when compared to that of commercial anatase, indicates that the nanopowder is more active under UV illumination because of increased ability to harness the photons for photocatalysis. Carbon content, along with the new nanocrystalline layered morphology, likely play the main roles of shifting the band gap.

To extend the light absorption edge, TiO_2 can be doped with metal (e.g., W, Mo) and non-metal (e.g., N, C, F, S) elements to augment the photo-response and visible-light

photoactivity. In this research, different ions such as tungsten, molybdenum, and vanadium are used as doping ions into the TiO_2 nanostructure. The initial results show that the doped TiO_2 nanostructure is more photocatalytically active than that of undoped TiO_2 nanopowder.

Nanostructured powders of tungsten-doped TiO_2 are synthesized by pulsed-laser ablation of a tungsten foil immersed in liquid TTIP. Interaction between the focused laser beam and the W substrate generates a submerged-plasma, where ablation of the W substrate along with decomposition of the adjacent liquid precursor combine to produce W-doped TiO_2 nanoparticles upon quenching by the surrounding un-reacted liquid precursor TTIP. The as-synthesized nanoparticles display various morphologies, including nano-sphere and nano-fiber, and occur in discrete agglomerated and aggregated forms. Whatever their morphologies, all nanoparticles have non-crystalline or amorphous structures, primarily because of rapid condensation and quenching of vaporized species from the plasma-reaction zone. Interestingly, upon subsequent heat treatment in air or oxygen, starting at ~400 ºC, transformation to the more stable anatase-TiO_2 phase occurs, but now doped with tungsten. X-ray diffraction (XRD) identifies crystallinity and phase conversion of the photocatalyst. The phase transformation with increasing temperature from anatase to rutile TiO_2 in the doped sample can be deferred in comparison to that of non-doped TiO_2. In addition, the average crystallite size of TiO_2 (about 13 nm) becomes slightly reduced by doping with W (10 nm). Preliminary results show that W-doped anatase TiO_2 exhibits a higher UV and visible photochemical activity than un-doped anatase-TiO_2.

Using the same synthesis method, molybdenum-doped and vanadium-doped-TiO_2 nanostructures are also produced. Initial results show that Mo^{6+} ions are doped into an anatase TiO_2 lattice. As the ionic radius of molybdenum (0.62 nm) and titanium (0.68 nm) are quite similar, it is much easier for Mo to occupy a lattice position of Ti instead of an interstitial position. Mo-doping in TiO_2 narrows the band gap (from 3.04 eV of TiO_2 to 2.8 eV), shifting the optical absorption more into the visible range. Interestingly, the doped nanopowder exhibits higher UV and visible photochemical activity than does un-doped anatase-TiO_2. For vanadium-doped TiO_2 samples, the results show that the unit cell volume and parameters *a* and *c* decrease in comparison to those of un-doped samples. Based on the fact that the ionic radius of V^{5+} (0.054 nm) is smaller than that of Ti^{4+} (0.068 nm), the vanadium ions can replace titanium ions in the TiO_2 lattice.

As an extension of the processing method, boron nitride (BN) nanoparticles are generated through pulsed laser ablation of boron bulk immersed in an ammonia solution. The unique conditions of high-temperature plasma reaction with rapid subsequent quenching enable metastable phase formation. Short-range ordered BN structure is produced. Upon heat-treatment at 1000ºC in an ammonia atmosphere for 2 hrs, the powder transforms to the more thermodynamically-stable BN. XRD indicates the presence of hexagonal BN (h-BN), with some cubic BN (c-BN) as well.

Acknowledgements

I would like to express my deepest gratitude to my advisor, Prof. Stephen Tse, for his outstanding guidance, caring and patience. I would like to thank my co-advisor, Prof Bernard Kear for his support and advice. I am most grateful to all my lab-mates, particularly, Dr. Gang Xiong and Dr. Zhizong Dong, for their support and suggestions. Many thanks go to Ashley Pennington and Prof. Celik for their assistance and expertise in the photocatalytic characterizations of our powder. Thank you to Nofel Wohieb, Arab Hamadi, Omar Jumaah, John Shi, and Rachel Yang, for their support.

Dedication

With a heart full of love, longing and anguish, I dedicate this thesis to my deceased Mother and father. Although our time together was curtailed, their contributions to my life will be felt forever. I would not be who I am today without the love and support of my parents.

Preface

The bulk of this thesis focuses on synthesis of TiO_2, doped-TiO_2 with different ions such as tungsten, molybdenum and vanadium, and synthesis boron nitride nanoparticles by pulsed-laser decomposition in liquid precursor solutions.

Much of the content in Chapters 4, 5, 6, is verbatim from soon to be submitted publication papers [1-3]; and the permission to include the collaborative work in my thesis has been obtained from the co-authors. In addition, other chapters contain wording similar or identical to that in the papers referenced below.

References

[1] Mustafa. Mozael, Zhizhong Dong, Ashley M. Pennington, Gang Xiong, Fuat E. Celik, Bernard H. Kear, and Stephen D. Tse " Crystalline-layered fabrication of TiO_2 nanorods and nanospheres " Manuscript prepared

[2] Mustafa. Mozael, Zhizhong Dong, Ashley M. Pennington, Fuat E. Celik, Bernard H. Kear, and Stephen D. Tse " Synthesis of Tungsten-Doped TiO_2 Nanopowders " Manuscript in preparation

[3] Mustafa. Mozael, Ashley M. Pennington, Fuat E. Celik, Bernard H. Kear, and Stephen D. Tse " Synthesis of Molybdenum- and Vanadium-Doped TiO", manuscript in preparation

List of contents

List of Tables

List of Figures

Chapter One

Background and Literature Review

Using non-renewable fossil fuels to satisfy increasing energy demand is accompanied by various environmental concerns. To address these implications, researchers have been investigating many different approaches. Photocatalysis has attracted attention because of its potential applications in environmental remediation and clean-energy production. TiO_2-based photocatalysts are favorable candidates for industrial-scale applications, because of their photoactive efficiency, stability, low cost, nonhazardous nature, and ability to be activated by solar light [1-3]. TiO_2 has been used in sundry applications including gas sensors, thermal barrier coating, biomaterials, catalysts, and catalysts supports [4-8].

1.1 Chemical Structure of TiO_2

TiO_2 belongs to the transition-metal oxide family and forms several polymorphs, such as anatase (tetragonal), brookite (orthorhombic), rutile (tetragonal), and others polymorphos [1, 9, 10]. In addition, other phases have been identified or predicted, particularly at high pressure [11, 12]

Rutile: TiO_2 rutile phase is the most stable phase. It has a tetragonal structure, with 6 atoms per unit cell, Figure 0.1. The distortion of each octahedron and the assembly patterns of octahedral chains are the main differences between the three crystal structures

(i.e., rutile, anatase, and brookite) [13]. Anatase can be considered to be built up from octahedra connected by the vertices, while in rutile, the octahedra are connected by the edges. In brookite, the octahedra are connected by both vertices and edges[3]. Thermodynamically, rutile is considered the most stable phase at all temperatures and pressures up to 60 Kbar [1]. It has been reported that the phase stability may reverse depending on the particle size. Anatase phase has been found to be more stable when the particle size is less than 11 nm; brookite becomes stable at sizes between 11-35 nm; and the rutile is stable at sizes above 35 nm [14]. This aspect is due to the surface energy effect. Anatase and brookite structures have been shown to transform to rutile phase after reaching a certain particle size [15]. As a photocatalyst, rutile phase is generally very poor. Sclafani et al [16] reported that the rutile phase could be active depending on the preparing conditions.

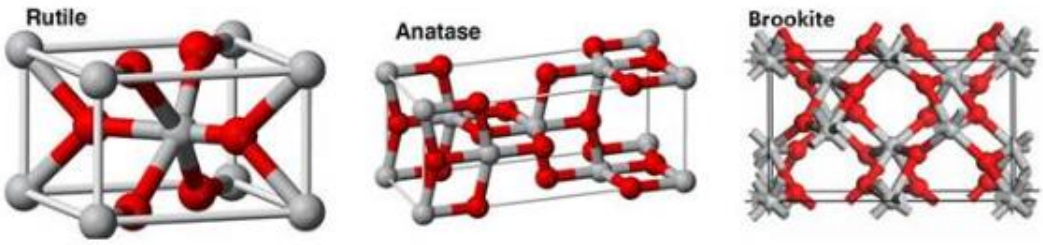

Figure 0.1. Crystal structure of the rutile, anatase, and brookite, respectively [22, 23]

Anatase: TiO_2 anatase has a tetragonal structure, Figure 0.1. Anatase TiO_2 is more stable than rutile at 0 kelvin [17]. In comparison with other polymorphs, anatase-TiO_2 is preferable for solar-cell applications because of its high electron mobility, low dielectric constant, and lower density [18]. Anatase-TiO_2 also possesses a slightly higher Fermi level,

a lower capacity to adsorb oxygen, and a higher degree of hydroxylation when compared with other phases. These properties increase the photoactivity of TiO_2 [19, 20].

Brookite: Brookite TiO_2 has an orthorhombic structure, Figure 0.1. Brookite is much lesser studied, partially because of difficulties in producing it as a pure phase [21].

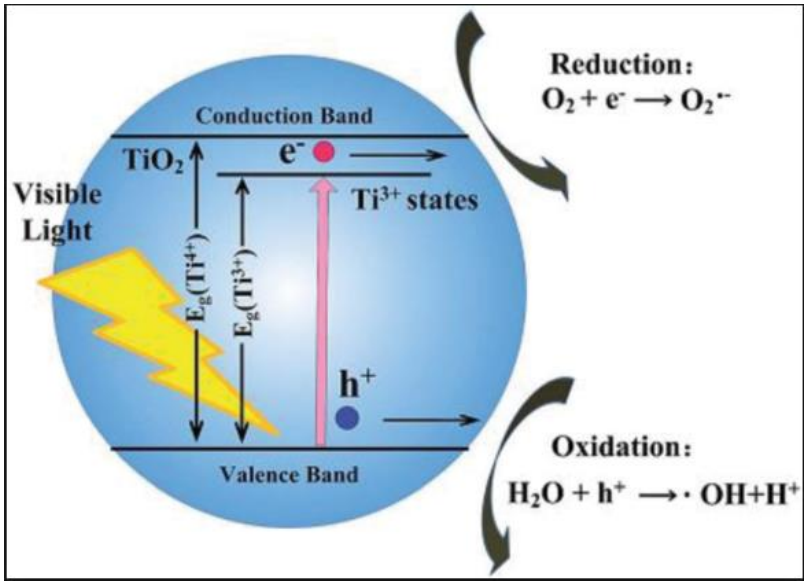

Figure 0.2. Light absorption mechanism by TiO_2 [24]

TiO_2 is a large band semiconductor, with band gaps of 3.2 eV, 3.02 eV, and 2.96 eV, for *anatase*, *rutile*, and *brookite* phases, respectively [25]. Exposure of TiO_2 to near-UV light excites electrons in the valance band to the conduction band leaving behind holes (h^+), Figure 0.2. These electrons are in a purely 3d state; and because of dissimilar parity, the transition probability of e^- to the valence band decreases, thus making the e^-/h^+ recombination decrease as well [24]. Based on charge-carrier dynamics, chemical properties,

and activity of photocatalytic degradation of organic compounds, *anatase*-TiO_2 appears to be the most active photocatalytic polymorph [26]. A mixture of *anatase* and *rutile* has been shown to enhance the effect of absorbed visible light, as compared to either of the pure phase. The photocatalytic activity decreases once the *rutile* phase is formed separately. Ohtani et al. [27] reported that there are two requirements needed to be fulfilled to achieve a high TiO_2 photocatalyst, i.e., *(i)* large surface area for absorbing and *(ii)* high crystallinity to reduce the rate of e^-/h^+ recombination.

1.2 TiO_2 Synthesis

TiO_2 has been synthesized in the form of *nanoparticles*, *nanotubes*, *thin films* and *nanorods* [28-30]. Different methods used include hydrolysis precipitation [31], sol-gel, hydrothermal [32, 33], inert gas condensation [34], and oxidation-hydrothermal synthesis of metallic Ti [35]. In all these methods, several variables must be considered, with one of the most important being particle size. Zhao et al. [36] prepared ultrafine TiO_2 nanoparticles (9-nm dia.) using a gas-flame combustion method. When particle size is several nanometers, because of very high surface-to-volume ratio, novel optical properties are expected [37].

Factors such as pH of the reaction medium, reaction temperature, natures of the solvent and additive, and reactivity of the metal alkoxide can affect the processing of TiO_2 nanostructures [32]. For example, in the sol-gel process, pH of the solution plays an important role in defining the morphology of the structure as well as the photocatalytic degradation properties. At pH above 11, the TiO_2 morphology changes from cuboidal to ellipsoidal [38, 39]. The degree of photodegradation decreases with increasing pH of the solution [40]. The

particle size distribution, as well as the phase formation, is affected by the type of solvent. Increasing the amount of acetic acid (AA) leads to the formation of brookite phase, with the particle size becoming slightly narrower [41].

In addition, various parameters, including flow rate, gas composition, deposition temperature, pressure, and deposition chamber geometry, can be controlled to have nano-forms of the desired TiO_2 material [42]. The nature of the substrates influences the size and distribution of nanograins in the films [43]. In the CVD process, it has been reported that the temperature of the substrate is a crucial parameter in the deposition of films, with increasing decomposition rate with increasing temperature. The decomposition rate of films grown at a substrate temperature of 255°C is approximately four times higher than that at 230°C [44, 45].

Pulsed-laser ablation of a liquid phase has become a successful technique for synthesizing experimental quantities of nanostructured materials with various chemistries and morphologies, including nanospheres, nanocubes, nanorods, and core-shell nanostructures. Laser ablation of solid target immersed in liquid offers some advantage in comparison to other techniques, such as chemical vapor deposition, vapor phase transport, hydrothermal synthesis, and sol-gel synthesis. These advantages include *(i)* forming phase-pure nanoparticles without by-products nor need for further purification, *(ii)* ease of experimental setup, and finally, *(iii)* unique conditions of high temperature, high pressure, and high density in the plasma-reaction zone to enable metastable phase formation.

In laser ablation in liquid (LAL), the solvent environment has a crucial role in the nature of the nanoparticles produced, as solvent components are incorporated into the

nanoparticles during formation. It has been found that titania nanoparticles formed in oxygen-rich solvents incorporate oxygen, while those formed in a carbon-rich environment are found to contain carbon [46]. TiO_2 nanoparticles prepared in DI water have a size distribution of 24.7 ± 0.2 nm, while the nanoparticles formed in methanol have smaller size distribution [47]. In addition, the conditions of the ablation affect the nanoparticle phase formation. Ablation at defocused conditions have produced anatase TiO_2 phase, while tightly focused conditions have resulted in rutile TiO_2 nanoparticles [48].

1.3 Fundamental aspects of The Laser Ablation in Liquid

Figure 0.3 shows a sequence of interactions of a pulsed laser with a solid-liquid interface [49]: *(i)* plasma initiation at the solid/liquid interface; *(ii)* plasma expansion in the confining liquid under high pressure; *(iii)* chemical reactions within the plasma and confining liquid, and (*iv*) condensation of vaporized species to form nanoparticles in the liquid and a nanostructured coating on the solid substrate.

According to Fabbro et. al [50], a laser-induced plasma under liquid confinement generates a shock wave from adiabatic expansion at supersonic velocity. This effect causes increases in pressure, temperature, and density in the plasma, which are greater than that realized under vacuum or in a gas environment. When an Al target is ablated in water, Berthe et. al [51] reported increases in pressure of 2.0-2.5 GPa.

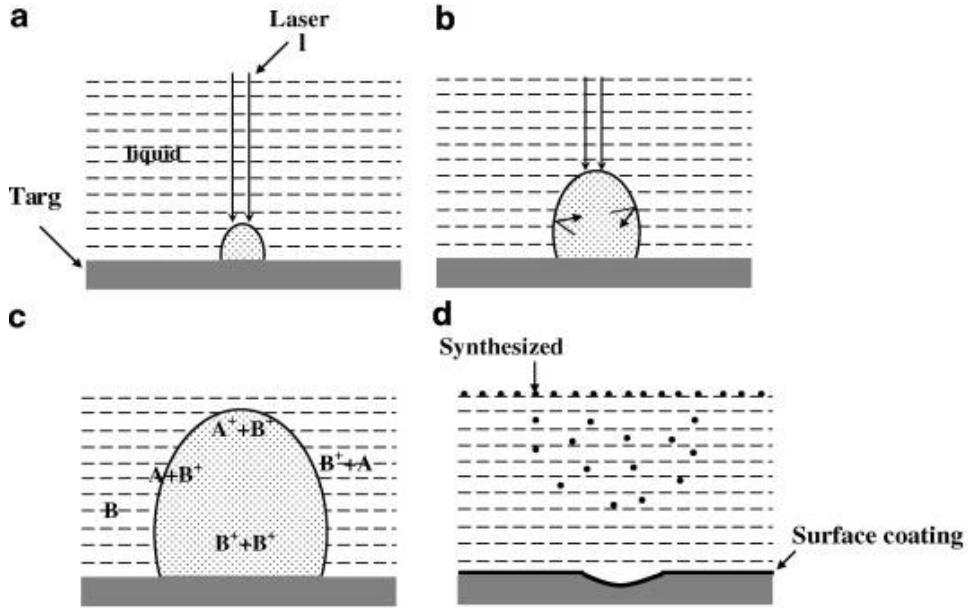

Figure 0.3. Sequence of events that occur when a pulsed laser interacts with a solid-liquid interface: (a) plasma initiation at the solid/liquid interface; (b) plasma expansion under pressure in the confining liquid; (c) chemical reactions within the plasma and confining liquid, and (d) condensation of vaporized species to form nanoparticles in the liquid, and a surface coating on the solid substrate [49]

Chemical reactions that occur in the plasma and in the liquid, and at the plasma/liquid interface are of four main types [49]:

- Reactions that occur within the plasma, forming vaporized species that experience rapid quenching to form nanoparticles with far-from-equilibrium or metastable structures;
- Reactions that occur between target and liquid species because of excitation and evaporation of the liquid molecules at the interface with the plasma;

- Reactions that occur at the interface between plasma and liquid, involving chemical reactions between ablated species from the target and molecules in the liquid;
- Reactions that occur within the liquid between ablated species and liquid molecules.

1.3.1 Thermodynamic aspects

Within the laser-induced plasma reaction zone, the relevant thermodynamic parameters are density of species, temperature, and pressure [52]. The density of species may be deduced from calculations of plasma-expansion volume and amount of ablated species. Using an Nd:YAG laser to ablate a graphite target immersed in water, the estimated density of ablated species is reported to be 6.7×10^{21} cm^{-3} [49]. The plasma temperature, determined from optical-emission spectra of ablated species is ~5000 K [53]. High pressure arises from adiabatic expansion of the plasma under liquid confinement, along with the pressure from the accompanying shock wave. Fabbro and co-workers [52] developed a theoretical model for the laser-induced pressure, obtaining a value for maximum pressure of 5.5 GPa.

1.3.2 Ablation kinetics

Laser ablation of a solid target immersed in liquid gives a higher ablation rate than that in vacuum or dilute gas. Again, because of the high pressure and high temperature experienced in laser ablation of a liquid, the plasma continuously etches the solid target, thus increasing ablation rate. Zhu et. al [54] reported differences in laser ablation rate in air and water, Figure 0.4. (a), and studied the influence of the water thickness layer on the laser ablation rate. The rate is a maximum at 1.1 mm of water-layer thickness, Figure 0.4.

(b). Kim and Lee [55] reported that the liquid layer reduces the ablation threshold, thus enhancing the ablation yield. The quenching rate for laser ablation in a liquid is much faster than that in vacuum or dilute gas because of the confining liquid. It has been observed that the plasma duration in liquids is 10 times shorter than that in air, which enables nanostructured materials with far-from-equilibrium structures to be synthesized.

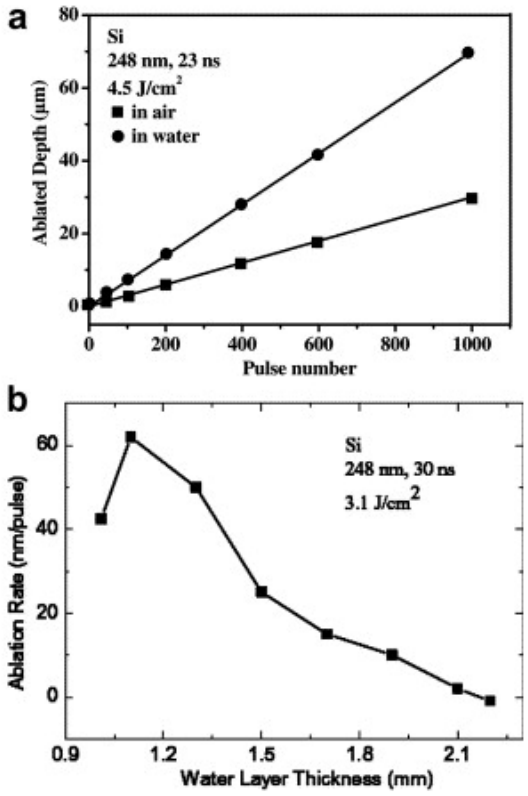

Figure 0.4. (a) Ablated depth of target surface vs laser pulse number in air and in water, and (b) laser ablation rate of Si vs water layer thickness [54]

Table 0-1. Various nanomaterials synthesized using laser ablation of solids in liquids			
Product	Solid target	Liquid solution	Laser parameters
Ag NPs	Ag	H_2O [56, 57] C_2H_5OH [58]	Nd:YAG laser (355, 532, 1064 nm) Laser energy: 90-340 mJ/pulse Cu vapor laser (510.5 nm) Laser fluence: 1-20 J/cm2
Au NPs	Au	H_2O [59]	Nd:YAG laser (532, 266 nm) Laser fluence: 5-250 J/cm2 Nd:YAG laser (532 nm) Laser fluence: 1-200 J/cm2
Cubic-BN NPs	Hexagonal-BN	Acetone [60]	Nd:YAG laser (532 nm) Power density: 1010 W/cm2
Diamond NPs	Graphite	Acetone [61] H_2O [62]	Nd:YAG laser (532 nm) Power density: 1010 W/cm2 Nd:YAG laser (532 nm) Laser energy: max 125 mJ/pulse
TiO_2 NPs	Ti	H_2O [63] H_2O +SDS [64]	Nd:YAG laser (355 nm) Laser energy: max 150 mJ/pulse
TiO_2/Ag NPs	Ti then Ag	H_2O [65]	Nd:YAG (1064 nm) Laser energy: 100 mJ/pulse
ZnO NPs ZnO/Mg NPs	Zn Zn/Mg	Water, isopropanol, and acetone [66.] Ethanol [67]	Nd:YAG (355 nm) Laser energy: 50 mJ/pulse Ti:Sapphire laser system
$Mg(OH)_2$ Tubular	Mg	H_2O +SDS [68]	Nd:YAG laser (355 nm) Laser energy: 100 mJ/pulse
SnO_2 NPs	Sn	H_2O [69]	Nd:YAG laser (355 nm) Laser energy: 180 mJ/pulse

Various nanomaterials synthesized using laser ablation of solids in liquids have been investigated by many researchers as listed in Table 0-1. In summary, laser ablation of a solid immersed in a liquid yields materials that are quite different from that formed in

vacuum or dilute gas. The plasma created at the liquid-solid interface experiences high pressure, high temperature, and high species density because of liquid confinement, affecting the four basic chemical reactions that occur in the plasma-liquid interaction zone. Subsequent high quenching rates can yield nanostructured particles and deposits with metastable structures.

1.4 Titanite Nanotubes Synthesis

Titanite nanotubes have increasingly gained scientific attention. TiO_2 nanotubes exhibit unique features that are beneficial in photocatalysis, in comparison with more commonly used TiO_2 powders. This is because the higher surface area (478 m^2/g) gives larger adsorption capacity, and pore volume up to 1.25 cm^3/g [26, 70-72]. Nanotubes also exhibit an ion-exchange ability [73], rapid and long-distance electron transport capability [74], and ability to enhance light absorption because of the high ratio of length-to-tube diameter [75]. Three main routes have been developed to synthesize TiO_2 nanotubes .

(i) Template method that helps to construct materials through adjustments in template morphology

(ii) Anodic oxidation that builds crystallized films of TiO_2 immobilized on a titanium foil surface and

(iii) Hydrothermal synthesis that allows high nanotube yields by dissolving TiO_2 or its precursor in a concentrated aqueous solution of NaOH. Table 0-2. shows the advantages and the drawbacks of these techniques.

Table 0-2. Comparison of typical rotes of synthesis TiO_2 tubes		
Synthesis method	Advantages	Drawbacks
Template method [76-78]	Nanotubes can be controlled by using different templates Useful for practical applications	Instability and high cost materials Complex fabrication process, tube morphology may be destroyed during fabrication process.
Anodic oxidation [79-81]	Eligible for extensive applications High-length-to-diameter ratio makes it favorable for practical applications	Difficulty of separate TiO_2 array from the substrate Costly and utilization of highly toxic solvent such as HF.
Hydrothermal synthesis [26, 82-84]	Easy process to fabricate nanotubes. Eligible for number of modifications. High length-to-diameter ratio	Thermal unstable Long reaction Hard to obtain uniform size and high concentrated NaOH should be added

1.5 The Effect of the Heat Treatment

Heat treatment or annealing serves an important role in the processing of particles, affecting the crystallinity, porosity, and morphology of the final product. Decrease in surface area, loss of surface hydroxyl groups, and induced phase transformation can be caused by heat treatment. Gupta and co-workers [9] reported that the removal of organic materials occur at 400 ºC. Increasing the calcination time and heating rate decreases the surface area of TiO_2 because of the collapse of pores in the TiO_2 powder as the phase transforms from amorphous to anatase. Hu et al. [85] observed that phase transformation from anatase to rutile phase starts in the temperature range of 600-700 ºC. The synthesis method, the primary particles of the anatase phase, the oxygen vacancies, and the kind of precursor used, all factor into the transformation process from anatase to rutile phase.

Different groups have reported that heat treatment has an enormous effect on the photocatalytic property of TiO_2 nanopowders. Two important factors contribute to the photocatalytic activity of TiO_2, i.e., large surface area to absorb substrates and high crystallinity to reduce the rate of photoexcited e^-/h^+ recombination [27]. Since crystallinity increases while surface area decreases with the heat treatment, a moderate heat treatment is required satisfy the two requirements. Aritonang et al. [86] proposed that TiO_2 containing both rutile and anatase phases enhance the photocatalytic activity by reducing the band gap of TiO_2. They reported that the presence of rutile nanoparticles can be set to reduce the probability of recombination of excited electrons and holes.

1.6 TiO_2 Doping

Among the many photocatalysts, TiO_2 may be close to being ideal. A shortcoming for solar applications, however, is its inability to absorb visible light [1]. Because of its large band gap, TiO_2 absorbs light in the UV portion of the solar spectrum, which is only 4% of the emission [2]. To overcome this problem, it has been proposed to shrink the band-gap energy by using doping, coupling, and capping of TiO_2 nanoparticles, all of which have been extensively studied [1].

Doping TiO_2 with various non-metal (e.g., N, C) and metal elements (e.g., Cr, V, Ag, W), Table 0-3, has been investigated to increase photocatalytic activity in the visible-light range by introducing additional energy levels in the band-gap structure of TiO_2 [3, 87, 88]. Moreover, doping improves the activity of TiO_2 photocatalysts by inhibiting electron-hole recombination, which increases the number of electrons flowing to the other electrode [88].

Furthermore, such doping enhances the surface properties of TiO_2, augmenting photocatalytic activity by increasing the surface acidity and area [89]. The presence of oxygen vacancies is also considered to be crucial to the improvement of photoactivity of TiO_2 [90]. However, the efficiency of a dopant is affected by several parameters, including concentration and distribution of the dopant in the TiO_2 matrix, creation of additional energy levels in the band-gap structure, and electron donor concentration [91]. Additionally, concentration must be closely monitored as excess dopant decreases photocatalytic activity, with charge recombination becoming favorable [92]. Xin et al. [93] reported enhanced photocatalytic activity of TiO_2 with low doping concentration of Fe and reduced activity at high concentrations.

From a chemical point of view, TiO_2 doping is equivalent to the introduction of defects sites like Ti^{3+} into the semiconductor lattice, where the oxidation of Ti^{3+} species is kinetically fast compared with the oxidation of Ti^{4+} [94]. The doping process can be achieved either by substitutional-type doping or interstitial-type doping [95, 96]. Substitutional-type doping has been reported to be effective for band gap narrowing of TiO_2 by the mixing of doped element 2p with O 2p states in the valence band [97]. Interstitial-doping type induced localizes the doped element 2p states within the band gap just above the top of the valence band, helping in the production of oxygen vacancies [98].

Table 0-3. Various ions have been doped to TiO2 in different methods	
Doped element	Preparation method
W	Chemical Vapor Deposition (CVD) by using mixture of titanium tetra-isopropoxide (TTIP) as TiO_2 precursor and tungsten (VI) isopropoxide as tungsten precursor. The mixture was transported into a heated tube furnace by using nitrogen carrier, while the oxygen gas was supplied separately [99].
N_2	Plane-wave ultrasoft pseudopotentials method based on density functional theory. Simulation finds: (i) band-gap narrowing due to high nitrogen doping; (ii) impurity-energy levels induced above the band gap by low nitrogen doping; and (iii) oxygen vacancies can be formed in nitrogen-doped TiO_2 easier than in pure TiO_2, which is important for visible activity [100].
Ca	Sol-gel method and dip-coating procedure [101]. The dopant creates some distortion in the TiO_2 lattice. Doping of TiO_2 affects the crystallinity by decreasing the intensity peaks of TiO_2 due to decrease the crystal fraction.
Fe, Cu, and Al	Sol-gel dip-coating method [102]. Metal element exists as its oxide in the nearly stoichiometric TiO_2 matrices. Photocatalytic activity of the doped nanocrystalline material shows better response by VIS-light irradiation
C	Alkoxidide precursor dissolved in corresponding alcohol, mixed with hydrochloric acid aqueous solution. [103]

1.7 Application of TiO_2 in Photocatalysis

1.7.1 Pollutant treatment in air and water

Over the last two decades, photocatalysis with TiO_2 nanoparticles has been applied in the treatment of wastes both in air and water because of their non-toxic, environmentally-friendly, high stability, and excellent photocatalytic properties [26, 72]. There are many pollutants that cannot be degraded effectively by using conventional oxidation methods. TiO_2 nanoparticles exhibit excellent properties, including complete mineralization of organic pollutant like alphatics, ploymers, dyes, and surfactants. TiO_2 photocatalysis, as a

green catalytic technology, can degrade almost all organic pollutants without selection. Studies show that more than 3,000 kinds of difficult to break down organic compounds can be degraded by TiO_2 photocatalytic technology [104]. TiO_2 nanoparticles were used to treat water contaminated with metal and organic species by Prairie et al. [105]. It has been reported that Ag^+, Cr^{6+}, Hg^{2+}, and Pt^{2+} are easy to be removed by photocatalytic reduction using 0.1 wt% TiO_2. Grandcolas and co-workers [106] proposed that WO_3-modified titanate nanotubes exhibit efficient capabilities in degradation of organo-phosphorus and organo-sulfide chemical weapon agents. Mohmoodi et al. [107] studied the photocatalytic degradation of a textile dye (Acid Blue 25) in a photocatalytic reactor containing TiO_2 nanoparticles. They found that the TiO_2 nanoparticles were able to degrade Acid Blue 25 in textile wastewater and thus help in reducing its toxicity. TNTs-CNTs exhibited excellent performance in the degradation of benzene [108]. Tang et al. [109] found that CeO_2-doped TNTs display remarkable photocatalytic activity in benzene degradation in comparison with CeO_2 nanoparticles and P25 TiO_2.

1.7.2 Hydrogen fuel production via CO_2 reduction

Since the first discovery of photocatalytic water splitting using TiO_2 by Honda-Fujioshima in 1972, photocatalytic hydrogen evolution has been one of the most popular research topics in utilizing solar energy [110]. Since hydrogen has great potential as a source of energy from the aspects of environmental preservation and energy security, H_2 should be produced from renewable resources and natural energy sources, with photocatalysis using solar energy being very attractive as a possible system to produce hydrogen from water. Solar

photoelectrolysis has been demonstrated utilizing a system in which an n-type TiO_2 semiconductor electrode was connected through an electrical load to a platinum black electrode [111]. Photocurrent flowed from the platinum counter electrode to the TiO_2 electrode when the surface of TiO_2 was irradiated with near-UV light, demonstrating that the water can be decomposed into oxygen and hydrogen without the application of external voltage.

TiO_2 nanotubes (TNTs) coupled with non-metal anion and metal cations have received much attention because of their low cost and excellent activity. Bi-doped TNTs show light absorption in the visible region, with increased yield of hydrogen production [111]. Zhang et al. [112] prepared Cr_2O_3-TNTs nanocomposites using the hydrothermal method followed by impregnation. They reported that the activity of H_2 evolution is much higher in the doped case than that using TNTs without dopant

1.7.3 Self-cleaning and Sensors

The growth of organisms, such as bacteria, algae, and fungi, in the buildings presents health and safety issues. For prevention, buildings can be coated with a layer of photocatalysis. The use of TiO_2 nanostructures for self-cleaning purposes have received considerable interest. TiO_2- coated silicon catheters was made by Sekiguchi et al. [113] to clean intermittent catheterization. These catheters were easily sterilized under sunlight. Toma et al. [114] reported the degradation of gaseous nitrogen-oxide pollutants, such as NO and NO_x, by sprayed TiO_2 coatings.

Doped and un-doped TiO_2 nanostructures have been used extensively in sensor devices. Morris et al. [115] prepared V-doped TiO_2 by a solid state reaction between mixed V_2O_5 and TiO_2 in air. They found that the changes in resistivity of polycrystalline V-doped TiO_2 upon exposure to SO_2 in air allows for application of the material as a sensor for detection of the pollutant. TiO_2 nanotubes have been used as excellent room-temperature hydrogen sensors with high sensitivity. TNTs also have the ability of self-cleaning photoactively upon environment contamination [116]. Ruiz et al. [117] reported that La-doped TiO_2 nanopowders can serve as a sensing material for ethanol. W-doped TiO_2 nanostructures have shown to be more sensitive in detecting ethanol than that for pure TiO_2 [118].

1.8 Summary and overview of the thesis

TiO_2 nanostructures have garnered attention because of their favorable photocatalytic properties. TiO_2 nanostructures can be fabricated using various methods, including the sol-gel, CVD, flame synthesis, and laser ablation. Various parameters can be adjusted to obtain different morphologies and particle sizes. Laser ablation in liquids has been proven to be a successful process for producing nanostructures with various advantageous aspects, including forming phase-pure nanoparticles without by-products, no need for further purification, ease of experimental setup, and the unique conditions of high temperature, high pressure, and high density in the plasma-reaction zone to enable amorphous or metastable phase formation.

In this thesis, chapter 3 presents formation of amorphous and non-stoichiometric titania nanoparticles and films by pulsed-laser decomposition of liquid titanium tetra-

isopropoxide (TTIP). Nanoparticles are formed in the TTIP solution, where the submerged laser-induced plasma generates vaporized species that are rapidly quenched by the surrounding (chilled) liquid precursor. Concurrently, relatively-dense films are formed on glass substrates above the surface of the liquid TTIP by vapor transport and condensation of pyrolyzed species. Upon post-annealing at 400ºC (~ 0.3 T_M) in ambient air, transformation of the amorphous titania nanoparticles occurs, producing novel anatase-TiO_2 morphologies, such as layered (nanotube-like) nanorods and (nano-onion-like) nanospheres. The influence of the heat treatment in air and nitrogen is investigated in this work.

Chapter 4 describes the synthesis of tungsten doped TiO_2 using laser ablation of tungsten foil immersed in TTIP solution. Chapter 5 discusses the effect of the doping of molybdenum and vanadium ions on the structure of TiO_2 as well as the photocatalytic activity after doping. Chapter 6 presents the synthesis BN nanoparticles through pulsed laser ablation of boron bulk immersed in an ammonia solutio

References

(1) Carp, O.; Huisman, C. L.; Reller, A., Photoinduced reactivity of titanium dioxide. *Progress in solid state chemistry* **2004,** 32, (1), 33-177.

(2) Yang, G.; Jiang, Z.; Shi, H.; Xiao, T.; Yan, Z., Preparation of highly visible-light active N-doped TiO 2 photocatalyst. *Journal of Materials Chemistry* **2010,** 20, (25), 5301-5309.

(3) Chen, X.; Mao, S. S., Titanium dioxide nanomaterials: synthesis, properties, modifications, and applications. *Chem. Rev* **2007,** 107, (7), 2891-2959.

(4) Bai, J.; Zhou, B., Titanium dioxide nanomaterials for sensor applications. *Chemical reviews* **2014,** 114, (19), 10131-10176.

(5) Peng, X.; Wang, Z.; Huang, P.; Chen, X.; Fu, X.; Dai, W., Comparative Study of Two Different TiO2 Film Sensors on Response to H2 under UV Light and Room Temperature. *Sensors* **2016,** 16, (8), 1249.

(6) Hairong, W.; Quntao, S.; Lei, C.; Bike, Z.; Yulong, Z. In *Design and fabrication of TiO 2 thin films oxygen sensors*, Manipulation, Manufacturing and Measurement on the Nanoscale (3M-NANO), 2013 International Conference on, 2013; IEEE: 2013; pp 238-242.

(7) Cui, C.; Liu, H.; Li, Y.; Sun, J.; Wang, R.; Liu, S.; Greer, A. L., Fabrication and biocompatibility of nano-TiO 2/titanium alloys biomaterials. *Materials Letters* **2005,** 59, (24), 3144-3148.

(8) Bagheri, S.; Muhd Julkapli, N.; Bee Abd Hamid, S., Titanium dioxide as a catalyst support in heterogeneous catalysis. *The Scientific World Journal* **2014,** 2014.

(9) Gupta, S. M.; Tripathi, M., A review of TiO2 nanoparticles. *Chinese Science Bulletin* **2011,** 56, (16), 1639.

(10) Cromer, D. T.; Herrington, K., The structures of anatase and rutile. *Journal of the American Chemical Society* **1955,** 77, (18), 4708-4709.

(11) Hanaor, D. A.; Sorrell, C. C., Review of the anatase to rutile phase transformation. *Journal of Materials science* **2011,** 46, (4), 855-874.

(12) Liu, Q.-J.; Ran, Z.; Liu, F.-S.; Liu, Z.-T., Phase transitions and mechanical stability of TiO 2 polymorphs under high pressure. *Journal of Alloys and Compounds* **2015,** 631, 192-201.

(13) Thompson, T. L.; Yates, J. T., Surface science studies of the photoactivation of TiO2 new photochemical processes. *Chemical Reviews* **2006,** 106, (10), 4428-4453.

(14) Zhang, H.; Banfield, J. F., Understanding polymorphic phase transformation behavior during growth of nanocrystalline aggregates: insights from TiO2. *The Journal of Physical Chemistry B* **2000,** 104, (15), 3481-3487.

(15) Zhang, Q.; Gao, L.; Guo, J., Effects of calcination on the photocatalytic properties of nanosized TiO 2 powders prepared by TiCl 4 hydrolysis. *Applied Catalysis B: Environmental* **2000,** 26, (3), 207-215.

(16) Sclafani, A.; Palmisano, L.; Schiavello, M., Influence of the preparation methods of titanium dioxide on the photocatalytic degradation of phenol in aqueous dispersion. *Journal of physical chemistry* **1990,** 94, (2), 829-832.

(17) Luo, Y.; Benali, A.; Shulenburger, L.; Krogel, J. T.; Heinonen, O.; Kent, P. R., Phase stability of TiO2 polymorphs from diffusion Quantum Monte Carlo. *New Journal of Physics* **2016,** 18, (11), 113049.

(18) Sathasivam, S.; Bhachu, D. S.; Lu, Y.; Chadwick, N.; Althabaiti, S. A.; Alyoubi, A. O.; Basahel, S. N.; Carmalt, C. J.; Parkin, I. P., Tungsten doped TiO2 with enhanced photocatalytic and optoelectrical properties via aerosol assisted chemical vapor deposition. *Scientific reports* **2015,** 5, 10952.

(19) Woan, K.; Pyrgiotakis, G.; Sigmund, W., Photocatalytic carbon-nanotube–TiO2 composites. *Advanced Materials* **2009,** 21, (21), 2233-2239.

(20) Tanaka, K.; Capule, M. F.; Hisanaga, T., Effect of crystallinity of TiO2 on its photocatalytic action. *Chemical Physics Letters* **1991,** 187, (1-2), 73-76.

(21) Di Paola, A.; Bellardita, M.; Palmisano, L., Brookite, the least known TiO2 photocatalyst. *Catalysts* **2013,** 3, (1), 36-73.

(22) Austin, R. H.; Lim, S.-f., The Sackler Colloquium on promises and perils in nanotechnology for medicine. *Proceedings of the National Academy of Sciences* **2008,** 105, (45), 17217-17221.

(23) Woodley, S.; Catlow, C., Structure prediction of titania phases: implementation of Darwinian versus Lamarckian concepts in an evolutionary algorithm. *Computational Materials Science* **2009,** 45, (1), 84-95.

(24) Huang, F.; Yan, A.; Zhao, H., Influences of Doping on Photocatalytic Properties of TiO2 Photocatalyst. In *Semiconductor Photocatalysis-Materials, Mechanisms and Applications*, InTech: 2016.

(25) Wunderlich, W.; Oekermann, T.; Miao, L.; Hue, N. T.; Tanemura, S.; Tanemura, M., ELECTRONIC PROPERTIES OF NANO-POROUS TiO 2- AND ZnO THIN FILMS-COMPARISON OF SIMULATIONS AND EXPERIMENTS. *Journal of Ceramic Processing & Research* **2004,** 5, (4), 343-354.

(26) Liu, N.; Chen, X.; Zhang, J.; Schwank, J. W., A review on TiO 2-based nanotubes synthesized via hydrothermal method: formation mechanism, structure modification, and photocatalytic applications. *Catalysis Today* **2014,** 225, 34-51.

(27) Ohtani, B.; Ogawa, Y.; Nishimoto, S.-i., Photocatalytic activity of amorphous− anatase mixture of titanium (IV) oxide particles suspended in aqueous solutions. *The Journal of Physical Chemistry B* **1997,** 101, (19), 3746-3752.

(28) Liu, B.; Aydil, E. S., Growth of oriented single-crystalline rutile TiO2 nanorods on transparent conducting substrates for dye-sensitized solar cells. *Journal of the American Chemical Society* **2009,** 131, (11), 3985-3990.
(29) Jiu, J.; Isoda, S.; Wang, F.; Adachi, M., Dye-sensitized solar cells based on a single-crystalline TiO2 nanorod film. *The Journal of Physical Chemistry B* **2006,** 110, (5), 2087-2092.
(30) Liu, S.; Gan, L.; Liu, L.; Zhang, W.; Zeng, H., Synthesis of single-crystalline TiO2 nanotubes. *Chemistry of materials* **2002,** 14, (3), 1391-1397.
(31) Ragai, J.; Lotfi, W., Effect of preparative pH and ageing media on the crystallographic transformation of amorphous TiO2 to anatase and rutile. *Colloids and surfaces* **1991,** 61, 97-109.
(32) Wang, C.-C.; Ying, J. Y., Sol− gel synthesis and hydrothermal processing of anatase and rutile titania nanocrystals. *Chemistry of Materials* **1999,** 11, (11), 3113-3120.
(33) Wang, C.; Li, Q.; Wang, R.-D., Synthesis and characterization of mesoporous TiO 2 with anatase wall. *Materials Letters* **2004,** 58, (9), 1424-1426.
(34) Siegel, R.; Ramasamy, S.; Hahn, H.; Zongquan, L.; Ting, L.; Gronsky, R., Synthesis, characterization, and properties of nanophase TiO2. *Journal of Materials Research* **1988,** 3, (6), 1367-1372.
(35) Chen, Q.; Qian, Y.; Chen, Z.; Zhou, G.; Zhang, Y., Preparation of TiO2 powders with different morphologies by an oxidation-hydrothermal combination method. *Materials Letters* **1995,** 22, (1-2), 77-80.
(36) Zhao, Y.; Li, C.; Liu, X.; Gu, F.; Jiang, H.; Shao, W.; Zhang, L.; He, Y., Synthesis and optical properties of TiO 2 nanoparticles. *Materials Letters* **2007,** 61, (1), 79-83.
(37) O'regan, B.; Grätzel, M., A low-cost, high-efficiency solar cell based on dye-sensitized colloidal TiO 2 films. *nature* **1991,** 353, (6346), 737-740.
(38) Sugimoto, T.; Zhou, X.; Muramatsu, A., Synthesis of uniform anatase TiO 2 nanoparticles by gel–sol method: 3. Formation process and size control. *Journal of colloid and interface science* **2003,** 259, (1), 43-52.
(39) Sugimoto, T.; Okada, K.; Itoh, H., Synthetic of uniform spindle-type titania particles by the gel–sol method. In ed.; Elsevier: 1997.
(40) Yang, H.; Zhang, K.; Shi, R.; Li, X.; Dong, X.; Yu, Y., Sol–gel synthesis of TiO 2 nanoparticles and photocatalytic degradation of methyl orange in aqueous TiO 2 suspensions. *Journal of Alloys and Compounds* **2006,** 413, (1), 302-306.
(41) Leyva-Porras, C.; Toxqui-Teran, A.; Vega-Becerra, O.; Miki-Yoshida, M.; Rojas-Villalobos, M.; García-Guaderrama, M.; Aguilar-Martinez, J., Low-temperature synthesis and characterization of anatase TiO 2 nanoparticles by an acid assisted sol–gel method. *Journal of Alloys and Compounds* **2015,** 647, 627-636.

(42) Malekshahi Byranvand, M.; Nemati Kharat, A.; Fatholahi, L.; Malekshahi Beiranvand, Z., A review on synthesis of nano-TiO2 via different methods. *Journal of nanostructures* **2013,** 3, (1), 1-9.
(43) Djerdj, I.; Tonejc, A. M.; Bijelić, M.; Vranes, V.; Turković, A., Transmission electron microscopy studies of nanostructured TiO 2 films on various substrates. *Vacuum* **2005,** 80, (4), 371-378.
(44) Kolouch, A.; Hájková, P.; Macková, A.; Horáková, M.; Houdková, J.; Špatenka, P.; Hucek, S., Photocatalytic TiO2 thin film prepared by PE CVD at low temperature. *Plasma Processes and Polymers* **2007,** 4, (S1).
(45) Mathur, S.; Kuhn, P., CVD of titanium oxide coatings: Comparative evaluation of thermal and plasma assisted processes. *Surface and Coatings Technology* **2006,** 201, (3), 807-814.
(46) Golightly, J. S.; Castleman, A., Analysis of titanium nanoparticles created by laser irradiation under liquid environments. *The Journal of Physical Chemistry B* **2006,** 110, (40), 19979-19984.
(47) Hong, S. M.; Lee, S.; Jung, H. J.; Yu, Y.; Shin, J. H.; Kwon, K.-Y.; Choi, M. Y., Simple preparation of anatase TiO 2 nanoparticles via pulsed laser ablation in liquid. *Bulletin of the Korean Chemical Society* **2013,** 34, (1), 279-282.
(48) Nath, A.; Laha, S.; Khare, A., Synthesis of TiO2 nanoparticles via laser ablation at titanium-water interface. *Integrated ferroelectrics* **2010,** 121, (1), 58-64.
(49) Yang, G., Laser ablation in liquids: applications in the synthesis of nanocrystals. *Progress in Materials Science* **2007,** 52, (4), 648-698.
(50) Budimlija, O. Laser synthesis of nanoparticles in liquids. Prirodoslovno-matematički fakultet, Sveučilište u Zagrebu, 2015.
(51) Berthe, L.; Sollier, A.; Peyre, P.; Fabbro, R.; Bartnicki, E., The generation of laser shock waves in a water-confinement regime with 50 ns and 150 ns XeCl excimer laser pulses. *Journal of physics D: Applied physics* **2000,** 33, (17), 2142.
(52) Berthe, L.; Fabbro, R.; Peyre, P.; Tollier, L.; Bartnicki, E., Shock waves from a water-confined laser-generated plasma. *Journal of Applied Physics* **1997,** 82, (6), 2826-2832.
(53) Kask, N. E.; Michurin, S. V.; Fedorov, G. M., Percolation upon expansion of nanosecond-pulse-produced laser plasma into a gas. *Quantum Electronics* **2005,** 35, (1), 48.
(54) Zhu, S.; Lu, Y.; Hong, M.; Chen, X., Laser ablation of solid substrates in water and ambient air. *Journal of Applied Physics* **2001,** 89, (4), 2400-2403.
(55) Kim, D.; Oh, B.; Lee, H., Effect of liquid film on near-threshold laser ablation of a solid surface. *Applied surface science* **2004,** 222, (1), 138-147.

(56) Pyatenko, A.; Shimokawa, K.; Yamaguchi, M.; Nishimura, O.; Suzuki, M., Synthesis of silver nanoparticles by laser ablation in pure water. *Applied Physics A: Materials Science & Processing* **2004,** 79, (4), 803-806.
(57) Tsuji, T.; Iryo, K.; Watanabe, N.; Tsuji, M., Preparation of silver nanoparticles by laser ablation in solution: influence of laser wavelength on particle size. *Applied Surface Science* **2002,** 202, (1), 80-85.
(58) Osorio, G. L. O.; Vargas, J. P. C.; Riascos, H. In *Study of Laser Ablation Synthesized Nanoparticles and Characterization by Nanotracking Analysis (NTA) and Scanning Electron Microscopy (SEM)*, Latin America Optics and Photonics Conference, 2016; Optical Society of America: 2016; p LW4B. 1.
(59) Tarasenko, N.; Butsen, A.; Nevar, E.; Savastenko, N., Synthesis of nanosized particles during laser ablation of gold in water. *Applied surface science* **2006,** 252, (13), 4439-4444.
(60) Wang, J.; Yang, G.; Zhang, C.; Zhong, X.; Ren, Z. A., Cubic-BN nanocrystals synthesis by pulsed laser induced liquid–solid interfacial reaction. *Chemical physics letters* **2003,** 367, (1), 10-14.
(61) Wang, J.; Zhang, C.; Zhong, X.; Yang, G., Cubic and hexagonal structures of diamond nanocrystals formed upon pulsed laser induced liquid–solid interfacial reaction. *Chemical Physics Letters* **2002,** 361, (1), 86-90.
(62) Yang, L.; May, P.; Yin, L.; Smith, J.; Rosser, K., Growth of diamond nanocrystals by pulsed laser ablation of graphite in liquid. *Diamond and Related Materials* **2007,** 16, (4), 725-729.
(63) Liang, C.; Shimizu, Y.; Sasaki, T.; Koshizaki, N., Preparation of ultrafine TiO 2 nanocrystals via pulsed-laser ablation of titanium metal in surfactant solution. *Applied Physics A: Materials Science & Processing* **2005,** 80, (4), 819-822.
(64) Liang, C.; Shimizu, Y.; Sasaki, T.; Koshizaki, N., Synthesis, characterization, and phase stability of ultrafine TiO2 nanoparticles by pulsed laser ablation in liquid media. *Journal of materials research* **2004,** 19, (5), 1551-1557.
(65) Liu, C.; Hong, M.; Zhou, Y.; Chen, G.; Saw, M.; Hor, A., Synthesis and characterization of Ag deposited TiO2 particles by laser ablation in water. *Physica Scripta* **2007,** 2007, (T129), 326.
(66) Thareja, R.; Shukla, S., Synthesis and characterization of zinc oxide nanoparticles by laser ablation of zinc in liquid. *Applied Surface Science* **2007,** 253, (22), 8889-8895.
(67) Chelnokov, E.; Rivoal, M.; Colignon, Y.; Gachet, D.; Bekere, L.; Thibaudau, F.; Giorgio, S.; Khodorkovsky, V.; Marine, W., Band gap tuning of ZnO nanoparticles via Mg doping by femtosecond laser ablation in liquid environment. *Applied Surface Science* **2012,** 258, (23), 9408-9411.

(68) Phuoc, T. X.; Howard, B. H.; Martello, D. V.; Soong, Y.; Chyu, M. K., Synthesis of Mg (OH) 2, MgO, and Mg nanoparticles using laser ablation of magnesium in water and solvents. *Optics and lasers in Engineering* **2008,** 46, (11), 829-834.
(69) Gondal, M.; Drmosh, Q.; Saleh, T., Preparation and characterization of SnO 2 nanoparticles using high power pulsed laser. *Applied Surface Science* **2010,** 256, (23), 7067-7070.
(70) Zhang, M.; Wu, J.; Lu, D.; Yang, J., Enhanced visible light photocatalytic activity for TiO2 nanotube array films by codoping with tungsten and nitrogen. *International Journal of Photoenergy* **2013,** 2013.
(71) Mozia, S.; Borowiak-Paleń, E.; Przepiórski, J.; Grzmil, B.; Tsumura, T.; Toyoda, M.; Grzechulska-Damszel, J.; Morawski, A. W., Physico-chemical properties and possible photocatalytic applications of titanate nanotubes synthesized via hydrothermal method. *Journal of Physics and Chemistry of Solids* **2010,** 71, (3), 263-272.
(72) Song, F.; Zhao, Y.; Zhong, Q., Adsorption of carbon dioxide on amine-modified TiO2 nanotubes. *Journal of Environmental Sciences* **2013,** 25, (3), 554-560.
(73) Rajeshwar, K.; Osugi, M.; Chanmanee, W.; Chenthamarakshan, C.; Zanoni, M. V. B.; Kajitvichyanukul, P.; Krishnan-Ayer, R., Heterogeneous photocatalytic treatment of organic dyes in air and aqueous media. *Journal of photochemistry and photobiology C: photochemistry reviews* **2008,** 9, (4), 171-192.
(74) Salant, A.; Shalom, M.; Hod, I.; Faust, A.; Zaban, A.; Banin, U., Quantum dot sensitized solar cells with improved efficiency prepared using electrophoretic deposition. *Acs Nano* **2010,** 4, (10), 5962-5968.
(75) Roy, P.; Berger, S.; Schmuki, P., TiO2 nanotubes: synthesis and applications. *Angewandte Chemie International Edition* **2011,** 50, (13), 2904-2939.
(76) Reyesa, M. H.; Camposeco-Solísb, R.; Ruiza, F.; Niño, N.; Martíneza, V. R. G.; Compeán–Jassoa, M., H2Ti3O7 nanotubes decorated with silver nanoparticles for photocatalytic degradation of atenolol.
(77) Kobayashi, S.; Hanabusa, K.; Hamasaki, N.; Kimura, M.; Shirai, H.; Shinkai, S., Preparation of TiO2 hollow-fibers using supramolecular assemblies. *Chemistry of materials* **2000,** 12, (6), 1523-1525.
(78) Peng, T.; Hasegawa, A.; Qiu, J.; Hirao, K., Fabrication of titania tubules with high surface area and well-developed mesostructural walls by surfactant-mediated templating method. *Chemistry of Materials* **2003,** 15, (10), 2011-2016.
(79) Albu, S. P.; Ghicov, A.; Macak, J. M.; Hahn, R.; Schmuki, P., Self-organized, free-standing TiO2 nanotube membrane for flow-through photocatalytic applications. *Nano letters* **2007,** 7, (5), 1286-1289.
(80) Tsuchiya, H.; Macak, J. M.; Ghicov, A.; Räder, A. S.; Taveira, L.; Schmuki, P., Characterization of electronic properties of TiO 2 nanotube films. *Corrosion science* **2007,** 49, (1), 203-210.

(81) Yan, J.; Zhou, F., TiO 2 nanotubes: structure optimization for solar cells. *Journal of Materials Chemistry* **2011,** 21, (26), 9406-9418.
(82) Kasuga, T.; Hiramatsu, M.; Hoson, A.; Sekino, T.; Niihara, K., Formation of titanium oxide nanotube. *Langmuir* **1998,** 14, (12), 3160-3163.
(83) Liu, S.; Zhang, N.; Tang, Z.-R.; Xu, Y.-J., Synthesis of one-dimensional CdS@ TiO2 core–shell nanocomposites photocatalyst for selective redox: the dual role of TiO2 shell. *ACS applied materials & interfaces* **2012,** 4, (11), 6378-6385.
(84) Perera, S. D.; Mariano, R. G.; Vu, K.; Nour, N.; Seitz, O.; Chabal, Y.; Balkus Jr, K. J., Hydrothermal synthesis of graphene-TiO2 nanotube composites with enhanced photocatalytic activity. *Acs Catalysis* **2012,** 2, (6), 949-956.
(85) Hu, Y.; Tsai, H.-L.; Huang, C.-L., Phase transformation of precipitated TiO 2 nanoparticles. *Materials Science and Engineering: A* **2003,** 344, (1), 209-214.
(86) Aritonang, A. B.; Surahman, H.; Krisnandi, Y. K.; Gunlazuardi, J. In *Photo-electro-catalytic performance of highly ordered nitrogen doped TiO2 nanotubes array photoanode*, IOP Conference Series: Materials Science and Engineering, 2017; IOP Publishing: 2017; p 012005.
(87) Lee, S.; Cho, I.-S.; Lee, J. H.; Kim, D. H.; Kim, D. W.; Kim, J. Y.; Shin, H.; Lee, J.-K.; Jung, H. S.; Park, N.-G., Two-step sol− gel method-based TiO2 nanoparticles with uniform morphology and size for efficient photo-energy conversion devices. *Chemistry of Materials* **2010,** 22, (6), 1958-1965.
(88) Zaleska, A., Doped-TiO2: a review. *Recent Patents on Engineering* **2008,** 2, (3), 157-164.
(89) Di Paola, A.; Garcıa-López, E.; Marcì, G.; Martín, C.; Palmisano, L.; Rives, V.; Venezia, A. M., Surface characterisation of metal ions loaded TiO 2 photocatalysts: structure–activity relationship. *Applied Catalysis B: Environmental* **2004,** 48, (3), 223-233.
(90) Martyanov, I. N.; Berger, T.; Diwald, O.; Rodrigues, S.; Klabunde, K. J., Enhancement of TiO 2 visible light photoactivity through accumulation of defects during reduction–oxidation treatment. *Journal of Photochemistry and Photobiology A: Chemistry* **2010,** 212, (2), 135-141.
(91) Choi, W.; Termin, A.; Hoffmann, M. R., The role of metal ion dopants in quantum-sized TiO2: correlation between photoreactivity and charge carrier recombination dynamics. *The Journal of Physical Chemistry* **1994,** 98, (51), 13669-13679.
(92) Zhu, J.; Deng, Z.; Chen, F.; Zhang, J.; Chen, H.; Anpo, M.; Huang, J.; Zhang, L., Hydrothermal doping method for preparation of Cr 3+-TiO 2 photocatalysts with concentration gradient distribution of Cr 3+. *Applied Catalysis B: Environmental* **2006,** 62, (3), 329-335.
(93) Fox, M. A.; Dulay, M. T., Heterogeneous photocatalysis. *Chemical reviews* **1993,** 93, (1), 341-357.

(94) Maruska, H. P.; Ghosh, A. K., Transition-metal dopants for extending the response of titanate photoelectrolysis anodes. *Solar Energy Materials* **1979,** 1, (3-4), 237-247.
(95) Wang, H.; Lewis, J. P., Effects of dopant states on photoactivity in carbon-doped TiO2. *Journal of Physics: Condensed Matter* **2005,** 17, (21), L209.
(96) Khan, S. U.; Al-Shahry, M.; Ingler, W. B., Efficient photochemical water splitting by a chemically modified n-TiO2. *science* **2002,** 297, (5590), 2243-2245.
(97) Asahi, R.; Morikawa, T.; Ohwaki, T.; Aoki, K.; Taga, Y., Visible-light photocatalysis in nitrogen-doped titanium oxides. *science* **2001,** 293, (5528), 269-271.
(98) Irie, H.; Watanabe, Y.; Hashimoto, K., Nitrogen-concentration dependence on photocatalytic activity of TiO2-x N x powders. *The Journal of Physical Chemistry B* **2003,** 107, (23), 5483-5486.
(99) Park, B.-I.; Jie, H.; Song, B.-G.; Kang, K.-M.; Park, J.-K.; Cho, S.-H., The structural, morphological, and surface properties of tungsten-doped TiO2 nanopowders and their contribution to the photocatalytic activity. *Research on Chemical Intermediates* **2014,** 40, (1), 115-126.
(100) Zhao, Z.; Liu, Q., Mechanism of higher photocatalytic activity of anatase TiO2 doped with nitrogen under visible-light irradiation from density functional theory calculation. *Journal of Physics D: Applied Physics* **2007,** 41, (2), 025105.
(101) Castro, Y.; Arconada, N.; Durán, A., Synthesis and photocatalytic characterisation of mesoporous TiO 2 films doped with Ca, W and N. *Boletín de la Sociedad Española de Cerámica y Vidrio* **2015,** 54, (1), 11-20.
(102) Maeda, M.; Yamada, T. In *Photocatalytic activity of metal-doped titanium oxide films prepared by sol-gel process*, Journal of Physics: Conference Series, 2007; IOP Publishing: 2007; p 755.
(103) Lettmann, C.; Hildenbrand, K.; Kisch, H.; Macyk, W.; Maier, W. F., Visible light photodegradation of 4-chlorophenol with a coke-containing titanium dioxide photocatalyst. *Applied Catalysis B: Environmental* **2001,** 32, (4), 215-227.
(104) Chong, M. N.; Jin, B.; Chow, C. W.; Saint, C., Recent developments in photocatalytic water treatment technology: a review. *Water research* **2010,** 44, (10), 2997-3027.
(105) Prairie, M. R.; Evans, L. R.; Martinez, S. L. In *Destruction of organics and removal of heavy metals in water via TiO 2 photocatalysis*, Chemical oxidation: Technology for the nineties. Second international symposium, 1992; 1992; pp 428-441.
(106) Grandcolas, M.; Sinault, L.; Mosset, F.; Louvet, A.; Keller, N.; Keller, V., Self-decontaminating layer-by-layer functionalized textiles based on WO 3-modified titanate nanotubes. Application to the solar photocatalytic removal of chemical warfare agents. *Applied Catalysis A: General* **2011,** 391, (1), 455-467.

(107) Mahmoodi, N. M.; Arami, M., Degradation and toxicity reduction of textile wastewater using immobilized titania nanophotocatalysis. *Journal of Photochemistry and Photobiology B: Biology* **2009,** 94, (1), 20-24.
(108) Tang, Z.-R.; Li, F.; Zhang, Y.; Fu, X.; Xu, Y.-J., Composites of titanate nanotube and carbon nanotube as photocatalyst with high mineralization ratio for gas-phase degradation of volatile aromatic pollutant. *The Journal of Physical Chemistry C* **2011,** 115, (16), 7880-7886.
(109) Tang, Z.-R.; Zhang, Y.; Xu, Y.-J., A facile and high-yield approach to synthesize one-dimensional CeO 2 nanotubes with well-shaped hollow interior as a photocatalyst for degradation of toxic pollutants. *RSC Advances* **2011,** 1, (9), 1772-1777.
(110) Fujishima, A.; Rao, T. N.; Tryk, D. A., Titanium dioxide photocatalysis. *Journal of Photochemistry and Photobiology C: Photochemistry Reviews* **2000,** 1, (1), 1-21.
(111) Fujishima, A.; Kohayakawa, K.; Honda, K., Hydrogen production under sunlight with an electrochemical photocell. *Journal of the Electrochemical Society* **1975,** 122, 1487-1489.
(112) Zhang, Y. J.; Wang, Y. C.; Yan, W.; Li, T.; Li, S.; Hu, Y. R., Synthesis of Cr 2 O 3/TNTs nanocomposite and its photocatalytic hydrogen generation under visible light irradiation. *Applied Surface Science* **2009,** 255, (23), 9508-9511.
(113) Sekiguchi, Y.; Yao, Y.; Ohko, Y.; Tanaka, K.; Ishido, T.; Fujishima, A.; Kubota, Y., Self-sterilizing catheters with titanium dioxide photocatalyst thin films for clean intermittent catheterization: Basis and study of clinical use. *International journal of urology* **2007,** 14, (5), 426-430.
(114) Toma, F.-L.; Bertrand, G.; Klein, D.; Meunier, C.; Begin, S., Development of photocatalytic active TiO 2 surfaces by thermal spraying of nanopowders. *Journal of Nanomaterials* **2008,** 2008, 58.
(115) Morris, D.; Egdell, R., Application of V-doped TiO2 as a sensor for detection of SO2. *Journal of Materials Chemistry* **2001,** 11, (12), 3207-3210.
(116) Mor, G. K.; Carvalho, M. A.; Varghese, O. K.; Pishko, M. V.; Grimes, C. A., A room-temperature TiO 2-nanotube hydrogen sensor able to self-clean photoactively from environmental contamination. *Journal of Materials Research* **2004,** 19, (2), 628-634.
(117) Ruiz, A. M.; Cornet, A.; Morante, J. R., Performances of La–TiO 2 nanoparticles as gas sensing material. *Sensors and Actuators B: Chemical* **2005,** 111, 7-12.
(118) Garzella, C.; Bontempi, E.; Depero, L.; Vomiero, A.; Della Mea, G.; Sberveglieri, G., Novel selective ethanol sensors: W/TiO 2 thin films by sol–gel spin-coating. *Sensors and Actuators B: Chemical* **2003,** 93, (1), 495-502.

Chapter Two

Experimental Methods

2.1 Experimental Setup

A schematic of the experimental setup used to synthesize titania nanoparticles is shown in Figure 0.1**.** Liquid TTIP precursor partially fills an inner-glass container that is supported on a rotating platform and water cooled. An outer-glass container allows circulation of N_2 gas through the hermetically-sealed system. Liquid TTIP precursor in the inner container is shrouded with flowing N_2, which serves to prevent its reaction with ambient air. A frequency-doubled Nd:YAG pulsed laser (wavelength 532 nm, maximum pulse energy 500 mJ/pulse) is focused into the container to decompose the liquid precursor, thereby forming a high concentration of vaporized species within a submerged plasma, which then experiences rapid condensation/quenching by the surrounding un-reacted and chilled liquid-TTIP precursor solution.

To maximize the decomposition rate, while ensuring the high quenching rate needed to produce amorphous nanoparticles, the laser beam is focused just below the surface of the liquid precursor solution. To keep the temperature of the TTIP constant during processing, the container is water cooled. After operation, a suspension of nanoparticles is formed in the liquid precursor, which is extracted by centrifuging.

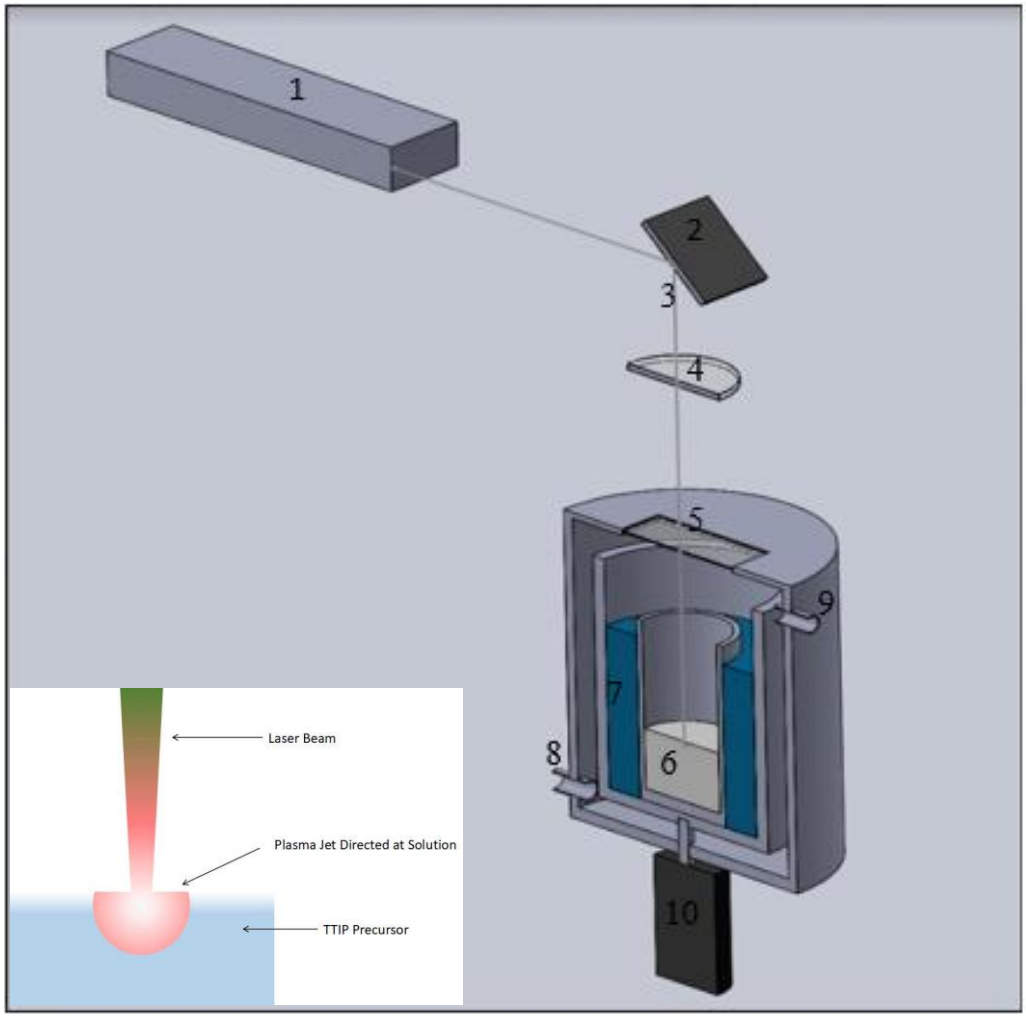

Figure 0.1. Schematic diagram of the experimental setup: (1) Nd-YAG laser; (2) reflecting mirror; (3) laser beam; (4) focusing lens; (5) cover plate (glass slide); (6) liquid TTIP precursor; (7) chilled water bath; (8) N2 gas inlet; (9) N_2 gas outlet; and (10) motor-driven support.

Small samples of as-synthesized TiO_2 nanoparticles, before and after heat treatment, are characterized for composition, structure, and morphology using conventional analytical techniques, such as X-ray diffraction (XRD), X-ray photoelectron spectroscopy (XPS), scanning electron microscopy (SEM), UV-Visible spectroscopy, and transmission electron

microscopy (TEM). Post heat treatments are performed in both air and nitrogen. Photocatalytic activity is measured by gas-phase methanol oxidation, under both ultraviolet illumination and no illumination (dark) conditions.

Quantitative details of the experiment can be found in the Appendix.

2.2 Analytical Instrument

To gain a better understanding of composition, structure, and the morphology of the as-synthesized and the heat-treated TiO_2 nanopowders, conventional analytical techniques are employed and described briefly below.

2.2.1 Scanning Electron Microscope

A Zeiss-Sigma Scanning Electron Microscope (SEM) with a Schottky Field Emission (FE) source and a GEMINI electron optical column are shown in Figure 0.2 and Figure 0.3. The equipment features detectors that allow imaging of particles and surfaces, as well as measurements of their compositions. There are three detectors and one image analyzer, i.e.:

(i) In-lens secondary electron detector

(ii) Lateral secondary electron detector

(iii) 4-quadrant backscatter electron detector

(iv) EDS system with fully digital image collection, transfer and analysis

Figure 0.2. Zeiss-Sigma scanning electron microscope [1].

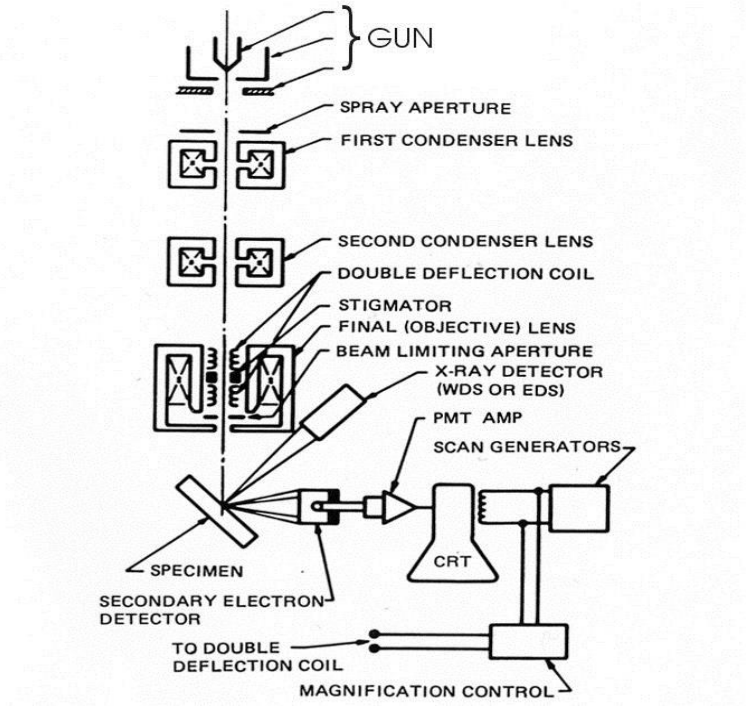

Figure 0.3. Schematic of a scanning electron microscope [2].

Apertures are 20-120 micron in size, and maximum accelerating voltage is 30kV. The instrument includes a 5-axis rotary stage. Sample sizes up to 20 cm can be accommodated [1]. A focused beam of high-energy electrons is used within the FESEM to collects signals generated when the beam is scattered by the surface of a solid specimens. The signals resulting from electron-sample interactions reveal information about morphology, crystalline structure, orientation, and chemical composition. In most cases, data are collected over a selected area of the surface of the specimen, and a 2-dimensional image is generated that displays spatial variations in these properties, while also providing qualitative or semi-quantitative analysis of chemical composition (using EDS), crystal orientations (using EBSD), and crystalline structure. According to the method and function adopted, the FESEM is considered to be similar to an Electron Probe Micro-Analyzer (EPMA), since there are common capabilities between the two instruments [3].

2.2.2 X-Ray Diffraction Unit

X-ray diffraction (XRD) is one of the primary methods available to determine atomic structure, including crystallite size, phase, and composition. It is a nondestructive technique that is relatively fast and easy compared with techniques that give similar information such as transmission electron microscopy (TEM). A PANalytical X-ray diffraction (XRD) unit equipped with on-board control electronics, offers high throughput, high-quality phase identification and quantification, residual stress analysis, grazing incidence diffraction, X-ray reflectometry, small-angle X-ray scattering, pair distribution function analysis, and non-ambient diffraction [3].

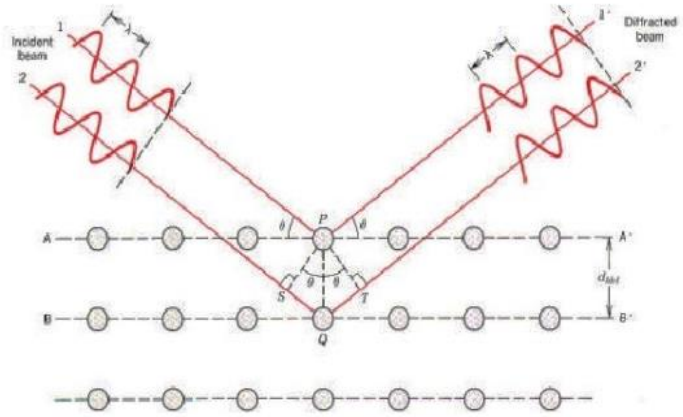

Figure 0.4. Incident and diffracted beams on a crystal plane [4].

When the wavelength of the incident radiation is comparable with or smaller than the lattice constant of a crystal, the diffracted beams are obtained in directions different from the incident direction. W.L. Bragg put forward a simple explanation. If the incident waves are reflected specularly from parallel planes of atoms in the crystal, with each plane reflecting only a very small fraction of the radiation, the angle of incidence is equal to the angle of reflection. The diffracted beams, Figure 0.4, are formed when reflections from parallel planes of atoms experience constructive interference [4]. According to Bragg's analysis:

$$2d \sin\theta = 2\pi n\lambda \qquad 0\text{-}1$$

Where (d) is the spacing of parallel atomic planes and ($2\pi n$) is the difference in phase between reflections from successive planes. The reflection planes have nothing to do with the surface planes bounding the particular specimen [4].

2.2.3 X-ray Photoelectron Spectrometer

Thermo Scientific's K-Alpha creates chemical state images of the surface. K-Alpha X-ray photoelectron spectrometer (XPS), Figure 0.5, is designed for a multi-user environment. The analytical options include tilt module for data collection and recirculating inert-gas glove box for transfer of air-sensitive samples [5]. K-Alpha XPS has the following specifications as shown in Table 0-1 [5]

Table 0-1. K-Alpha XPS features and specifications	
Feature	Specifications
Analyzer	180° double focusing hemispherical analyzer, 128-channel detector
X-ray source	Al Kα micro-focused monochromator, with variable spot size 30-400 μm
Charge compensation	Dual beam source, ultra-low energy electron beam Ion Gun
Energy range	100 eV to 4 keV
Sample handling	60 × 60 mm sample area, 20 mm maximum sample thickness
Vacuum system	2 x 260 l/s turbo-molecular pumps for entry and analysis chambers

When an X-ray beam is directed onto the surface of a material, its energy causes excitation of the bonding electrons, giving them enough kinetic energy to leave that surface and into the surrounding, Figure 0.6. Since every bond in the material surface has different amounts of electrons with different kinetic energies, this effect is adopted as a means to determine the nature of the bonding on any surface [6].

Figure 0.5. Thermo Scientific's K-Alpha X-ray photoelectron spectrometer [5].

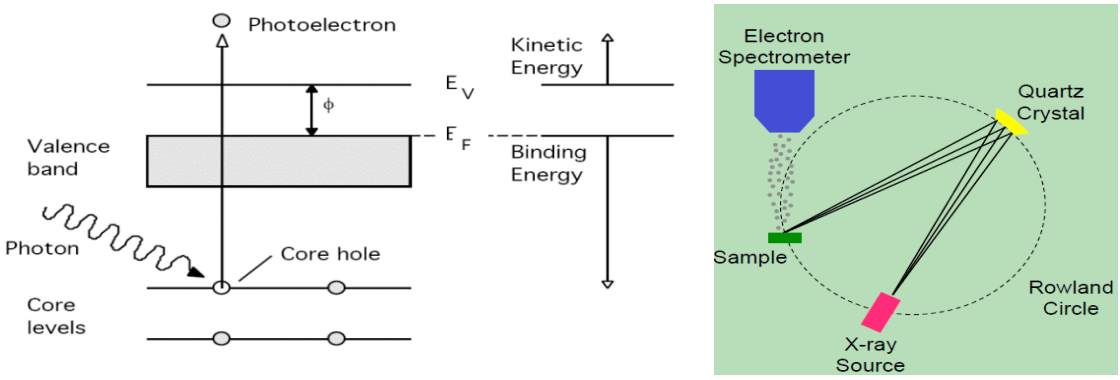

Figure 0.6. Photoelectric effect (left) and XPS work principle (right) [6].

2.2.4 Transmission Electron Microscope

JEOL's 2010F Field-Emission Scanning Transmission Electron Microscope (FE-STEM) employs a technique whereby a beam of electrons is transmitted through an ultra-thin specimen, interacting with the specimen as it passes through. An image is formed from the interaction of the electrons transmitted through the specimen. STEM is capable of direct lattice imaging and composition analysis via EDS and EELS/GIF.

JEOL's FE-STEM has the following specifications [7]:

- Acceleration voltage 20-200kV with ZrO-W field emission source
- Scanning Transmission Electron Microscopy (STEM) interface
- Digital imaging with 1Kx1K CCD camera
- BF/DF STEM detectors
- HADF STEM detector
- Electron Energy Loss (EELS) spectrometer
- Kx2K GATAN imaging EELS filter (GIF)
- Heating (1400K) and cooling (90K) holders

Figure 0.7. JEOL 2010F scanning transmission electron microscope [8]**.**

A schematic ray diagram, Figure 2.8, shows:

- Illumination system, which takes the electrons from the gun and transfers them to the specimen, giving either a broad beam or a focused beam.
- Objective lens and stage, which is the heart of the TEM.
- TEM imaging system, which includes intermediate lens and projector lens.

At the back focal and image planes of the objective lens, the diffraction pattern and image are formed. To obtain the diffraction pattern on the screen, the back focal plane is selected as the objective plane of the intermediate lens and projector lens. In this case, the TEM works in a diffraction mode. To form an image on the screen, the image plane of the objective lens is selected as the objective plane of the intermediate lens and projector lens, which is called the imaging mode [9].

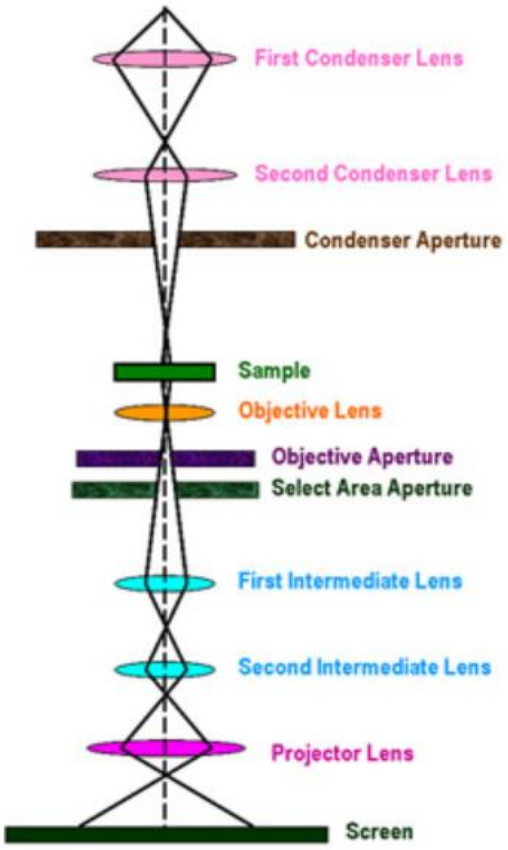

Figure 0.8. Ray diagram for a transmission electron microscope [9].

References

[1] https://microscopy.stanford.edu/sem-zeiss-sigma-fesem-

[2] https://serc.carleton.edu/research_education/geochemsheets/techniques/SEM.html

[3] http://www.iitk.ac.in/meesa/SEM/SEM_manual.pdf

[4] Kacher, J., Landon, C., Adams, B. L., & Fullwood, D. (2009). Bragg's law diffraction simulations for electron backscatter diffraction analysis. *Ultramicroscopy*, *109*(9), 1148-1156.

[5] Moore, D. M., & Reynolds, R. C. (1989). *X-ray Diffraction and the Identification and Analysis of Clay Minerals* (Vol. 332). New York: Oxford university press.

[6] https://xpssimplified.com/kalpha_surface_analysis.php

[7] https://xpssimplified.com/xray_generation.php

[8] http://iamdn.rutgers.edu/facilities-main/16-home/48-electron-microscopy

[9] http://www.nanoscience.gatech.edu/zlwang/research/tem.html

Chapter Three

Crystalline-layered fabrication of TiO_2 nanorods and nanospheres

3.1 Introduction

With issues related to the use of non-renewable fossil fuels to satisfy increasing energy demand, photocatalysis has received attention because of its potential applications in environmental remediation and clean-energy production. TiO_2-based photocatalysts are strong candidates for industrial-scale applications given their photoactive efficiency, stability, low cost, nonhazardous nature, and ability to be activated by solar light [1-4].

TiO_2 belongs to the transition-metal oxide family and forms several polymorphs, e.g., anatase (tetragonal), brookite (orthorhombic), rutile (tetragonal), and others [5-8]. In comparison with other polymorphs, anatase-TiO_2 is preferable for solar-cell applications because of its high electron mobility, low dielectric constant, and lower density [5]. Anatase-TiO_2 also has a slightly higher Fermi level, a lower capacity to adsorb oxygen, and a higher degree of hydroxylation compared with other phases. These properties increase the photoactivity of TiO_2 [9, 10]. Based on charge-carrier dynamics, chemical properties, and activity of photocatalytic degradation of organic compounds, anatase-TiO_2 appears to be the most active photocatalytic polymorph [11].

TiO_2 has been synthesized in the form of nanoparticles [12], nanotubes [13], thin films [14, 15], and nanorods [16]. Methods employed include hydrolysis precipitation [17], sol-gel,

hydrothermal [18, 19], flame synthesis [20-23], inert gas condensation [24], and oxidation-hydrothermal synthesis of metallic Ti [25]. In all these methods, several variables must be considered, with one of the most important being particle size. Wegner and Pratsinis [26] rapidly quenched a flame aerosol using a critical-flow nozzle to control precisely the synthesis of nanoparticles with a broad range of sizes, morphologies, and phase compositions. When particle size is several nanometers, because of the very high surface-to-volume ratio, novel optical properties are expected [27]. Ultrafine anatase-TiO_2 nanoparticles (5-100 nm) have been synthesized via sol-gel precipitation of alkoxides, followed by hydrothermal treatment [18]. TiO_2 and titanate nanotubes, synthesized by hydrothermal and electrochemical-anodic oxidation methods, have been reported [28, 29].

TiO_2 nanotubes exhibit unique features that are beneficial in photocatalysis, in comparison with commonly used TiO_2 nanopowders. The higher surface area (478 m^2/g) gives larger adsorption capacity, with pore volume up to 1.25 cm^3/g [30-32]. Nanotubes also exhibit ion-exchange ability [33], rapid and long distance electron transport capability [34], and enhanced light absorption because of the high ratio of length-to-tube diameter [35]. Three main routes have been developed to synthesize TiO_2 nanotubes: (*i*) template method that helps to construct materials through adjustments in template morphology [36-39], (*ii*) anodic oxidation that builds crystallized films of TiO_2 immobilized on a titanium foil surface [40-42], and (*iii*) hydrothermal synthesis that allows high nanotube yields by dissolving TiO_2 or its precursor in a concentrated aqueous solution of NaOH [42, 43]. Using the hydrothermal synthesis method in NaOH-water-ethanol solution, Yan et al. [44] prepared a rutile nanotube from rutile-anatase particles. The rutile nanotubes show optoelectronic properties different

from those of the raw TiO_2. In addition, titanate nanotubes have been synthesized using a hydrothermal method [28, 45]. Nanotubes calcined at 600ºC show excellent properties in the decomposition of Acid Red 18 in water, but with lower photocatalytic activity than that of P25 [45]. Nanorod TiO_2 is an important morphology and has been synthesized by different methods. Vertically-aligned nanorods have increased electron transport and reduced charge carrier recombination, giving excellent electron transport property in comparison to that for nanoparticles [46]. TiO_2 nanorods have also been grown on tungsten carbide substrates through metalorganic chemical vapor deposition [47]. Limmer [48] prepared TiO_2 nanorods via electrophoretic deposition. Aligned anatase and rutile TiO_2 nanorods have also been prepared by sol-gel template method [49].

In this work, pulsed-laser decomposition of titanium tetra-isopropoxide (TTIP) is used to synthesize amorphous-titania nanoparticles in both discrete and agglomerated forms. Post-annealing transforms as-synthesized amorphous nanoparticles into nanocrystalline counterparts, but with layered crystalline structure resembling nanotubes and nano-onions in morphology. After annealing at intermediate temperatures, the resulting nanostructures have anatase-TiO_2 crystallinity, whereas at high temperatures the resulting nanostructures convert to rutile-TiO_2 crystallinity. Details of these nanopowder products and their phase transitions are presented below. In addition, the effects of such phase transitions on photocatalytic behavior are investigated preliminarily.

3.2 Results and Discussion

3.2.1 As-synthesized nanostructures

The titania materials synthesized directly in this work by pulsed-laser decomposition of TTIP assume various morphologies, but invariably have non-crystalline or amorphous structures. Samples for SEM observations are taken from three locations of the glass-reactor vessel, as shown in Figure 0.1. Under the cover plate of the vessel, relatively dense films are observed, Figure 0.2, which are the products of vapor transport and condensation of precursor species from the plasma-reactor zone. As indicated, with increasing exposure time to ambient air, *craze-cracking* of the deposited film occurs, apparently because of release of volatile species, accompanied by film shrinkage. In striking contrast, agglomerated nanoparticles are observed on the cold wall and at the bottom of the vessel, Figure 0.3**.** Within the *liquid precursor* itself, discrete nanoparticles are found, as well as fragments of thin films that have broken off from the cover plate; see Figure 9 for TEM images.

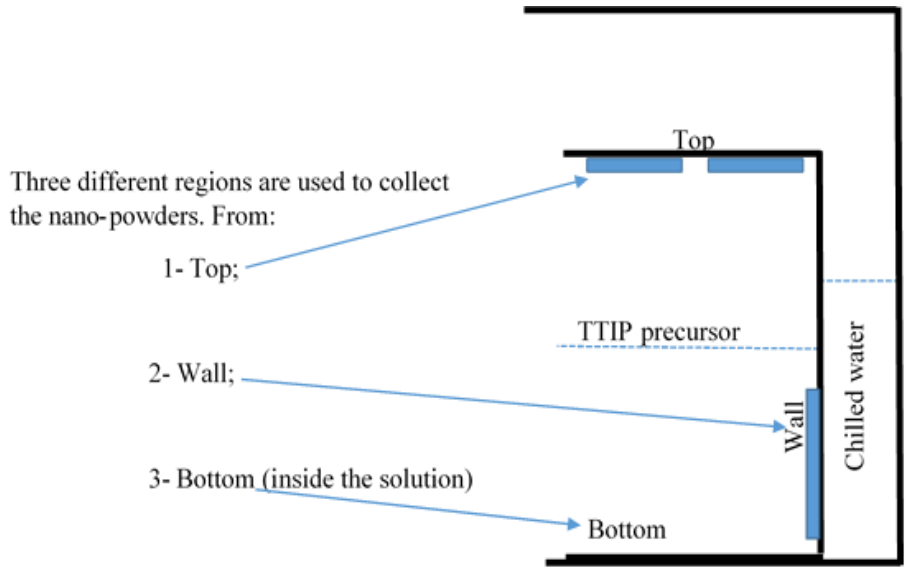

Figure 0.1. Schematic diagram of locations where as-synthesized TiO_2 samples are taken for characterization purposes.

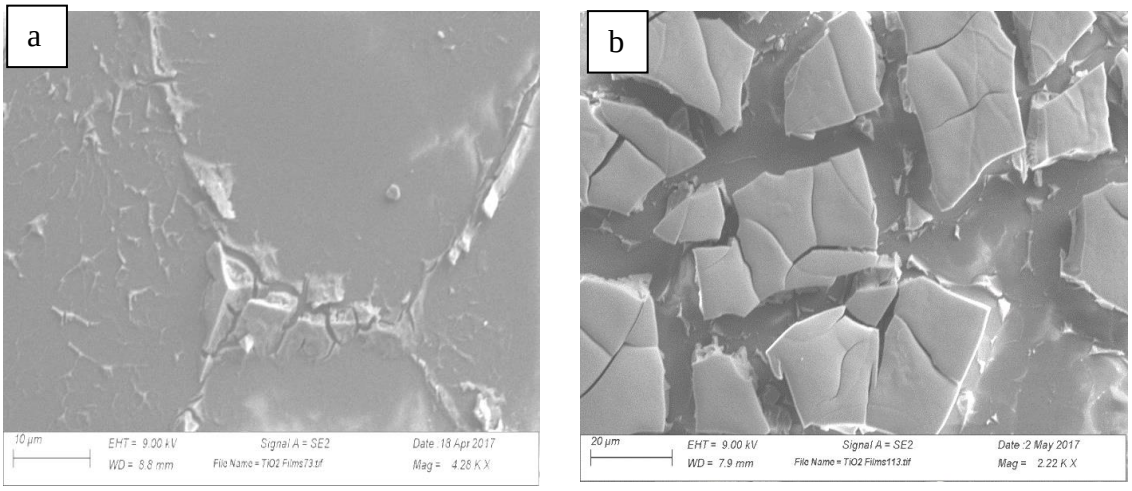

Figure 0.2. Craze-cracking of thin/thick film formed on the inside surface of the cover plate: (a) as deposited, and (b) after exposure to ambient air for several hours.

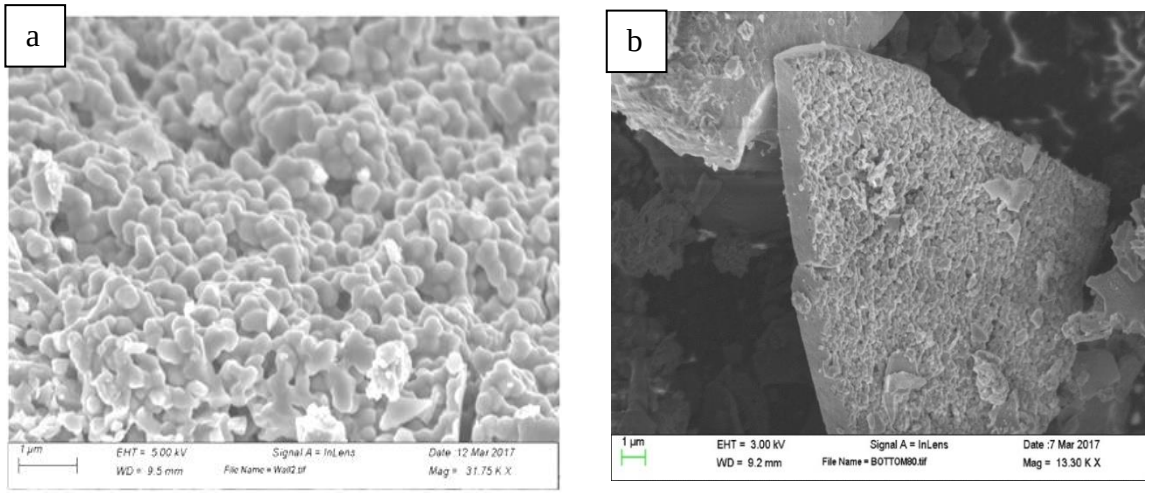

Figure 0.3. Agglomerated nanoparticles deposited: (a) on the cold wall of the vessel; and (b) at the bottom of the vessel.

XRD scans of nanostructured particles and films, taken from all three locations of the reactor vessel, show that they are non-crystalline or amorphous-like in nature. This aspect also applies to weakly-agglomerated and strongly-aggregated nanoparticles. Of particular interest are the well-aligned nanoparticles deposited on the cold wall of the vessel, which appear to be in various stages of densification while retaining an amorphous-like structure. Such behavior suggests the possibility of controlled thin/thick film deposition of fully-dense amorphous-like titania. Experiments are underway to check this concept, including the effects of quenching rate, radiant heating, and stand-off distance.

In Figure 0.2, the as-deposited film has the appearance of a dense CVD-derived film. This result opens opportunities for post-annealing to generate *new phases with nanocrystalline structures* that are not accessible to CVD, which is a near-equilibrium deposition process. Here, deposition rates should also be higher, since the laser-processed

films are derived from decomposed precursor species that arrive on the substrate surface. This manner is in contrast to CVD where deposition occurs via thermal decomposition of precursor molecules at or near a heated substrate surface. Another variable of interest in laser processing, therefore, is the effect of moderate heating of the substrate.

3.2.2 Heat treatment of nanopowders

Upon subsequent heat treatment at intermediate temperatures, an amorphous-to-anatase TiO_2 phase transformation occurs; whereas at high temperatures, an anatase-to-rutile TiO_2 phase transformation occurs. A series of XRD spectra for as-synthesized amorphous-TiO_2 nanopowder, after post-annealing at 300-950ºC for 2 hours in ambient air, is shown in.Figure 0.4. Diffraction angles at 25.3° and 27.4° represent anatase-TiO_2 (A) and rutile-TiO_2 (R) phases, respectively [50]. As indicated, at about 400ºC, an amorphous-to-anatase TiO_2 phase transformation occurs. At this temperature, there exists sufficient atomic mobility to allow rearrangement of quenched-in Ti, O, and C species to form the more stable anatase TiO_2 phase, while at the same time eliminating excess oxygen and impurity carbon by a diffusion-controlled process. When the annealing temperature is increased to ~800ºC, the rutile phase makes an appearance, accompanied by some nanoparticle growth (Table 0-1).

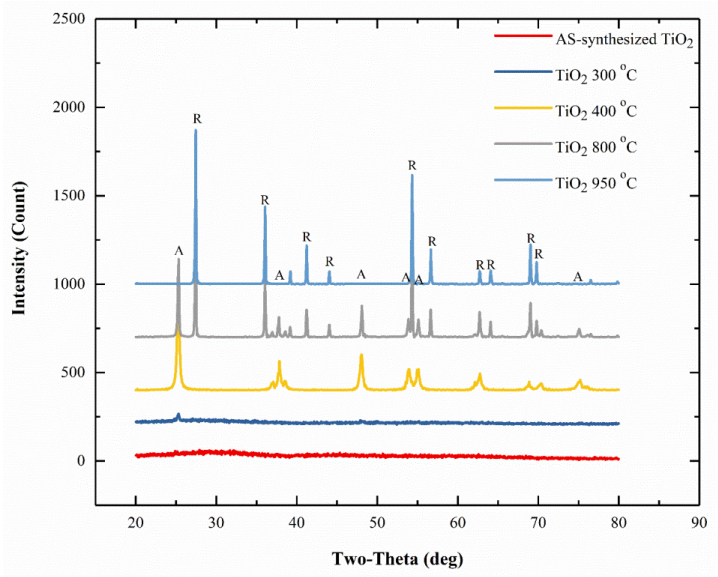

Figure 0.4. A series of XRD spectra for as-synthesized amorphous-TiO_2 nanoparticles, after post annealing at 300-950 ºC for 2 hr in air, showing transformation to anatase-TiO_2 at ~ 400ºC, and then to rutile-TiO_2 at ~800ºC. (A-anatase, R-rutile).

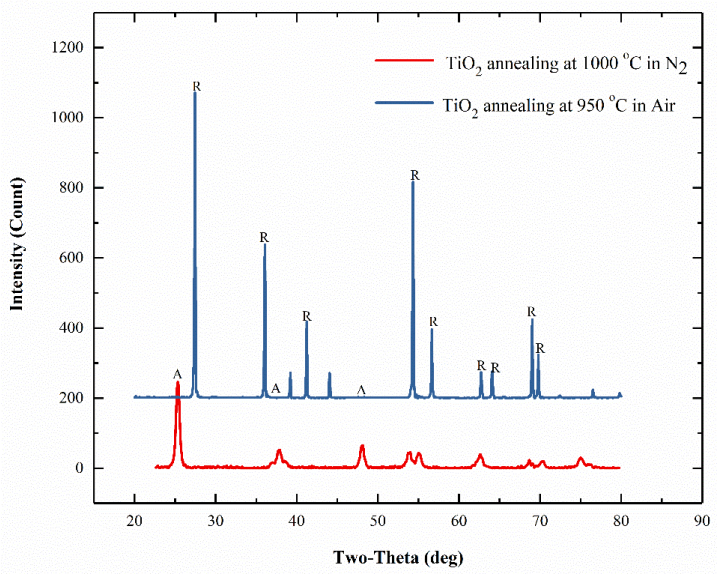

Figure 0.5. Comparison of XRD patterns of as-synthesized anatase-TiO_2 after post-annealing in air and nitrogen at high temperatures, showing greater thermal stability of anatase phase when heated in nitrogen.

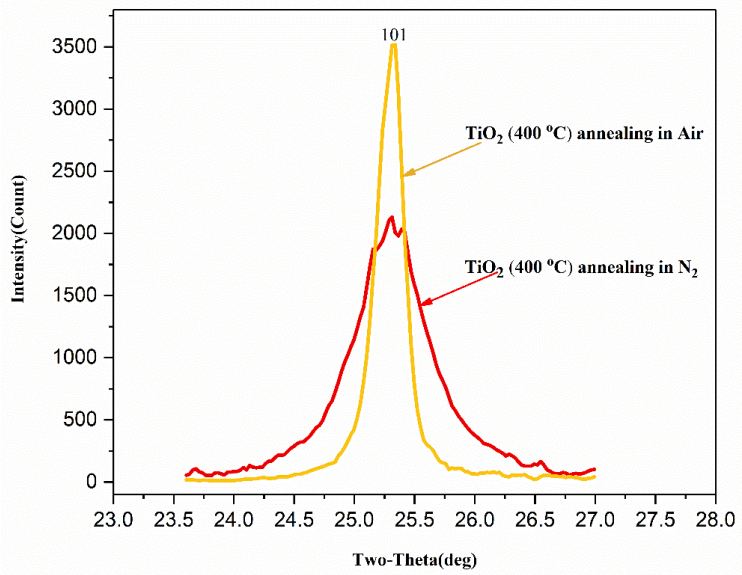

Figure 0.6. Comparison of XRD peak broadening of anatase-TiO_2 nanopowder after annealing at 400ºC for 2 hrs, showing much broader 101 peak after annealing in N_2.

.

Table 0-1. Nanoparticles growth					
TiO_2	300 °C	400 °C	700 °C	800 °C	950 °C
Anatase (nm)	19.9	23	54.7	56	..
Rutile (nm)	--	--	--	13	17

Because the diffusion distance is small for nanostructured materials, whatever their morphologies, it is not surprising that a metastable-to-stable transformation occurs at this low temperature of 400ºC. Heat treating the same TiO_2 nanopowder in N_2 to about 1000°C produces an anatase phase (Figure 0.5), indicating again that the far-from-stoichiometric composition of the original nanopowder inhibits the anatase-to-rutile TiO_2 phase transformation. After post-annealing as-synthesized amorphous-TiO_2 at 400ºC for 2 hr, the resulting anatase-TiO_2 diffraction peak at 25.3° is stronger and narrower after annealing

in air than in N_2, as seen in Figure 0.6. The corresponding grain sizes, as determined using Scherrer's method, are 23 nm and 10 nm, respectively. Additional investigation is needed to understand this interaction with ambient air in the amorphous-to-anatase TiO_2 transformation.

Figure 0.7 shows XPS scans of C 1*s*, Ti 2*p* and O 1*s* binding energies for anatase-TiO_2 nanopowder, after annealing at 400ºC for two hours in air. The binding energy of 284.72 eV corresponds to elemental carbon, likely coming from plasma-decomposition of the metalorganic TTIP precursor. The binding energies of 286.32 eV and 288.68 eV are indicative of Ti-C-O bonds in carbonate species [51-53]. Two types of carbonate species with binding energies of 287.5 eV and 288.5 eV are reported by Sakthivel and Kwasch[52]. On the other hand, Ren et al [51] observed only one type with binding energy of 288.6 eV. The presence of carbonate species indicates that the C atoms occupy interstitial sites in the TiO_2 lattice.

XPS signals of Ti 2*p* are observed at binding energies of 458.3 eV and 464.02 eV. The binding energy of Ti $2p_{3/2}$ peak in pure TiO_2 occurs at 458.5-459.7 eV[54]. In the Ti *2p* region, there is a binding energy of 458.3 eV, which is slightly lower than that of pure TiO_2. It has been suggested that the binding energy of the Ti *2p* peak shifts to lower energy when Ti^{4+} species are transformed to Ti^{3+}[55, 56].

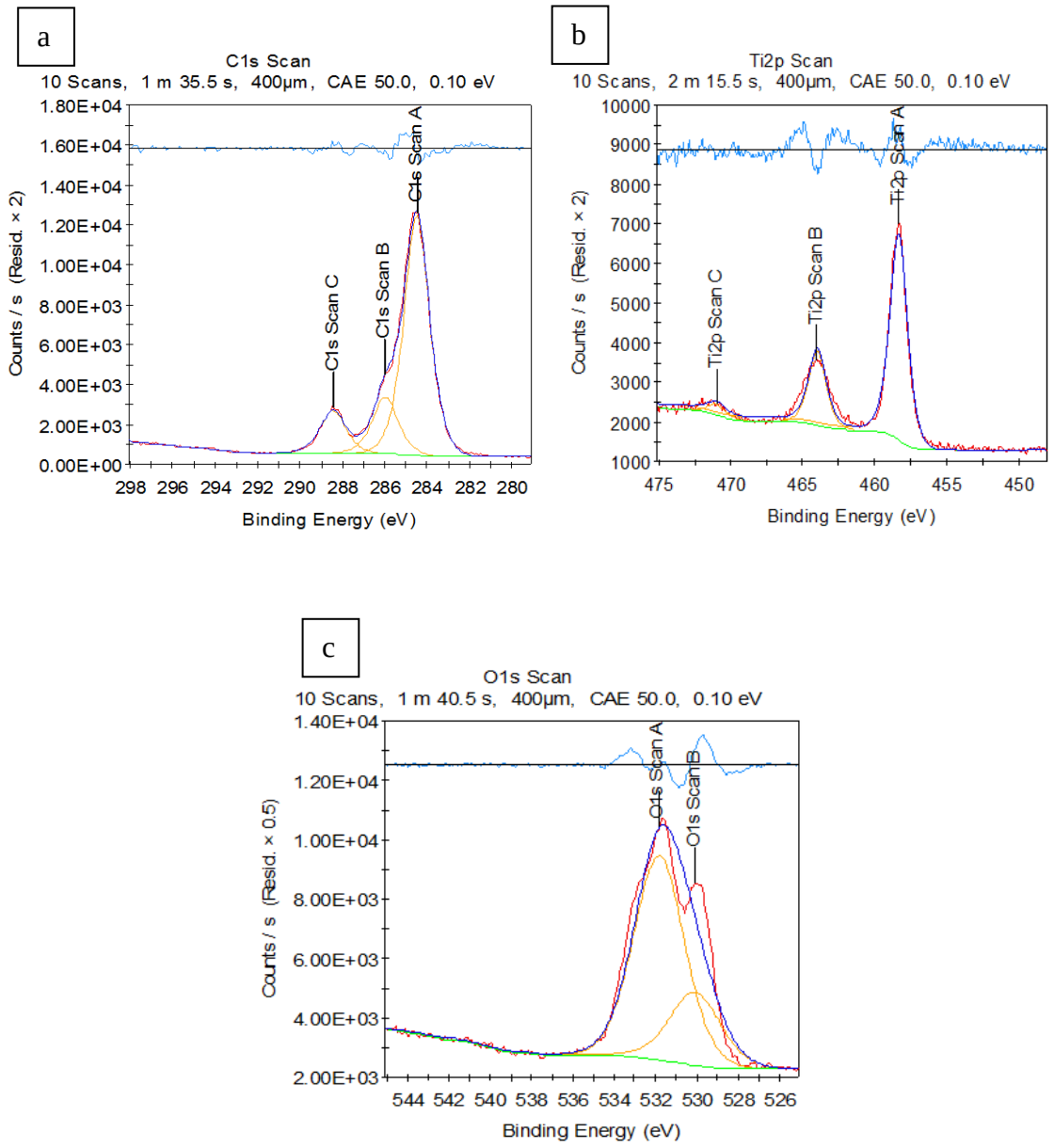

Figure 0.7. XPS scans for anatase-TiO_2 nanopowder after annealing at 400ºC for two hours: (a) C 1s species; (b) Ti 2p species; and (c) O 1s species

The shifting to lower binding energy is also observed by other researchers[52, 54]. The formation of an oxygen-vacancy state between valence and conduction bands in the C-doped TiO_2 is attributed to the presence of Ti^{3+} species[54].

Binding energies of O *1s* are observed at 530.09 eV and 531.82 eV. The binding energy of 530.09 eV is assigned to the Ti-O bond, whereas the binding energy of 531.82 eV is assigned to O bonded to Ti^{3+}. Xiao et al [54] also observed this binding energy at 531.5 eV. In this work, after annealing the nanopowder at 600ºC, a weak peak with binding energy of 282.55 eV, is observed (Figure 0.8), which can be attributed to C substituting for oxygen in the TiO_2 lattice, resulting in O-Ti-C bonds[52].

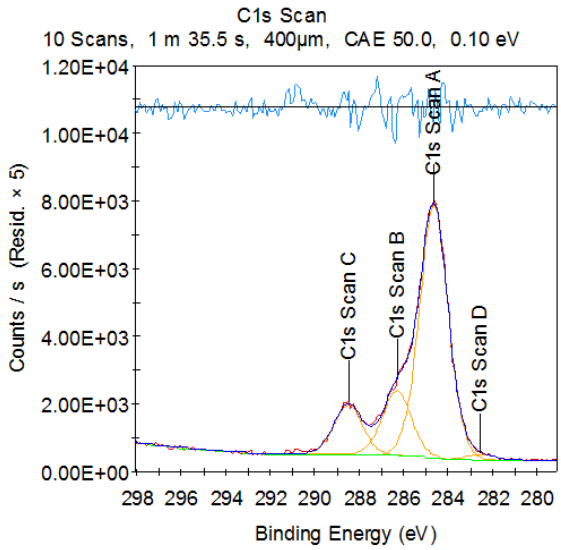

Figure 0.8. XPS scans for anatase-TiO_2 nanopowder after annealing at 400ºC for two hours, showing an additional weak peak with binding energy of 282.55 eV.

Examination of anatase-TiO_2 nanoparticles by high resolution STEM shows partially- or fully-transformed nanoparticles. Lattice imaging of a typical fully-transformed spherical-shaped TiO_2 nanoparticle reveals a radially-symmetric nanograin structure, in which each nanograin is separated from its neighbor by a disordered region that contains a high density of lattice defects. Furthermore, lattice imaging of a typical partially-

transformed spherical nanoparticle reveals a core-shell structure, in which the shell consists of fully-transformed (crystalline) anatase-TiO_2, and the core consists of un-transformed amorphous-TiO_2, as seen in Figure 0.9(a). A feature of the nanocrystalline core-shell structure is its radially-symmetric pie-shaped morphology. The presence of a high density of edge dislocations at each interface between adjacent nanograins would account for the observed tilt-angle between them. Figure 0.9(b) also shows a similar core-shell structure for a high-aspect ratio nano-fiber.

In all cases of partially-transformed nanoparticles, including nano-onions and nano-fibers, nano-crystallization induced by post-annealing is initiated at the surfaces of the nanoparticles and then propagates uniformly into their interiors, eventually yielding fully transformed nanocrystalline anatase-TiO_2. Previously-mentioned Figure 0.9(b) of a high-aspect ratio nanofiber shows evidence that the phase transformation from amorphous-to-nanocrystalline anatase TiO_2 occurs by a layer-by-layer growth mechanism. Moreover, it appears that layered growth starts at a favorable location on the outside and then propagates inward in a sleeve-like manner in opposite directions. Superposition of such sleeve-like layers gradually builds up a radially-symmetric layered nanostructure, reminiscent of a tree's ring-like structure, but from outside in.

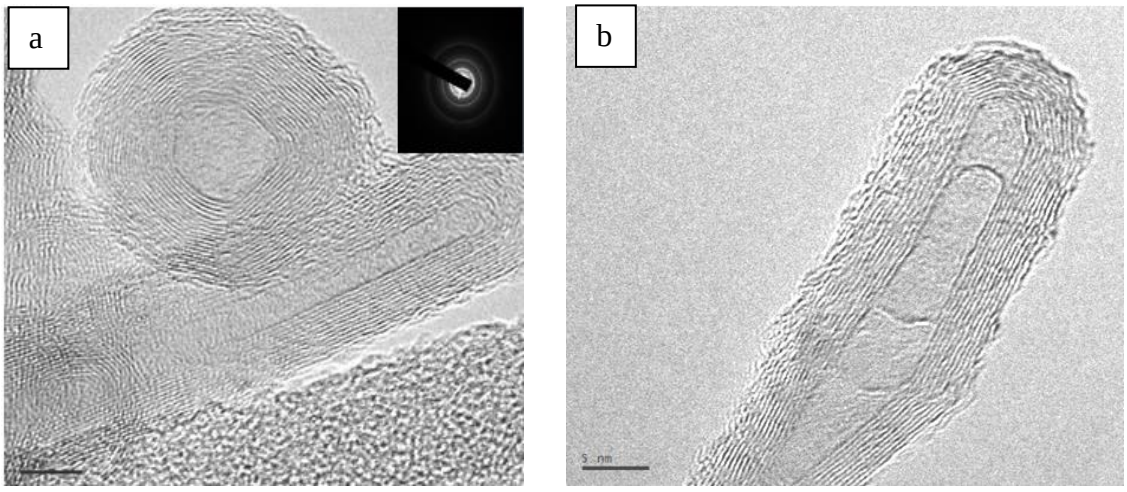

Figure 0.9 As-synthesized amorphous-TiO_2 nanoparticles after annealing at 400ºC for 2 hours showing: (a) core-shell structures of partially-transformed nanoparticles, in which the shell is transformed (crystalline) anatase-TiO_2 and the core is un-transformed amorphous-TiO_2; and (b) high resolution image of a nano-fiber indicating propagation of a phase-transformation interface via a layer-by-layer mechanism. TEM Images collected with the help of Zhizhong Dong.

3.2.3 Photocatalytic activity

To determine photocatalytic activity, samples (i.e., as-synthesized amorphous-TiO_2 nanopowders and post-annealed nanopowders in air at 400ºC) are tested for hydrogen evolution from water reduction with methanol as a sacrificial agent, similar to the procedure reported by Wu et al [57]. The reactions are conducted in a 25 ml glass reactor filled with 10 ml of 20% methanol (*Sigma Aldrich*) in DI water. Fresh catalyst (2 mg) is dispersed in 10 ml of reaction solution via sonication for 1 minute. The reactor is illuminated by a 150W Xenon Ozone-free Arc Lamp (Newport), where a beam turning reflector with a cut-off of 280 nm – 400 nm (*Newport*) and FSQ-UG5 colored glass filter (*Newport*) ensure that the catalyst bed is irradiated with only UV light. After 20 minutes,

hydrogen production is measured by injecting 300 µL of the reactor headspace for each sample into an *Agilent 7890B* gas chromatograph with thermal conductivity detector. Both thermocatalytic (no illumination) and photocatalytic (UV-illumination) conditions are evaluated at room temperature. Commercial samples of anatase and rutile (*Acros Organics*) and P25 (an anatase-rutile mixture) (*Evonik*) are compared to our as-synthesized amorphous and annealed anatase samples, as well as to a control sample without any catalyst.

Nanocrystalline anatase-TiO_2 is active for hydrogen production at room temperature under UV illumination, Figure 0.10. After 20 minutes, hydrogen production over the as-synthesized (84.9 µmol g_{cat}^{-1}) and post-annealed nanocrystalline anatase (96.9 µmol g_{cat}^{-1}) is greater than those of commercial anatase (5.7 µmol g_{cat}^{-1}), rutile (13.2 µmol g_{cat}^{-1}), and P25 (21.5 µmol g_{cat}^{-1}). No hydrogen forms in the absence of a semiconductor catalyst. Without any illumination, the commercial samples of anatase, rutile, and P25 are completely inert. By contrast, the as-synthesized TiO_2 sample shows some hydrogen production (47.6 µmol g_{cat}^{-1}) under dark condition, most likely arising from decomposition of organic precursor trapped in the solid during synthesis. Therefore, probably only half of the hydrogen production under UV illumination can be attributed to photocatalytic water reduction. Annealing to 400 °C in air removes some of this trapped organic residue, reducing the amount of hydrogen seen in the dark condition to 32.6 µmol g_{cat}^{-1}. So while the hydrogen production of the as-prepared and post-annealed samples resemble one another under UV illumination, a larger fraction of the hydrogen formed over the post-annealed anatase material arises from photo-induced reaction. Additional investigation is

planned. At longer reaction times, the high-bulk-density powders settle out of suspension, making measurements difficult.

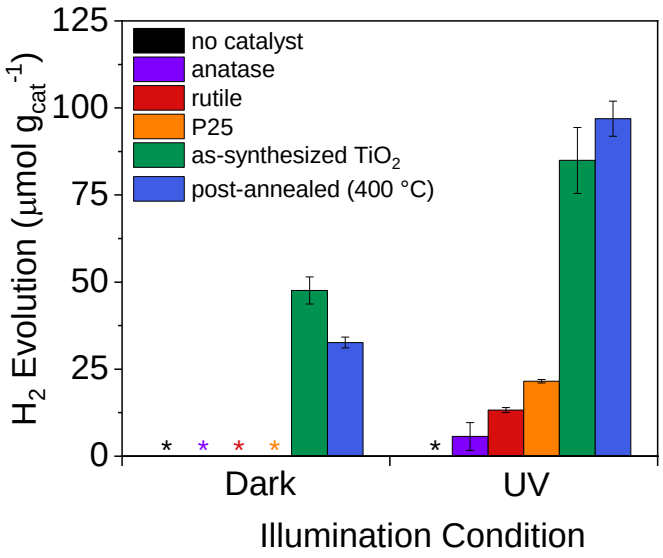

Figure 0.10. Hydrogen production per gram of catalyst from water reduction with 20% methanol as a sacrificial agent over anatase, rutile, P25, as-synthesized TiO_2 and post-annealed (400 °C) anatase TiO_2. Reaction duration of 20 minutes. ***** indicates no H_2 detected. Data collected with the help of Ashley Pennington.

Band gap energies are determined via diffuse-reflectance UV-Visible spectroscopy (*Thermo Scientific Evolution 3000*) equipped with a Praying Mantis diffuse reflectance accessory (*Harrick Scientific*). The spectra are collected between 200 nm and 1000 nm in intervals of 0.5 nm. The band-gap energy (BGE) of each sample is determined by the Tauc method Figure 0.11(a) and the diffuse reflectance derivative peak fitting (DPR) method [58] Figure 0.11(b). The BGE is calculated from the first and second derivatives to determine the slope and inflection point, respectively, to maximize accuracy. The indirect band-gap energy of the laser-produced/heat-treated anatase-TiO_2 nanopowder is determined to be

3.08 eV, which is reduced by >0.1 eV compared to that of commercial anatase; see **Table 0-2**. Enhanced near UV/high energy visible light absorption (340-450 nm) and a decrease in band-gap energy for the laser processed TiO_2 compared to that of commercial anatase Figure 13 indicates that the nanopowder should be more active under solar irradiation conditions. Carbon content, along with the new nanocrystalline layered morphology play the main roles of shifting the band gap. According to the literature, as mentiond before, TNT (Titanium nanotubes) have a lower band gap as compared to that of TiO_2 nanoparticles because of the increased surface area [30, 31]. In our work, we have found that anatase nanorods as well as nano-onions have decreased band gap in comparison with that for commercial anatase TiO_2, Figure 0.12.

Table 0-2. Band gap energies (BGEs) measured from Tauc½ and derivative peak fitting (DPR) methods indicate laser-processed anatase-TiO_2 has a lower direct (DPR) and indirect (Tauc1/2) BGE than commercial anatase-TiO_2

Sample	Tauc1/2 BGE [eV]	DPR BGE [eV]
Commercial anatase-TiO_2	3.23	3.31
Laser-processed anatase-TiO_2	3.08	3.18

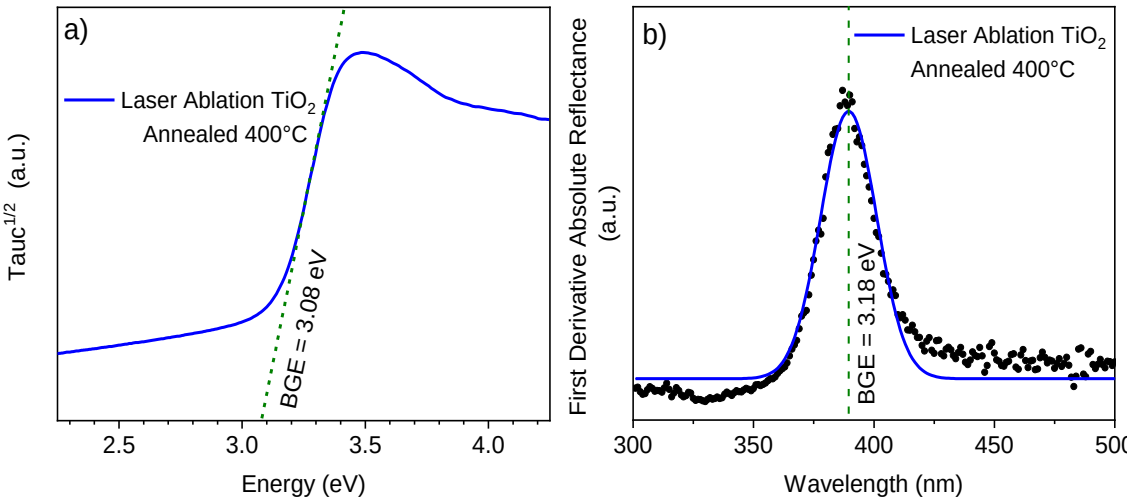

Figure 0.11. Methods for calculating BGE(a) Tauc1/2 of laser-processed anatase-TiO_2 nanopowder (b) DPR of laser-processed anatase-TiO_2 nanopowder. Data collected with the help of Ashley Pennington

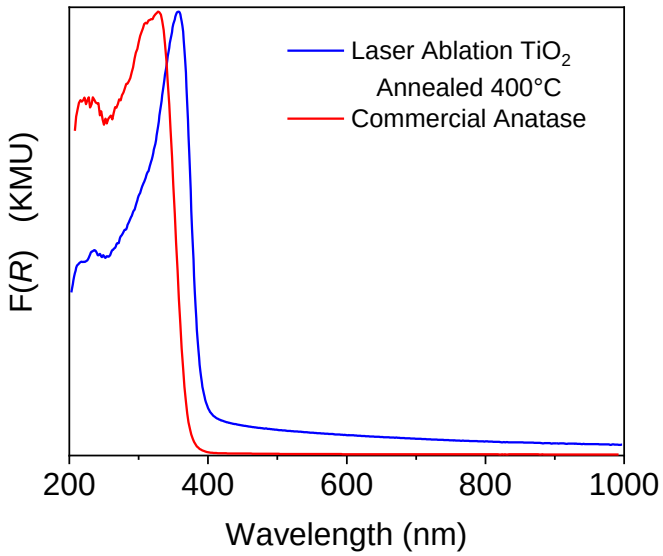

Figure 0.12. Kubelka-Munk Plot of laser-processed anatase-TiO_2 nanopowder and commercially processed anatase-TiO_2 powder, showing increase in absorbance in high energy UV region and a decrease in band-gap energy for the laser processed TiO_2. Data collected with the help of Ashley Pennington

3.3 Summary

Titanium dioxide (TiO_2) nanostructures are produced by pulsed-laser decomposition of titanium tetra-isopropoxide (TTIP). The laser is focused just below the surface of the liquid-metal-organic precursor, forming a high enthalpy *submerged-plasma* where precursor decomposition generates vaporized species, which upon subsequent rapid condensation/quenching by the surrounding liquid yields metal-oxide nanopowder. As-synthesized nanoparticles assume various morphologies, depending on the location within the glass-reactor vessel. On the inside of the cover plate, not in contact with the liquid precursor, relatively-dense amorphous titania films are formed. On the side-wall, in contact with the liquid precursor, relatively large-area flakes of aggregated nanoparticles are found. Within the liquid precursor, a suspension of discrete nanoparticles and loosely-agglomerated nanoparticles, are observed.

Whatever their size, shape or form, *as-synthesized nanoparticles have non-crystalline or amorphous-like structures.* Local compositional variations in the plasma-reaction zone, which are retained during rapid condensation/quenching of vaporized-precursor species, are believed to be responsible for amorphization of the nanoparticles because any significant deviation from the ideal stoichiometric composition of TiO_2 should inhibit its crystallization. Consistent with this model, chemical analysis of as-synthesized nanopowder shows that it is rich in oxygen and carbon relative to TiO_2. From chemical analysis, the composition of the as-synthesized nanopowder is $TiO_{2.7}C_{1.9}$. The chemical formula of the TTIP precursor is $TiO_4C_{12}H_{28}$. In other words, the presence of *excess*

oxygen and carbon (and possibly hydrogen) in the plasma inhibits nano-crystallization during rapid quenching. A similar effect should occur in other materials systems, where plasma-vaporized species derived from liquid precursors are far from stoichiometric values.

Upon post-annealing at 400ºC for 2 hours in ambient air, transformation of the amorphous-TiO_2 nanoparticles occurs, forming anatase-TiO_2 nanoparticles with little change in particle size. Apparently, at this temperature, there is sufficient atomic mobility to allow rearrangement of quenched-in Ti, O, and C species to form the more stable anatase-TiO_2 phase. Because diffusion distances are small in nanoparticles, whatever their morphologies, it is not surprising that the amorphous-to-anatase TiO_2 transformation occurs at the relatively low temperature of 400ºC (~ 0.3 T_M). Upon post-annealing at 800ºC for 2 hours in air, anatatase-TiO_2 transforms rapidly to rutile-TiO_2.

After annealing at 400ºC, examination of nanopowder by scanning transmission electron microscopy (STEM) shows partially- and fully-transformed anatase-TiO_2 nanoparticles. Lattice imaging of a *fully-transformed nanoparticle* reveals a radially-symmetric nanograin structure, in which each nanograin is separated from its neighbor by a disordered region, probably containing a high density of edge dislocations to account for the observed tilt-angle between neighboring nanograins. Lattice imaging of a *partially-transformed nanoparticle* reveals a core-shell structure, in which the shell is transformed anatase-TiO_2 and the core is un-transformed amorphous-TiO_2. The shell component is similar in appearance to that of fully-transformed anatase-TiO_2. The core component

appears amorphous-like, but upon closer examination at high resolution, there are regions where some degree of short-range ordering occurs.

It is concluded, therefore, that the amorphous-to-anatase phase transformation starts at the surfaces of the nanoparticles, irrespective of their morphologies, and propagates into the interior as in-situ reaction of trapped-in species likely yield gaseous products (e.g., CO, CH_4, H_2O) that diffuse out of the particles, leaving sufficient Ti and O to enable crystallization of anatase-TiO_2. In one remarkable case, such a diffusion-controlled transformation in a nanofiber appears to occur by propagation of anatase-TiO_2 layer-by-layer.

Reactions carried out at 200°C under both ultraviolet (UV) illumination and dark conditions, reveal photocatalytic production of methyl formate and acetalydehyde from methanol oxidation. Additionally, decreased band gap energy of the nanopowder, as well as increased light absorbance is measured in both the high-energy UV region (200 nm – 250 nm) and the low energy UV region (340 nm – 440 nm), as compared to those properties for commercial anatase (*Acros Organics*).

The applicability of laser processing to other oxide and non-oxide ceramics, with and without doping, also seems achievable. For example, to synthesize amorphous Al_2O_3 nanoparticles or films, a suitable liquid precursor may be aluminum isopropoxide, whereas to synthesize amorphous SiC, Si_3N_4 and SiC_XN_Y hexamethyldisilazane is a good prospect. Another area of interest is laser processing of high-pressure phases, such as cubic-BN and

diamond. As for suitable liquid precursors, hexane may be a good choice for diamond synthesis and borazine for cubic-BN synthesis

References

(1) Hadjiivanov, K. I.; Klissurski, D. G., Surface chemistry of titania (anatase) and titania-supported catalysts. *Chemical Society Reviews* **1996,** 25, (1), 61-69.

(2) Liu, N.; Chen, X.; Zhang, J.; Schwank, J. W., A review on TiO 2-based nanotubes synthesized via hydrothermal method: formation mechanism, structure modification, and photocatalytic applications. *Catalysis Today* **2014,** 225, 34-51.

(3) Diamandescu, L.; Vasiliu, F.; Tarabasanu-Mihaila, D.; Feder, M.; Vlaicu, A.; Teodorescu, C.; Macovei, D.; Enculescu, I.; Parvulescu, V.; Vasile, E., Structural and photocatalytic properties of iron-and europium-doped TiO 2 nanoparticles obtained under hydrothermal conditions. *Materials Chemistry and Physics* **2008,** 112, (1), 146-153.

(4) Benoit, A.; Paramasivam, I.; Nah, Y.-C.; Roy, P.; Schmuki, P., Decoration of TiO 2 nanotube layers with WO 3 nanocrystals for high-electrochromic activity. *Electrochemistry Communications* **2009,** 11, (4), 728-732.

(5) Carp, O.; Huisman, C. L.; Reller, A., Photoinduced reactivity of titanium dioxide. *Progress in solid state chemistry* **2004,** 32, (1), 33-177.

(6) Simons, P.; Dachille, F., The structure of TiO2II, a high-pressure phase of TiO2. *Acta Crystallographica* **1967,** 23, (2), 334-336.

(7) Latroche, M.; Brohan, L.; Marchand, R.; Tournoux, M., New hollandite oxides: TiO2 (H) and K0. 06TiO2. *Journal of Solid State Chemistry* **1989,** 81, (1), 78-82.

(8) Muscat, J.; Swamy, V.; Harrison, N. M., First-principles calculations of the phase stability of TiO 2. *Physical Review B* **2002,** 65, (22), 224112.

(9) Tanaka, K.; Capule, M. F.; Hisanaga, T., Effect of crystallinity of TiO2 on its photocatalytic action. *Chemical Physics Letters* **1991,** 187, (1-2), 73-76.

(10) Kho, Y. K.; Iwase, A.; Teoh, W. Y.; Mädler, L.; Kudo, A.; Amal, R., Photocatalytic H2 evolution over TiO2 nanoparticles. The synergistic effect of anatase and rutile. *The Journal of Physical Chemistry C* **2010,** 114, (6), 2821-2829.

(11) Li, G.; Chen, L.; Graham, M. E.; Gray, K. A., A comparison of mixed phase titania photocatalysts prepared by physical and chemical methods: the importance of the solid–solid interface. *Journal of Molecular Catalysis A: Chemical* **2007,** 275, (1), 30-35.

(12) Lehtinen, K. E.; Zachariah, M. R., Energy accumulation in nanoparticle collision and coalescence processes. *Journal of Aerosol Science* **2002,** 33, (2), 357-368.

(13) Cho, I. S.; Choi, J.; Zhang, K.; Kim, S. J.; Jeong, M. J.; Cai, L.; Park, T.; Zheng, X.; Park, J. H., Highly efficient solar water splitting from transferred TiO2 nanotube arrays. *Nano letters* **2015,** 15, (9), 5709-5715.

(14) Tolmachoff, E.; Memarzadeh, S.; Wang, H., Nanoporous titania gas sensing films prepared in a premixed stagnation flame. *The Journal of Physical Chemistry C* **2011,** 115, (44), 21620-21628.

(15) Zhang, Y.; Li, S.; Deng, S.; Yao, Q.; Tse, S. D., Direct synthesis of nanostructured TiO2 films with controlled morphologies by stagnation swirl flames. *Journal of Aerosol Science* **2012,** 44, 71-82.

(16) Cho, I. S.; Chen, Z.; Forman, A. J.; Kim, D. R.; Rao, P. M.; Jaramillo, T. F.; Zheng, X., Branched TiO2 nanorods for photoelectrochemical hydrogen production. *Nano letters* **2011,** 11, (11), 4978-4984.

(17) Ragai, J.; Lotfi, W., Effect of preparative pH and ageing media on the crystallographic transformation of amorphous TiO2 to anatase and rutile. *Colloids and surfaces* **1991,** 61, 97-109.

(18) Wang, C.-C.; Ying, J. Y., Sol− gel synthesis and hydrothermal processing of anatase and rutile titania nanocrystals. *Chemistry of Materials* **1999,** 11, (11), 3113-3120.

(19) Wang, C.; Li, Q.; Wang, R.-D., Synthesis and characterization of mesoporous TiO 2 with anatase wall. *Materials Letters* **2004,** 58, (9), 1424-1426.

(20) Zhao, H.; Liu, X.; Tse, S. D., Control of nanoparticle size and agglomeration through electric-field-enhanced flame synthesis. *Journal of Nanoparticle Research* **2008,** 10, (6), 907-923.

(21) Zhao, H.; Liu, X.; Tse, S. D., Effects of pressure and precursor loading in the flame synthesis of titania nanoparticles. *Journal of Aerosol Science* **2009,** 40, (11), 919-937.

(22) Hardt, S.; Wlokas, I.; Schulz, C.; Wiggers, H., Impact of Ambient Pressure on Titania Nanoparticle Formation During Spray-Flame Synthesis. *Journal of nanoscience and nanotechnology* **2015,** 15, (12), 9449-9456.

(23) Skandan, G.; Chen, Y.; Glumac, N.; Kear, B., Synthesis of oxide nanoparticles in low pressure flames. *Nanostructured materials* **1999,** 11, (2), 149-158.

(24) Siegel, R.; Ramasamy, S.; Hahn, H.; Zongquan, L.; Ting, L.; Gronsky, R., Synthesis, characterization, and properties of nanophase TiO2. *Journal of Materials Research* **1988,** 3, (6), 1367-1372.

(25) Chen, Q.; Qian, Y.; Chen, Z.; Zhou, G.; Zhang, Y., Preparation of TiO2 powders with different morphologies by an oxidation-hydrothermal combination method. *Materials Letters* **1995,** 22, (1-2), 77-80.

(26) Wegner, K.; Pratsinis, S. E., Nozzle-quenching process for controlled flame synthesis of titania nanoparticles. *AIChE Journal* **2003,** 49, (7), 1667-1675.

(27) O'regan, B.; Grätzel, M., A low-cost, high-efficiency solar cell based on dye-sensitized colloidal TiO 2 films. *nature* **1991,** 353, (6346), 737-740.

(28) Kasuga, T.; Hiramatsu, M.; Hoson, A.; Sekino, T.; Niihara, K., Formation of titanium oxide nanotube. *Langmuir* **1998,** 14, (12), 3160-3163.

(29) Zwilling, V.; Darque-Ceretti, E.; Boutry-Forveille, A.; David, D.; Perrin, M.-Y.; Aucouturier, M., Structure and physicochemistry of anodic oxide films on titanium and TA6V alloy. *Surface and Interface Analysis* **1999,** 27, (7), 629-637.

(30) Bavykin, D. V.; Lapkin, A. A.; Plucinski, P. K.; Friedrich, J. M.; Walsh, F. C., Reversible storage of molecular hydrogen by sorption into multilayered TiO2 nanotubes. *The Journal of Physical Chemistry B* **2005,** 109, (41), 19422-19427.

(31) Yu, J.; Yu, H.; Cheng, B.; Trapalis, C., Effects of calcination temperature on the microstructures and photocatalytic activity of titanate nanotubes. *Journal of Molecular Catalysis A: Chemical* **2006,** 249, (1), 135-142.

(32) Bavykin, D. V.; Friedrich, J. M.; Lapkin, A. A.; Walsh, F. C., Stability of aqueous suspensions of titanate nanotubes. *Chemistry of materials* **2006,** 18, (5), 1124-1129.

(33) Anastasescu, C.; Mihaiu, S.; Preda, S.; Zaharescu, M., Synthesis of Oxide Nanotubes/Nanorods by Hydrothermal Method. In *1D Oxide Nanostructures Obtained by Sol-Gel and Hydrothermal Methods*, Springer: 2016; pp 21-75.

(34) Rajeshwar, K.; Osugi, M.; Chanmanee, W.; Chenthamarakshan, C.; Zanoni, M. V. B.; Kajitvichyanukul, P.; Krishnan-Ayer, R., Heterogeneous photocatalytic treatment of

organic dyes in air and aqueous media. *Journal of photochemistry and photobiology C: photochemistry reviews* **2008,** 9, (4), 171-192.

(35) Likodimos, V.; Stergiopoulos, T.; Falaras, P.; Kunze, J.; Schmuki, P., Phase composition, size, orientation, and antenna effects of self-assembled anodized titania nanotube arrays: a polarized micro-Raman investigation. *The Journal of Physical Chemistry C* **2008,** 112, (33), 12687-12696.

(36) Kobayashi, S.; Hanabusa, K.; Hamasaki, N.; Kimura, M.; Shirai, H.; Shinkai, S., Preparation of TiO2 hollow-fibers using supramolecular assemblies. *Chemistry of materials* **2000,** 12, (6), 1523-1525.

(37) Jung, J. H.; Kobayashi, H.; van Bommel, K. J.; Shinkai, S.; Shimizu, T., Creation of novel helical ribbon and double-layered nanotube TiO2 structures using an organogel template. *Chemistry of materials* **2002,** 14, (4), 1445-1447.

(38) Peng, T.; Hasegawa, A.; Qiu, J.; Hirao, K., Fabrication of titania tubules with high surface area and well-developed mesostructural walls by surfactant-mediated templating method. *Chemistry of Materials* **2003,** 15, (10), 2011-2016.

(39) Fujikawa, S.; Kunitake, T., Surface fabrication of hollow nanoarchitectures of ultrathin titania layers from assembled latex particles and tobacco mosaic viruses as templates. *Langmuir* **2003,** 19, (16), 6545-6552.

(40) Albu, S. P.; Ghicov, A.; Macak, J. M.; Hahn, R.; Schmuki, P., Self-organized, free-standing TiO2 nanotube membrane for flow-through photocatalytic applications. *Nano letters* **2007,** 7, (5), 1286-1289.

(41) Roy, P.; Berger, S.; Schmuki, P., TiO2 nanotubes: synthesis and applications. *Angewandte Chemie International Edition* **2011,** 50, (13), 2904-2939.

(42) Yan, J.; Zhou, F., TiO 2 nanotubes: structure optimization for solar cells. *Journal of Materials Chemistry* **2011,** 21, (26), 9406-9418.

(43) Kasuga, T.; Hiramatsu, M.; Hoson, A.; Sekino, T.; Niihara, K., Titania nanotubes prepared by chemical processing. *Advanced Materials* **1999,** 11, (15), 1307-1311.

(44) Yan, J.; Feng, S.; Lu, H.; Wang, J.; Zheng, J.; Zhao, J.; Li, L.; Zhu, Z., Alcohol induced liquid-phase synthesis of rutile titania nanotubes. *Materials Science and Engineering: B* **2010,** 172, (2), 114-120.

(45) Mozia, S., Application of temperature modified titanate nanotubes for removal of an azo dye from water in a hybrid photocatalysis-MD process. *Catalysis Today* **2010,** 156, (3), 198-207.

(46) Govindaraj, R.; Santhosh, N.; Pandian, M. S.; Ramasamy, P., Synthesis of nanocrystalline TiO 2 nanorods via hydrothermal method: An efficient photoanode material for dye sensitized solar cells. *Journal of Crystal Growth* **2017,** 468, 125-128.

(47) Pradhan, S. K.; Reucroft, P. J.; Yang, F.; Dozier, A., Growth of TiO 2 nanorods by metalorganic chemical vapor deposition. *Journal of Crystal Growth* **2003,** 256, (1), 83-88.

(48) Limmer, S. J.; Cao, G., Sol–gel electrophoretic deposition for the growth of oxide nanorods. *Advanced Materials* **2003,** 15, (5), 427-431.

(49) Attar, A. S.; Ghamsari, M. S.; Hajiesmaeilbaigi, F.; Mirdamadi, S.; Katagiri, K.; Koumoto, K., Synthesis and characterization of anatase and rutile TiO2 nanorods by template-assisted method. *Journal of Materials Science* **2008,** 43, (17), 5924-5929.

(50) Chen, X.; Mao, S. S., Titanium dioxide nanomaterials: synthesis, properties, modifications, and applications. *Chem. Rev* **2007,** 107, (7), 2891-2959.

(51) Ren, W.; Ai, Z.; Jia, F.; Zhang, L.; Fan, X.; Zou, Z., Low temperature preparation and visible light photocatalytic activity of mesoporous carbon-doped crystalline TiO 2. *Applied Catalysis B: Environmental* **2007,** 69, (3), 138-144.

(52) Sakthivel, S.; Kisch, H., Daylight photocatalysis by carbon-modified titanium dioxide. *Angewandte Chemie International Edition* **2003,** 42, (40), 4908-4911.

(53) Wu, Z.; Dong, F.; Zhao, W.; Wang, H.; Liu, Y.; Guan, B., The fabrication and characterization of novel carbon doped TiO2 nanotubes, nanowires and nanorods with high visible light photocatalytic activity. *Nanotechnology* **2009,** 20, (23), 235701.

(54) Xiao, Q.; Zhang, J.; Xiao, C.; Si, Z.; Tan, X., Solar photocatalytic degradation of methylene blue in carbon-doped TiO 2 nanoparticles suspension. *Solar Energy* **2008,** 82, (8), 706-713.

(55) Chu, D.; Yuan, X.; Qin, G.; Xu, M.; Zheng, P.; Lu, J.; Zha, L., Efficient carbon-doped nanostructured TiO2 (anatase) film for photoelectrochemical solar cells. *Journal of Nanoparticle Research* **2008,** 10, (2), 357-363.

(56) Yang, J.; Bai, H.; Tan, X.; Lian, J., IR and XPS investigation of visible-light photocatalysis—Nitrogen–carbon-doped TiO 2 film. *Applied Surface Science* **2006,** 253, (4), 1988-1994.

(57) Wu, B.; Liu, D.; Mubeen, S.; Chuong, T. T.; Moskovits, M.; Stucky, G. D., Anisotropic growth of TiO2 onto gold nanorods for plasmon-enhanced hydrogen production from water reduction. Journal of the American Chemical Society 2016, 138, (4), 1114-1117.

(58) Pennington, A. M.; Okonmah, A. I.; Munoz, D. T.; Tsilomelekis, G.; Celik, F. E., Changes in Polymorph Composition in P25-TiO2 during Pretreatment Analyzed by Differential Diffuse Reflectance Spectral Analysis. The Journal of Physical Chemistry C 2018, 122, (9), 5093-5104.

Chapter Four

Synthesis of Tungsten-Doped TiO_2 Nanopowders

4.1 Introduction

Among the many photocatalytic materials, TiO_2 may be close to being ideal. However, a shortcoming for it involves solar applications, where it its inefficient at absorbing visible radiation [1]. Because of its large band gap, TiO_2 absorbs light in the UV portion of the solar spectrum, which is only 4% of the emission [2]. To overcome this aspect, it has been proposed that the band-gap energy can be reduced by doping, coupling, and capping of TiO_2 nanoparticles [1].

Doping TiO_2 with various transition metals (Cr, V, Ag, W, etc.) has been investigated to increase photocatalytic activity in the visible-light range by introducing additional energy levels in the band-gap structure of TiO_2 [3, 4]. In addition, transition metals improve the activity of TiO_2 photocatalysts by inhibiting electron-hole recombination, which increases the number of electrons flowing to the other electrode [5]. Moreover, such doping enhances the surface properties of TiO_2 and increases photocatalytic activity by increasing the surface acidity and area [6]. The presence of oxygen vacancies is also considered to be crucial to the improvement of photoactivity of TiO_2 [7]. However, the efficiency of a dopant is affected by several parameters, including concentration and distribution of the dopant in the TiO_2 matrix, creation of additional energy levels in the band-gap structure, and electron

donor concentration [8]. Moreover, concentration must be closely monitored as excess of dopant decreases photocatalytic activity, since charge recombination becomes favorable [9].

Tungsten is one of several transition metals used as a dopant in TiO_2. As the ionic radius of tungsten (W^{6+}) is quite similar to that of titanium (Ti^{4+}), tungsten ions are easily inserted into the TiO_2 lattice without significant distortion of the structure [10]. The presence of WO_3 in the lattice of TiO_2 plays an important role in increasing surface acidity and in providing an effective separation site for photo-generated charge carriers. In addition, the electronic structure of TiO_2 is modified by substitutional doping with higher-valence cations like tungsten, which results in a higher charge-separation efficiency [11]. Therefore, doping of W into the TiO_2 lattice effectively increases photocatalytic activity of TiO_2 [12].

Because of these benefits, many recent reports have focused on W-doped TiO_2 nanoparticles to enhance photoactivity under visible light irradiation. Park et al. [10] reported that doping TiO_2 with W by chemical vapor synthesis increases photocatalytic activity by 18%, as compared to commercial TiO_2. Many techniques have been utilized to dope TiO_2 with W. Sol-gel synthesis has been used to prepare and dope TiO_2 nanoparticles with W ions. Using a dip-coating procedure, Yolanda at el. [13] prepared TiO_2 doped with Ca^{2+}, W^{6+} and N_2. They reported that given the ionic radii similarity of both tungsten ions (W^{6+}) and titanium ions (Ti^{4+}), W^{6+} ions easily replace Ti^{4+} and cause excess charge in the lattice. Replacing Ti^{4+} in TiO_2 with a cation may be easier than to substitute O^{2-} with an anion as a result of the difference in charge state and ionic radius [14]. Reduction in the recombination of electron-hole (e^-/h^+) pairs increases the photocatalytic activity of W-TiO_2 nanoparticles.

Sanjayan et al. [15] doped TiO_2 with W by aerosol-assisted CVD, showing that the presence of W in TiO_2 films enhances photocatalytic and opto-electronic properties. They claimed that the increase in photocatalytic activity is due to increase in surface structure and decrease in grain boundary area, both of which are charge-carrier recombination sites. Thapanan et al. [11] reported that W doping and hydrothermal treatment improve the visible-light photoactivity of TiO_2 synthesized by the sol-gel method. They found that TiO_2 doped at a 0.5% tungsten to titanium ratio and hydrothermally treated showed photocatalytic activity equal to 74% of commercial material under UV irradiation. Hydrothermal treatment yields crystalline TiO_2 with different compositions, structures, and morphologies, which have positive effects on TiO_2 photoactivity. W-TiO_2 nanoparticles were also prepared by thermal hydrolysis of aqueous solutions of peroxo-complexes of titanium and tungsten. Vaclav [16] reported that tungsten doping increases the temperature range of the anatase-to-rutile phase transformation by 100ºC. Other methods have been used to prepare W-TiO_2 nanoparticles, such as ion-impregnation [17, 18], hydrothermal synthesis [19] and sol-precipitation [20], in order to obtain homogenous doping of tungsten in TiO_2. However, W-TiO_2 nanoparticles often exhibit low surface area caused by close packing, thus limiting their industrial applications [21].

Nanotubes of W-TiO_2 exhibit unique features that are beneficial in photocatalysis, including high specific surface area, high pore volume, ion-exchangeable ability, rapid and long-distance electron-transport, and enhanced light absorption, attributable to the high ratio of length-to-tube diameter [22-25]. Compared to nanoparticles, nanotubes can be more attractive for applications in photocatalysis [26], gas sensing [27] and solar cells [14]. The

performance of TiO_2 nanotubes can be augmented by decoration with Ag, Au and WO_3 nanoparticles [28,29]. Zhang et al. [21]prepared tungsten-nitrogen co-doped TiO_2 nanotube arrays using anodization and hydrothermal synthesis methods. It was observed that tungsten in co-doped arrays exists as W^{6+} by substituting for Ti^{4+} in the lattice of TiO_2, while nitrogen exists in the form of Ti-N-O. Tungsten ions are considered to act as trapping sites that help to decrease the recombination rate of electrons and holes, which leads to improved photocatalytic activity. Das et al. [30] studied the influence of WO_3 doping on the photocatalytic behavior of TiO_2 nanotube layers. They concluded that tungsten oxide in the structure introduces a photocurrent that strongly enhances the photocatalytic activity. They also found that high WO_3 content deactivates or decreases the photocatalytic performance.

In this study, W-doped TiO_2 nanopowders are prepared by laser ablation of a tungsten foil immersed in liquid titanium tetra-isopropoxide (TTIP) precursor. The photochemical activity is studied by UV-Vis spectroscopy under visible light irradiation. The results demonstrate that the W-doped TiO_2 nanopowders exhibit higher photochemical activity than un-doped TiO_2. The effects of heat-treatment in ambient air on structure and photochemical properties are also investigated. It is observed that W doping of TiO_2 increases the temperature of anatase-to-rutile phase transformation by about 150 ºC compared to that of un-doped TiO_2.

4.2 Experimental Work

4.2.1 Tungsten-doped TiO_2 synthesis

Nanostructured powders of W-TiO_2 are synthesized by pulsed-laser ablation of a tungsten foil (0.05 mm thick, 99.95% purity) immersed in liquid titanium tetra-isopropoxide (TTIP, 99.5% purity). In this process (Figure 0.1), the W-foil serves as a rotating target, and the Nd:YAG pulsed laser (wavelength 532 nm, maximum pulse energy 500 mJ/pulse) ablates the tungsten foil while simultaneously decomposing the precursor liquid. In practice, about 2 mL of liquid TTIP precursor in the inner container is shrouded with flowing N_2, which serves to prevent its reaction with ambient air. Nd:YAG pulsed laser is focused on the W-target surface to decompose the liquid precursor, thereby forming a high concentration of vaporized species of W-TiO_2 within a submerged plasma, which then experience rapid condensation/quenching by the surrounding un-reacted and chilled liquid-TTIP precursor solution.

To keep the temperature of the TTIP constant during processing, the container is water cooled. After 45 min of operation, a suspension of nanoparticles is formed in the liquid precursor, which is extracted by centrifuging at 1500 rpm for 10 min.

Small samples of as-synthesized W-doped TiO_2 nanoparticles, before and after heat treatment, are characterized for composition, structure, and morphology, using conventional analytical techniques, such as X-ray diffraction (XRD), X-ray photoelectron spectroscopy (XPS), UV-Visible spectroscopy, and scanning transmission electron

microscopy (STEM). Heat treatments are performed at 400-1050 ºC for 2 hours in an oven with ambient air as well as in a furnace with 100 ml/min nitrogen flow. Photochemical activity is measured by liquid-phase methylene-blue degradation, under ultraviolet illumination, visible light illumination, and no illumination (dark) conditions.

4.2.2 Methylene Blue (MB) degradation

Methylene blue (MB) degradation experiments are carried out in an aqueous solution. of 3.4 ppm MB, formed by diluting stock solution with DI water. The reaction vessel for the batch MB reactions, a 3.5 ml quartz Cuvette, is filled with 3 mL of 3.4 ppm MB; and then catalyst is added to the reaction vessel with specific masses given in Table 0-4 . Reactions are carried out at room temperature under constant stirring to ensure homogeneity under either no illumination (Dark) or ultraviolet illumination (UV) using a 150 W Xenon Ozone-free Arc Lamp equipped with a beam turner reflector for UV (280 nm-400 nm, Newport) or visible (420 nm-600 nm, Newport) light source. Additionally, a colored glass filter for UV (FSQ-UG5, Newport) and visible (KG1, Newport) is employed to ensure that the catalyst bed was only illuminated with specific wavelengths. For dark reactions, the reaction vessel is immediately wrapped in aluminum foil and monitored at ambient conditions for 60 min.

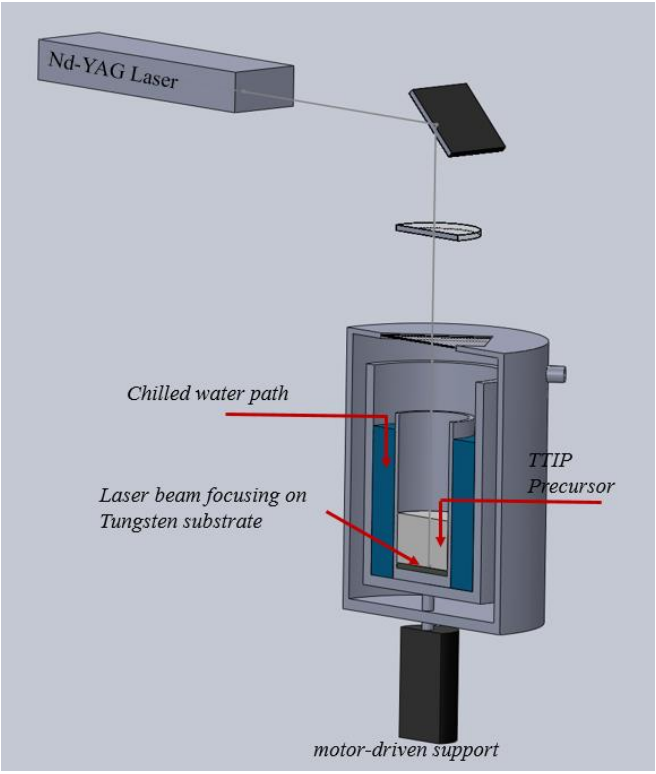

Figure 0.1. Schematic diagram of the experimental setup of Laser ablation Tungsten substrate immersed in Titanium isopropoxide precursor showing the laser focused on the Tungsten foil

Degradation was monitored via measuring transmittance of the reaction cell using the UV-Visible Spectrophotometer (Thermo Evolution 3600) every 5 minutes for the duration of the 60 minute reaction. The degradation of methylene blue is monitored measuring transmittance, calculating the percent absorbance, and using an in-house calibration curve, to determine the concentration of Methylene Blue (MB) in ppm via UV-Visible Spectroscopy. Each reaction batch was run with 3 ml of fresh MB and fresh catalyst (masses denoted in Table 0-4). Upon addition of the catalyst to the cuvette, MB is added, the sample is stirred, and the catalyst is allowed to sink to the bottom of the

cuvette, where the xenon arc lamp is focused, ensuring maximum absorbance of photons and minimum interference with the transmittance of the UV-vis scans. All catalytic reactions are run at room temperature, and the Xenon Arc beam is focused to a spot size of roughly 3 cm, illuminating the base of the cuvette.

4.3 Results and Discussion

As synthesized W-TiO_2 nanopowder, irrespective of its morphology, exhibits an amorphous-like structure. XRD patterns of W-TiO_2, after heat treatments at 400-1050ºC are shown in Figure 0.2. An amorphous-to-anatase phase change occurs at 400 ºC; and an anatase-to-rutile phase change occurs at 950 ºC, with no indication for any other phases. The evidence supports the widely accepted view that W^{6+} ions substitute for Ti^{4+} ions in both anatase- and rutile-TiO_2 phases. Moreover, the average crystallite size of TiO_2 (about 13 nm) is slightly reduced by doping with W (10 nm). Reduction in crystallite size by W doping has been observed by other groups [158, 159].

Table 0-. 0-1Cell parameters comparison			
TiO_2	a (A°)	c (A°)	Unit Cell Volume (A°)
TiO_2, 400°C	3.781	9.4541	135.16
W- TiO_2, 400°C	3.7825	9.433	134.9

Table 0-2. Phases formed after heat treatment (A: Anatase and R: Rutile)					
Sample	400°C	700°C	800°C	950°C	1050°C
TiO_2	A	A	A + R	R	R
W-TiO_2	A	A	A	A + R	R

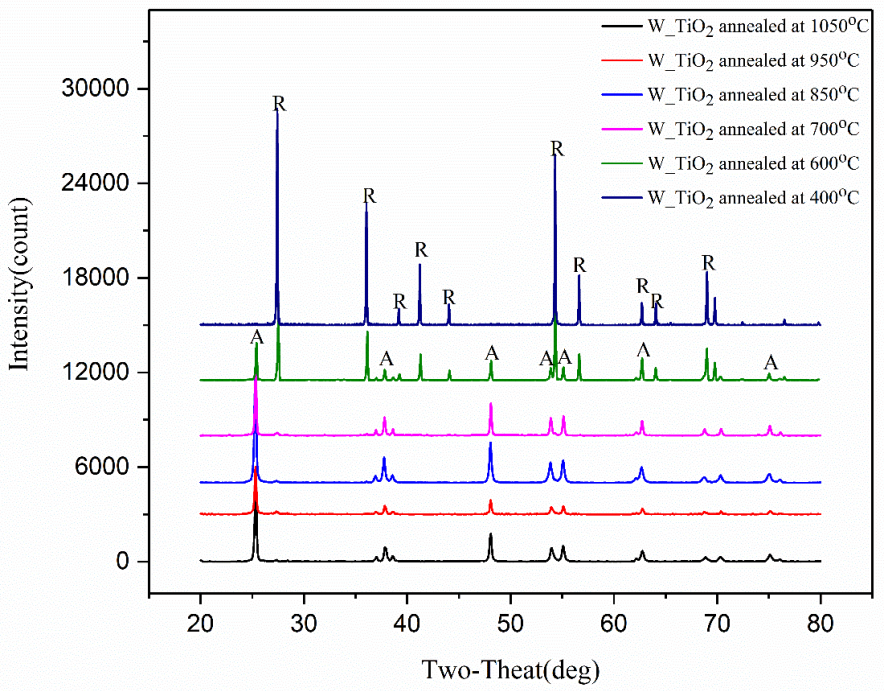

Figure 0.2. XRD pattern of W-doped TiO_2 annealed in air for 2 hr at different temperatures (A: anatase and R: rutile).

It has been reported by other researchers that W doping of TiO_2 retards the anatase-to-rutile phase transformation [20, 31]. In agreement with this prior work, phase transformation of our W-TiO_2 occurs at 950 °C, which is about 150 ºC higher than that of TiO_2. Doping TiO_2 with W also reduces crystal growth, as shown by the lower anatase peak in a doped sample in comparison with that of an un-doped sample, Figure 0.3. Wu et al. [32] reported that W^{6+} ions can occupy interstitial sites in the TiO_2 crystal lattice, which, by decreasing the number of oxygen vacancies, retards both phase transformation and crystal growth.

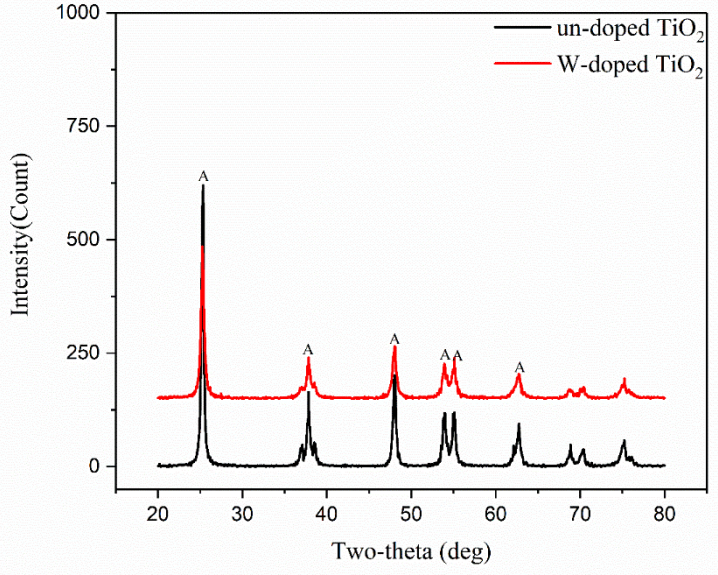

Figure 0.3. XRD patterns of un-doped TiO_2 vs W-doped TiO_2

Calculated unit cell volumes for TiO_2 and W-TiO_2 are given in Table 4.1. As indicated, unit-cell parameters (*a* and *c)* of W-TiO_2 are slightly smaller than that of TiO_2, which has also been reported by another group [18]. Since the ionic radius of W^{6+} (0.60 Å) is quite similar to Ti^{4+} (0.68 Å) [33], most W^{6+} ions occupy substitutional sites in the TiO_2 lattice. Moreover, XPS analysis shows that the doped powder contains tungsten in the 6+ oxidation state.

X-ray photoelectron spectroscopy XPS is used to determine the oxidation state of the O *1s*, Ti *2p*, and W *4f*. The XPS spectra of O *1s* and Ti *2p* of the heat treated un-doped and W-doped TiO_2 nanopowder are shown in Figure 0.4. Binding energies of O *1s* are observed at 530.09 eV and 531.82 eV. The binding energy of 530.09 eV is assigned to the Ti-O bond, whereas the binding energy of 531.82 eV is assigned to O bonded to Ti^{3+} [34]. The binding energies of Ti *2p* in un-doped TiO_2 are observed at 458.3 eV and 464.02 eV. For

the as-synthesized W-TiO_2, both the Ti *2p* and O *1s* peaks are slightly shifted toward higher binding energy owing to the doping of W in the TiO_2 lattice, which is consistent with the result reported by Gong et al. [35]. The tungsten-doped TiO_2 sample shows three oxygen species, at 530.61 eV, 532.23 eV and 533.35 eV, respectively. The new peak at 533.2 eV corresponds to adsorbed oxygen species. Park et al. [10] also found the formation of the new peak for tungsten doped TiO_2 nanopowder. Since the surface acidity of WO_3 is 15 times higher than that of TiO_2 [36], W-doped TiO_2 likely contains more hydroxyl groups than does non-doped TiO_2.

The chemical state of tungsten in W-doped TiO_2 nanopowder changes with annealing temperature, Figure 0.5. XPS scans of W-doped anatase TiO_2 showing influence of heat treatment: (a) 400ºC; (b) 600°C; (c) 700°C; and (d) 800ºC.. Tungsten-doped TiO_2 heat treated at 400 ºC exhibits W 4*f* binding energy at 37.8 eV, which corresponds to the W^{6+} of WO_3 chemical state [37]. After heat treatment at 600° C, the W peak shifts to 36.9 eV, indicating migration of tungsten to the surface of the TiO_2. Annealing at 700° C yields new peaks at 35.49 eV and 37.32 eV, which correspond to W^{6+} of WO_3 chemical state. Chen et al. [38] found XPS peaks for tungsten in W-doped anatase TiO_2 at 35.4 and 37.6 eV, which were assigned to the W^{6+} *4f7/2*, W^{6+} *4f5/2* states, respectively. Park et al. [10] reported the formation of non-stoichiometric tungsten binding energy after heat treatment of W- doped TiO_2 nanopowder, prepared by chemical vapor synthesis. Upon annealing to 800°C, the peak at 35.49 eV disappears, indicating that it was oxidized back to a higher oxidation-state. Other researchers have observed that WO_3 is stable at 400°C, but fluctuation of its chemical states occurs at higher temperature [36, 39, 40]. On the other hand, the absence of a tungsten-related phase in the XRD pattern, even after heat treatment of the nanopowder at

high temperatures, and the observation of tungsten in XPS, further illustrates that tungsten is incorporated into the lattices of both anatase and rutile TiO_2

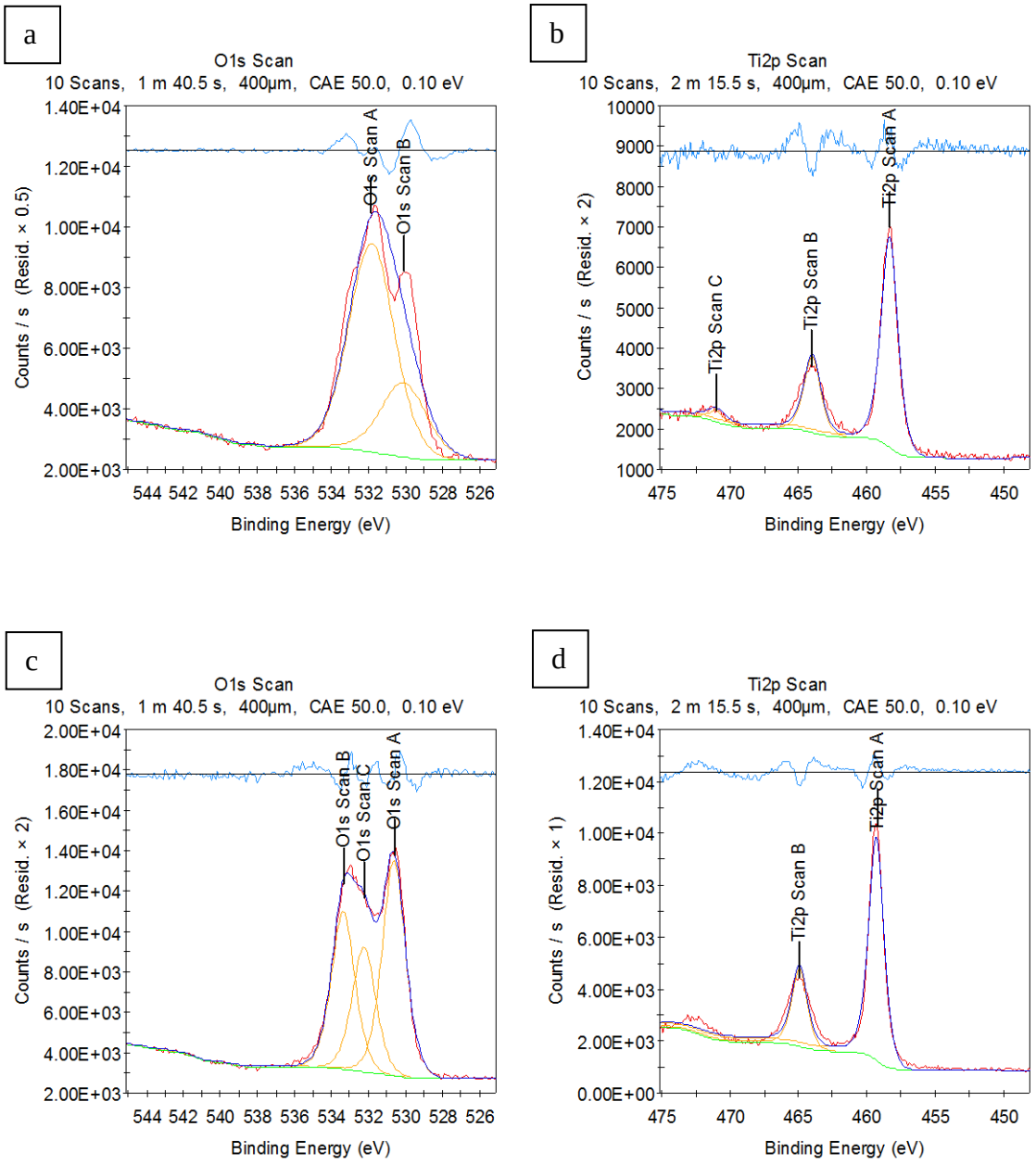

Figure 0.4. XPS spectra of O 1s and Ti 2p binding level energy of TiO_2 and W-doped TiO_2, both annealed at 400°C for 2 hours. (a) O_2 1s binding energy in non-doped TiO_2, (b) Ti 2p in non-doped TiO_2, (c) O_2 in W-doped TiO_2 and (d) Ti 2p in W-doped TiO_2.

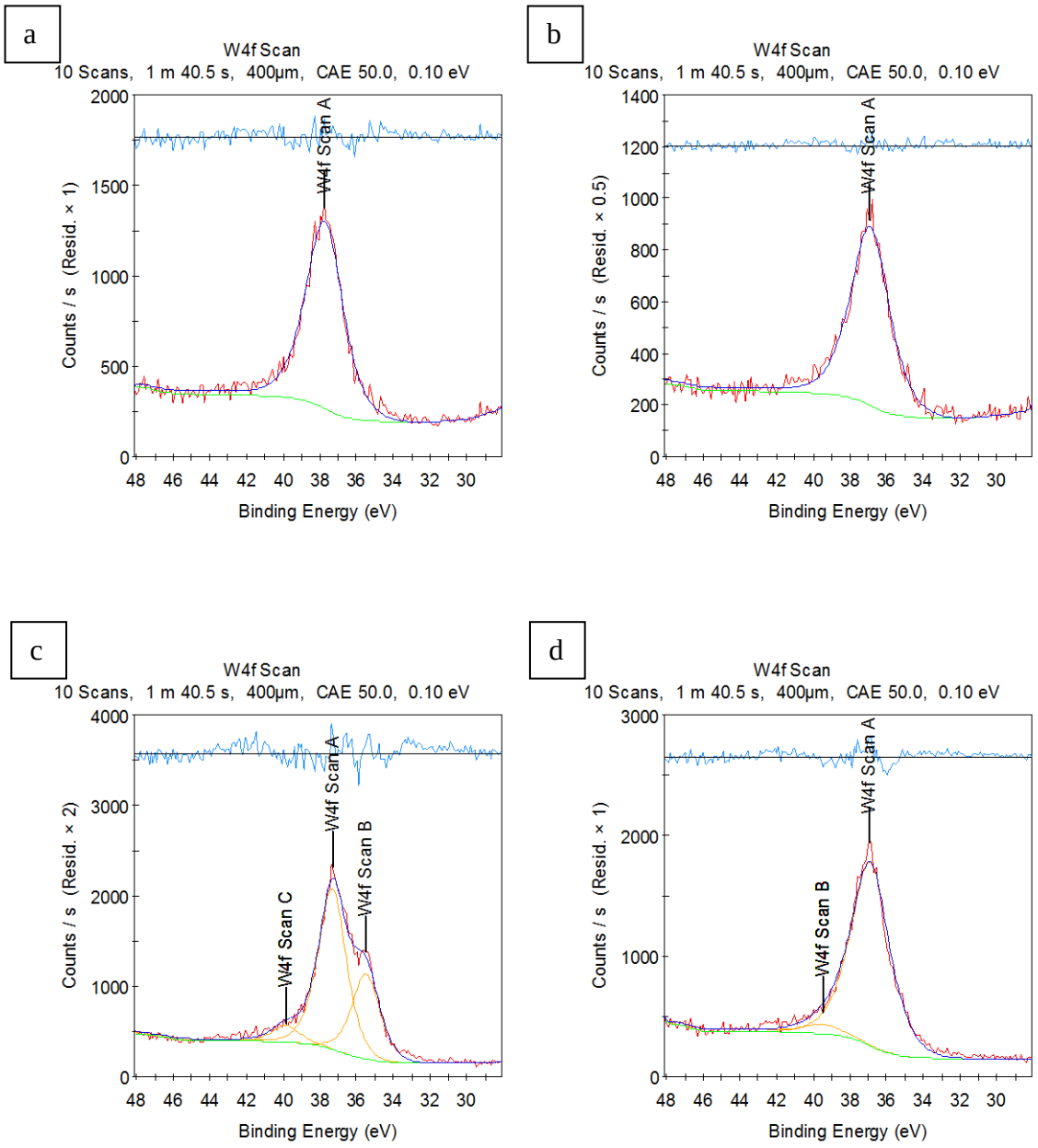

Figure 0.5. XPS scans of W-doped anatase TiO_2 showing influence of heat treatment: (a) 400ºC; (b) 600°C; (c) 700°C; and (d) 800ºC.

As-synthesized amorphous W-doped TiO_2 nanoparticles, post-annealed at 400ºC for 2 hr in air, transform into nanocrystalline anatase-TiO_2. As discussed in the preceding chapter, this phase transformation is shown to occur via a layer-by-layer crystalline-growth mechanism, starting at the nanoparticle surface and propagating uniformly into the interior. The resulting image shows a radially-symmetric (pie-shaped) crystalline structure.

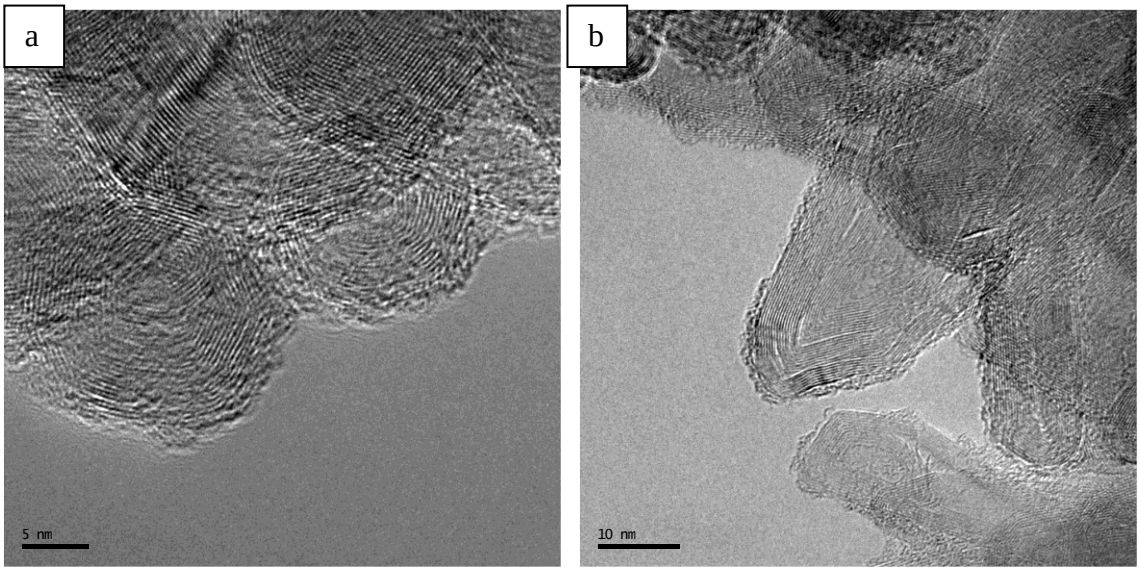

Figure 0.6:W-doped TiO_2 nanoparticles, after annealing at 400ºC/2 hrs in air, showing radially-symmetric nanocrystalline structure. TEM Images collected with the help of Zhizhong Dong.

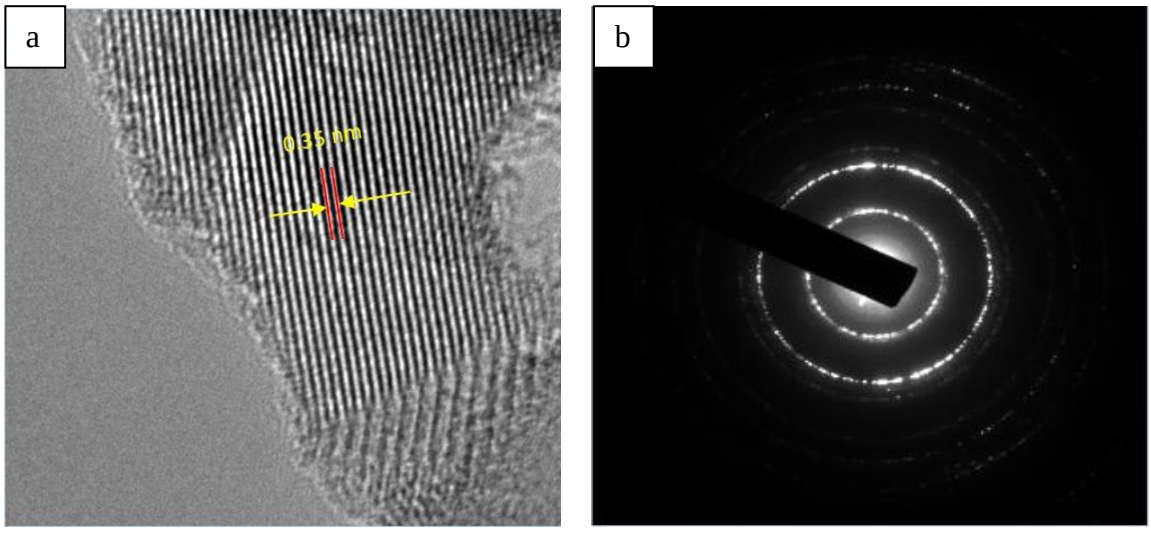

Figure 0.7. (a) Lattice image of a well-crystallized nanoparticle, showing d-spacing of 0.35 nm, in agreement with XRD, and (b) spotty-ring pattern indicative of a random nanocrystalline structure. TEM Images collected with the help of Zhizhong Dong.

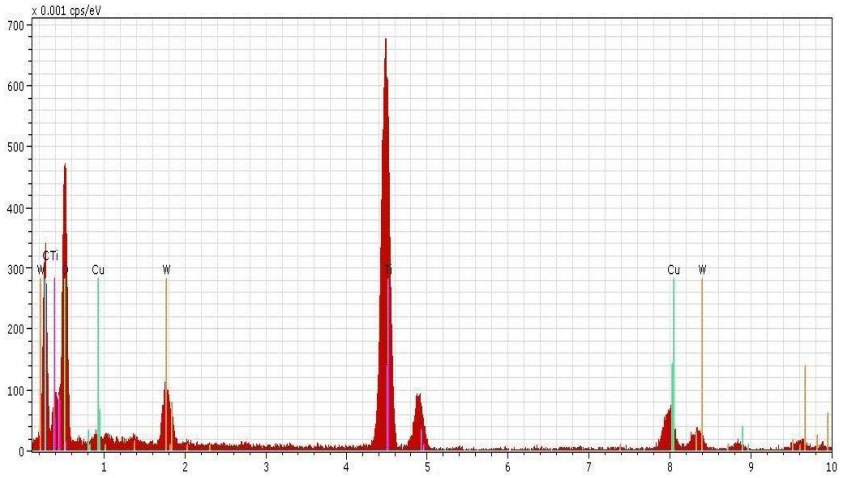

Figure 0.8. EDS spectra of nanocrystalline W-doped TiO_2, confirming the presence of W in the host lattice.

STEM images of partially crystallized anatase-TiO_2 nanoparticles, is shown in Figure 0.6*Figure* 0.6:W-doped TiO2 nanoparticles, after annealing at 400ºC/2 hrs in air,

showing radially-symmetric nanocrystalline structure. Lattice imaging of a well-crystallized nanoparticle, with corresponding SAED pattern is shown in **Figure** 0.7. (a) Lattice **image** of a well-crystallized nanoparticle, showing d-spacing of 0.35 nm, in agreement with XRD, and (b) spotty-ring pattern indicative of a random nanocrystalline structure.. The measured *d* spacing is 0.35 nm, which corresponds to (101) in anatase-TiO_2.

4.4 Optical Properties of W-doped TiO_2

Band gap energies are determined via diffuse-reflectance UV-Vis spectroscopy. Absolute reflectance spectra are collected between 200 nm and 800 nm in intervals of 1 nm. W-TiO_2 nanopowders are annealed in air at temperatures of 400°C, 500ºC, 600ºC, 700ºC, and 950 °C. UV-Vis spectroscopy is employed in order to compare the optical properties, including absorbance (KMU) and band gap energies, of the annealed samples along with those of the parent sample, W-TiO_2. The Kubelka Munk plot, Figure 0.9, shows a decrease in the absorbance of the high energy UV (200-350 nm) irradiation upon an increase in calcination temperature, as well as two apparent band edges in the sample annealed at 950 °C (gray), indicative of a mixture of anatase and rutile phases. The band gap energy (BGE) of each sample are determined by both the Tauc method, Figure 0.9**,** and the Diffuse Reflectance Derivative Peak Fitting (DPR) method, Figure 0.10**.**

For the Tauc method the inflection point is determined by calculating both first and second derivative to maximize accuracy of measured BGE. Band gap energies of the samples are displayed inTable 0-3. It is observed that the band gap of W-doped-TiO_2 decreases in comparison with that of un-doped TiO_2, indicating that tungsten doping indeed decreases

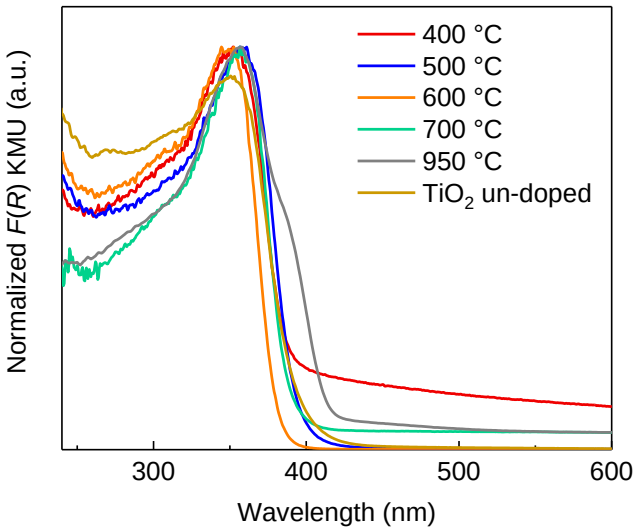

Figure 0.9. Kubelka Munk (absorbance of diffusely reflected sample) of W-TiO_2 annealed at various temperatures. Data collected with the help of Ashley Pennington

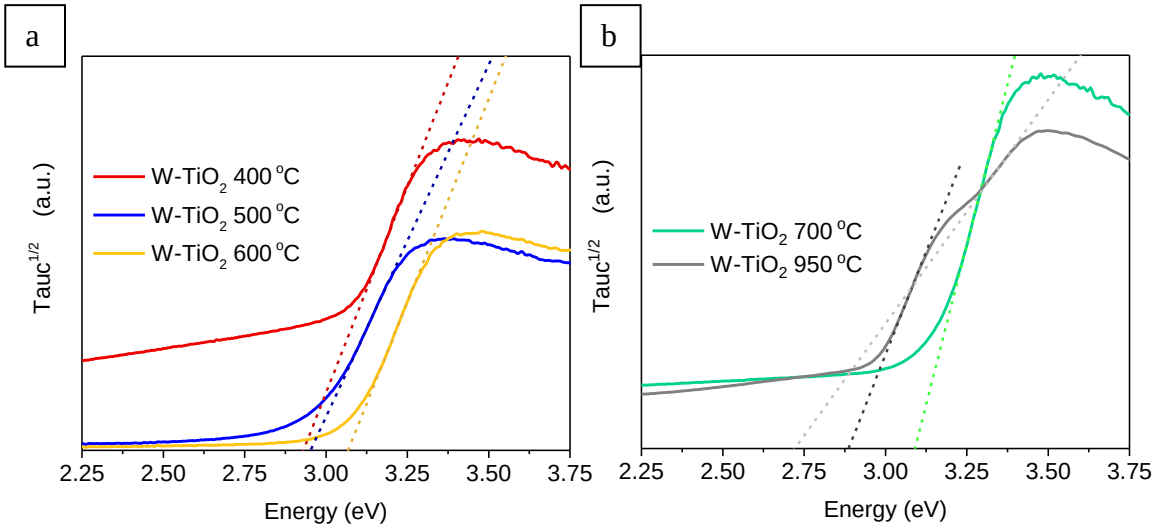

Figure 0.10. Tauc Methods for calculating indirect BGE (using $Tauc^{1/2}$) of laser-p rocessed anatase-TiO_2 nanopowder for (a) W-TiO_2 annealed between 400 °C and 600 °C, (b) W-TiO_2 annealed between 700 °C and 950 °C. Data collected with the help of Ashley Pennington

the apparent band gap energy of the sample by allowing for an increased probability of electrons lying in the tungsten fermi level as opposed to being in the valence band of the TiO_2.

The Tauc plot for W-TiO_2 at 950 °C shows two absorption onsets, indicative of two distinct oxides with BGEs far enough apart, and in high enough concentrations. XRD analysis shows both rutile and anatase phases at 950 °C. DPR analysis is used to determine BGE of both phases in each sample, which is in qualitative agreement with the Tauc BGE measurements.

Table 0-3. Band gap energies of W-TiO_2 heat treated to various temperatures using both the Tauc1/2 method for indirect BGE and the DPR method for BGE

TiO_2 Sample	$Tauc^{1/2}$ BGE (eV)	DPR Anatase BGE (eV)	DPR Rutile BGE (eV)
TiO_2	2.99	3.08	
W-TiO_2 400 °C	2.93	2.92	--
W-TiO_2 500 °C	2.95	3.12	2.89
W-TiO_2 600 °C	3.07	3.19	3.02
W-TiO_2 700 °C	3.09	3.18	3.02
W-TiO_2 950 °C	2.89, 2.72	3.16	3.02

Both Tauc and DPR show a decrease in the BGE of laser processed W-doped TiO_2 compared to laser-processed TiO_2,Table 0-3. This trend suggests that W doping of the TiO_2 lattice provides donor levels within the band gap of TiO_2, thus decreasing the effective BGE. As the annealing temperature increases in the presence of oxygen, the tungsten is converted to tungsten oxide, thus no longer being effective in decreasing the band gap, as shown by the increase in BGE with increasing annealing temperature. Table 0-4Table 0-4,

is measured for samples illuminated with UV/Vis light as well as under no illumination (dark) conditions. All catalysts exhibited minor activity in the dark reaction, from 1.4% to 9.9% conversion, indicating that there is some catalytic activity in the sample, with the sample annealed to 600 °C having the maximum conversion in the dark. Photochemical activity is monitored for both UV (280 nm - 400 nm) and Visible (420 nm – 630 nm) illumination.

Table 0-4. Methylene Blue Conversion after 40 minutes for dark (no illumination), UV, and Visible light illumination conditions for all samples

W-TiO_2 Sample	Sample Mass (mg)	Dark	UV	Visible
No Catalyst	--	1.3%	3.5%	25.4%
400 °C	14 mg	1.4%	20.9%	37.3%
500 °C	13 mg	4.5%	24.6%	36.6%
600 °C	14 mg	9.9%	35.0%	38.9%
700 °C	14 mg	6.1%	23.9%	35.7%
850 °C	12 mg	2.4%	25.6%	29.2%
950 °C	13 mg	2.9%	46.9%	30.5%

For UV illumination all samples show photochemical activity with the tendency for catalytic activity to increase (i.e., 20.9%-35.0%) with increasing annealing temperature from 400 °C to 600 °C. Then at 700 °C the photochemical activity dips to 23.9%, comparable to that for W-TiO_2 at 500 °C. From 700 °C to 950 °C, the trend is again observed that the UV-photochemical activity increases with increasing temperature, with W-TiO_2 at 950 °C being the best UV photocatalyst case at 46.9%. This result is likely due to the synergistic effect between the intimate justaposition of anatase and rutile phases in the sample inducing greater UV absorption. Samples annealed from 400 °C to 600 °C had

the largest visible light photochemical activity (i.e., 37.3-38.9%), which can be attributed to the smaller band gap promoting intermediate states in the band gap from the doped tungsten.

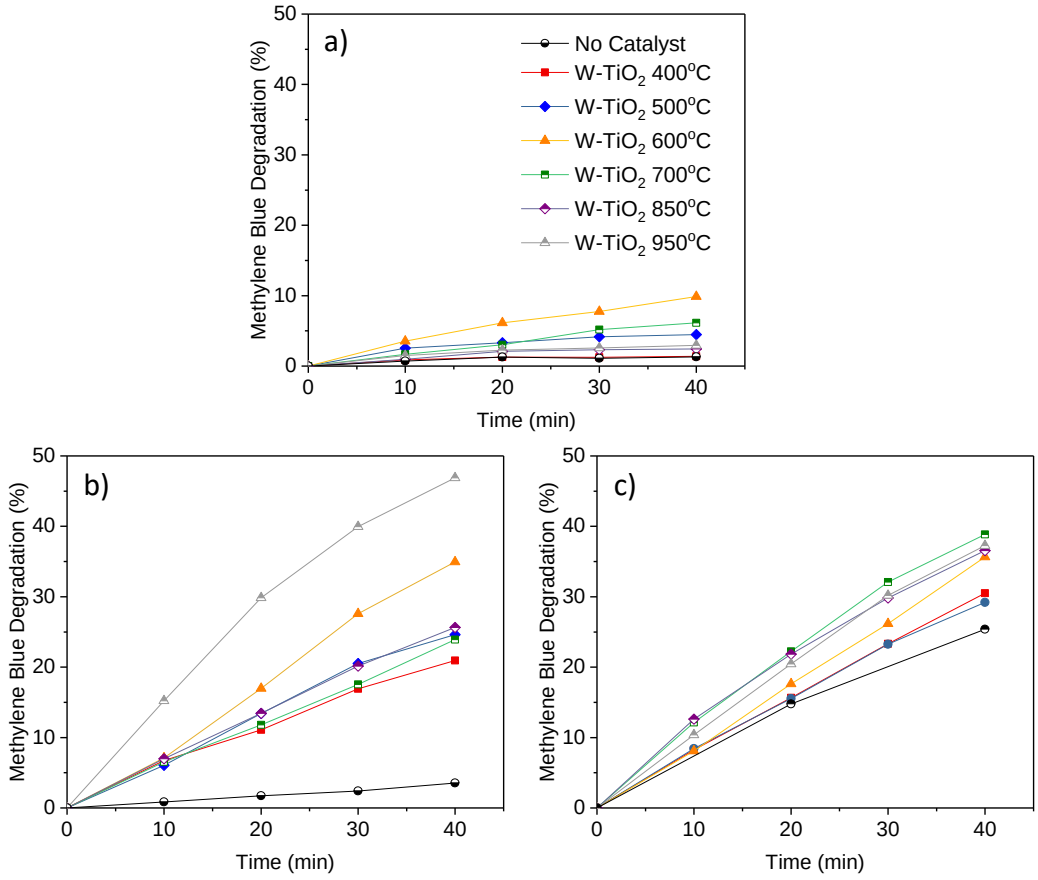

Figure 0.11. Methylene Blue degradation from 0 to 40 minutes of all annealed W-TiO_2 samples compared to no catalyst for (a) dark (b) UV Illumination, and (c) Visible Illumination batch reactions. Data collected with the help of Ashley Pennington

From the Methylene Blue degradation reactions, it is noted that depending on which wavelength is targeted, the W-TiO_2 should be annealed at different temperatures. An annealing temperature of 700 °C is preferred for visible light reactions, and an annealing

temperature of 950 °C is preferred for UV reactions, both for overall conversion as well as the largest initial conversion of MB after 10 min .

4.5 Summary

Tungsten-doped TiO_2 has been successfully prepared by pulsed laser ablation of a tungsten foil immersed in liquid titanium tetra-isopropoxide precursor. The as-synthesized nanopowder shows an amorphous or non-crystalline structure attributable to rapid condensation of vaporized species (tungsten species along with TiO_2 species) from the plasma-reaction zone. Upon post-annealing at 400ºC (~ 0.3 T_M) for two hours in air, transformation of the amorphous-W-doped TiO_2 nanoparticles is initiated, forming novel W-doped anatase-TiO_2 nanoparticles morphologies, such as layered nanotubes and onion-like nanospheres. The phase-transformation from anatase to rutile phase is delayed and crystal growth is inhibited in W-doped TiO_2 relative to that of un-doped TiO_2. According to the Scherrer equation, the average crystallite size of TiO_2 (about 13 nm) is slightly reduced by doping with W (to 10 nm), thus, indicating the doping of tungsten ions to the TiO_2 structure.

Tungsten doping also leads to more hydroxyl groups formed as compared to that of non-doped TiO_2. In addition, tungsten doping reduces the band gap of TiO_2 (to 2.92 eV) and increases absorbance as well.

References

(1) Carp, O.; Huisman, C. L.; Reller, A., Photoinduced reactivity of titanium dioxide. *Progress in solid state chemistry* **2004,** 32, (1), 33-177.

(2) Yang, G.; Jiang, Z.; Shi, H.; Xiao, T.; Yan, Z., Preparation of highly visible-light active N-doped TiO 2 photocatalyst. *Journal of Materials Chemistry* **2010,** 20, (25), 5301-5309.

(3) Chen, X.; Mao, S. S., Titanium dioxide nanomaterials: synthesis, properties, modifications, and applications. *Chem. Rev* **2007,** 107, (7), 2891-2959.

(4) Lee, S.; Cho, I.-S.; Lee, J. H.; Kim, D. H.; Kim, D. W.; Kim, J. Y.; Shin, H.; Lee, J.-K.; Jung, H. S.; Park, N.-G., Two-step sol− gel method-based TiO2 nanoparticles with uniform morphology and size for efficient photo-energy conversion devices. *Chemistry of Materials* **2010,** 22, (6), 1958-1965.

(5) Zaleska, A., Doped-TiO2: a review. *Recent Patents on Engineering* **2008,** 2, (3), 157-164.

(6) Di Paola, A.; Garcıa-López, E.; Marcì, G.; Martín, C.; Palmisano, L.; Rives, V.; Venezia, A. M., Surface characterisation of metal ions loaded TiO 2 photocatalysts: structure–activity relationship. *Applied Catalysis B: Environmental* **2004,** 48, (3), 223-233.

(7) Martyanov, I. N.; Berger, T.; Diwald, O.; Rodrigues, S.; Klabunde, K. J., Enhancement of TiO 2 visible light photoactivity through accumulation of defects during reduction–oxidation treatment. *Journal of Photochemistry and Photobiology A: Chemistry* **2010,** 212, (2), 135-141.

(8) Choi, W.; Termin, A.; Hoffmann, M. R., The role of metal ion dopants in quantum-sized TiO2: correlation between photoreactivity and charge carrier recombination dynamics. *The Journal of Physical Chemistry* **1994,** 98, (51), 13669-13679.

(9) Zhu, J.; Deng, Z.; Chen, F.; Zhang, J.; Chen, H.; Anpo, M.; Huang, J.; Zhang, L., Hydrothermal doping method for preparation of Cr 3+-TiO 2 photocatalysts with concentration gradient distribution of Cr 3+. *Applied Catalysis B: Environmental* **2006,** 62, (3), 329-335.

(10) Park, B.-I.; Jie, H.; Song, B.-G.; Kang, K.-M.; Park, J.-K.; Cho, S.-H., The structural, morphological, and surface properties of tungsten-doped TiO2 nanopowders and their contribution to the photocatalytic activity. *Research on Chemical Intermediates* **2014,** 40, (1), 115-126.

(11) Putta, T.; Lu, M.-C.; Anotai, J., Photocatalytic activity of tungsten-doped TiO 2 with hydrothermal treatment under blue light irradiation. *Journal of environmental management* **2011,** 92, (9), 2272-2276.

(12) Lorret, O.; Francová, D.; Waldner, G.; Stelzer, N., W-doped titania nanoparticles for UV and visible-light photocatalytic reactions. *Applied Catalysis B: Environmental* **2009,** 91, (1), 39-46.

(13) Castro, Y.; Arconada, N.; Durán, A., Synthesis and photocatalytic characterisation of mesoporous TiO 2 films doped with Ca, W and N. *Boletín de la Sociedad Española de Cerámica y Vidrio* **2015,** 54, (1), 11-20.

(14) Mor, G. K.; Varghese, O. K.; Paulose, M.; Shankar, K.; Grimes, C. A., A review on highly ordered, vertically oriented TiO 2 nanotube arrays: fabrication, material properties, and solar energy applications. *Solar Energy Materials and Solar Cells* **2006,** 90, (14), 2011-2075.

(15) Sathasivam, S.; Bhachu, D. S.; Lu, Y.; Chadwick, N.; Althabaiti, S. A.; Alyoubi, A. O.; Basahel, S. N.; Carmalt, C. J.; Parkin, I. P., Tungsten doped TiO2 with enhanced photocatalytic and optoelectrical properties via aerosol assisted chemical vapor deposition. *Scientific reports* **2015,** 5, 10952.

(16) Štengl, V. c.; Velická, J.; Maríková, M.; Grygar, T. s. M., New generation photocatalysts: how tungsten influences the nanostructure and photocatalytic activity of TiO2 in the UV and visible regions. *ACS applied materials & interfaces* **2011,** 3, (10), 4014-4023.

(17) Eibl, S.; Gates, B.; Knözinger, H., Structure of WO x/TiO2 Catalysts Prepared from Hydrous Titanium Oxide Hydroxide: Influence of Preparation Parameters. *Langmuir* **2001,** 17, (1), 107-115.

(18) Ramis, G.; Busca, G.; Cristiani, C.; Lietti, L.; Forzatti, P.; Bregani, F., Characterization of tungsta-titania catalysts. *Langmuir* **1992,** 8, (7), 1744-1749.

(19) Tian, H.; Ma, J.; Li, K.; Li, J., Photocatalytic degradation of methyl orange with W-doped TiO 2 synthesized by a hydrothermal method. *Materials Chemistry and Physics* **2008,** 112, (1), 47-51.

(20) Yang, H.; Zhang, D.; Wang, L., Synthesis and characterization of tungsten oxide-doped titania nanocrystallites. *Materials Letters* **2002,** 57, (3), 674-678.

(21) Zhang, M.; Wu, J.; Lu, D.; Yang, J., Enhanced visible light photocatalytic activity for TiO2 nanotube array films by codoping with tungsten and nitrogen. *International Journal of Photoenergy* **2013,** 2013.

(22) Mozia, S.; Borowiak-Paleń, E.; Przepiórski, J.; Grzmil, B.; Tsumura, T.; Toyoda, M.; Grzechulska-Damszel, J.; Morawski, A. W., Physico-chemical properties and possible photocatalytic applications of titanate nanotubes synthesized via hydrothermal method. *Journal of Physics and Chemistry of Solids* **2010,** 71, (3), 263-272.

(23) Song, F.; Zhao, Y.; Zhong, Q., Adsorption of carbon dioxide on amine-modified TiO2 nanotubes. *Journal of Environmental Sciences* **2013,** 25, (3), 554-560.

(24) Liu, N.; Chen, X.; Zhang, J.; Schwank, J. W., A review on TiO 2-based nanotubes synthesized via hydrothermal method: formation mechanism, structure modification, and photocatalytic applications. *Catalysis Today* **2014,** 225, 34-51.
(25) Rajeshwar, K.; Osugi, M.; Chanmanee, W.; Chenthamarakshan, C.; Zanoni, M. V. B.; Kajitvichyanukul, P.; Krishnan-Ayer, R., Heterogeneous photocatalytic treatment of organic dyes in air and aqueous media. *Journal of photochemistry and photobiology C: photochemistry reviews* **2008,** 9, (4), 171-192.
(26) Salant, A.; Shalom, M.; Hod, I.; Faust, A.; Zaban, A.; Banin, U., Quantum dot sensitized solar cells with improved efficiency prepared using electrophoretic deposition. *Acs Nano* **2010,** 4, (10), 5962-5968.
(27) Roy, P.; Berger, S.; Schmuki, P., TiO2 nanotubes: synthesis and applications. *Angewandte Chemie International Edition* **2011,** 50, (13), 2904-2939.
(28) Paramasivam, I.; Macak, J.; Schmuki, P., Photocatalytic activity of TiO 2 nanotube layers loaded with Ag and Au nanoparticles. *Electrochemistry Communications* **2008,** 10, (1), 71-75.
(29) Benoit, A.; Paramasivam, I.; Nah, Y.-C.; Roy, P.; Schmuki, P., Decoration of TiO 2 nanotube layers with WO 3 nanocrystals for high-electrochromic activity. *Electrochemistry Communications* **2009,** 11, (4), 728-732.
(30) Das, C.; Paramasivam, I.; Liu, N.; Schmuki, P., Photoelectrochemical and photocatalytic activity of tungsten doped TiO 2 nanotube layers in the near visible region. *Electrochimica Acta* **2011,** 56, (28), 10557-10561.
(31) Xu, H.; Liao, J.; Yuan, S.; Zhao, Y.; Zhang, M.; Wang, Z.; Shi, L., Tuning the morphology, stability and photocatalytic activity of TiO 2 nanocrystal colloids by tungsten doping. *Materials Research Bulletin* **2014,** 51, 326-331.
(32) Wu, Y.; Hu, X.; Xie, T.; Li, G.; Zhang, L., Phase structure of W-doped nano-TiO2 produced by sol-gel method. *China Particuology* **2005,** 3, (4), 233-236.
(33) Shannon, R. D., Revised effective ionic radii and systematic studies of interatomic distances in halides and chalcogenides. *Acta crystallographica section A: crystal physics, diffraction, theoretical and general crystallography* **1976,** 32, (5), 751-767.
(34) Xin, B.; Jing, L.; Ren, Z.; Wang, B.; Fu, H., Effects of simultaneously doped and deposited Ag on the photocatalytic activity and surface states of TiO2. *The Journal of Physical Chemistry B* **2005,** 109, (7), 2805-2809.
(35) Gong, J.; Yang, C.; Pu, W.; Zhang, J., Liquid phase deposition of tungsten doped TiO 2 films for visible light photoelectrocatalytic degradation of dodecyl-benzenesulfonate. *Chemical Engineering Journal* **2011,** 167, (1), 190-197.
(36) Li, X.; Li, F.; Yang, C.; Ge, W., Photocatalytic activity of WO x-TiO 2 under visible light irradiation. *Journal of Photochemistry and Photobiology A: Chemistry* **2001,** 141, (2), 209-217.

(37) Leftheriotis, G.; Papaefthimiou, S.; Yianoulis, P.; Siokou, A.; Kefalas, D., Structural and electrochemical properties of opaque sol–gel deposited WO 3 layers. *Applied Surface Science* **2003,** 218, (1), 276-281.
(38) Chen, D.-m.; Xu, G.; Miao, L.; Chen, L.-h.; Nakao, S.; Jin, P., W-doped anatase TiO 2 transparent conductive oxide films: Theory and experiment. *Journal of Applied Physics* **2010,** 107, (6), 063707.
(39) Su, L.; Lu, Z., All solid-state smart window of electrodeposited WO 3 and TiO 2 particulate film with PTREFG gel electrolyte. *Journal of Physics and Chemistry of Solids* **1998,** 59, (8), 1175-1180.
(40) Scholz, A.; Schnyder, B.; Wokaun, A., Influence of calcination treatment on the structure of grafted WO x species on titania. *Journal of Molecular Catalysis A: Chemical* **1999,** 138, (2), 249-261.

Chapter Five

Synthesis of Molybdenum- and Vanadium-Doped TiO_2

Nanostructured powders of molybdenum-doped TiO_2 are synthesized by pulsed-laser ablation of a molybdenum foil immersed in liquid titanium tetra-isopropoxide (TTIP). In this process, interaction between the focused laser beam and the Mo substrate generates a submerged-plasma flame, where vaporization of the Mo substrate along with decomposition of the liquid precursor combine to produce Mo-doped TiO_2 nanoparticles upon quenching by the surrounding un-reacted liquid precursor. A non-crystalline structure (amorphous structure) have been produced as synthesized nanoparticles, primarily because of rapid condensation and quenching of vaporized species from the plasma-reaction zone. Interestingly, upon subsequent heat treatment in air or oxygen, starting at ~400 ºC, transformation to the more stable anatase-TiO_2 phase occurs, but now doped with Mo. Initial results show that Mo-doped anatase TiO_2 exhibits a higher UV and visible photochemical activity than un-doped anatase-TiO_2.

Similarly, vanadium-doped TiO_2 nanostructure is created by using laser ablation of vanadium foil immersed in TTIP solution. The results reveal that the unit cell volume and parameters *a* and *c* of vanadium-doped TiO_2 samples decrease in comparison to those of un-doped samples, indicating that vanadium ions replace titanium ions.

5.1 Introduction

TiO_2 as photocatalyst was first recommended by Fujishima in 1972 [1]. By reason of unique attributes of TiO_2 including low cost, non-toxicity, and stability against chemical corrosion, TiO_2 has been the preferred material for many applications such as solar energy conversion, self-cleaning, gas sensors, and photoluminescence light [2-5]. TiO_2 has a wide band gap (i.e., 3.2 eV), and visible portion (45%) [6]. Given these properties, TiO_2 is mainly active under irradiation with ultraviolet (UV) light. Efforts have been devoted to modify the band gap of TiO_2 in order to shift the absorption edge to the visible range and thus augment its photocatalytic capability under sunlight. One of the effective ways is to dope TiO_2 with metal or non-metal ions (e.g., W, Mo, Cu, Ag, N, C). Co-doping TiO_2 with two or more different elements may be a strategic way to develop visible-light sensitivity [7, 8]. These methods can introduce additional energy levels into the band gap structure of TiO_2. In addition, transition metals can help to improve the activity of TiO_2 photocatalysts by preventing electron-hole recombination, increasing the number of electrons flowing to the other electrode [9]. At present, transition metals have been reported extensively as a favorable dopant in TiO_2.

It has been reported that molybdenum-doping of TiO_2 can result in lower the band gap of the material as thus shift the absorption edge toward the visible region, modifying the photocatalytic properties of TiO_2 [10-12]. Mo^{6+} ions can easily substitute into TiO_2 lattice structure and form an n-type semiconductor because its ionic radius (i.e., 0.62 Å) is similar to that of TiO_2 (0.68 Å) [13]. Molybdenum-doped TiO_2 has been prepared by using

techniques such as sol-gel, hydrothermal, and flame synthesis. Wang et al. [11] prepared Mo-doped TiO_2 using sol-gel technique. They observed that the Mo^{6+} ions incorporated into anatase TiO_2 structure and narrowed the band gap of the TiO_2–based material from 3.19 eV to 3.05 eV. Using the same processing technique, Huang et al. [14] showed that molybdenum decreased the band gap from 3.05 eV of TiO_2 to 2.73 eV of $TiMo_{0.02}O$. Also, they reported that Mo^{6+} replaced Ti^{4+} in the TiO_2 lattice and thus inhibited growth of the crystallite size as well as suppressed the phase transformation from anatase to rutile phase. Doping Mo in TiO_2 increases the lattice distortion of the TiO_2 matrix, where Sheng et al. [12] found increase in the lattice parameters size with increasing Mo doping amount. Others have prepared amorphous Mo-doped TiO_2 thin films using spray pyrolysis. After heat treatment, anatase and mixed anatase/rutile phase were obtained depending on the type of substrate [15]. Khan et al. [16] prepared Mo-doped TiO_2 using hydrothermal method. Depending on their functional theory based calculation study, they found that the molybdenum created impurity states below the conduction band of TiO_2, with the Fermi level pinned inside the conduction band, thus enhancing visible light absorption.

Vanadium, as a transition metals ion, has attracted attention recently. Its ability to (*i*) increase the carrier life time, and (*ii*) extend TiO_2 absorption range [17] make vanadium a favorable ion to dope into TiO_2. The ionic radius of vanadium is quite a bit smaller than that of titanium, meaning that it can be easily incorporated into the TiO_2 lattice. Different methods have been used to prepare V-doped TiO_2 nanostructures. Avansi et al. [18] synthesized V-doped TiO_2 using hydrothermal decomposition of vanadium and titanium peroxo-complexs. They showed that the vanadium ions are distributed homogeneously in

the TiO_2 structure, which mean that the V ions occupy the Ti^{4+} site, leading to improved optical properties of TiO_2. As an important application of detection of key pollutants, vanadium-doped TiO_2 has been used as a sensor. Morris et al. [19] prepared V-doped TiO_2 by high-temperature (1200 $^{\circ}C$) solid-state reaction between V_2O_5 and TiO_2 in a recrystallized aluminum boat. Their results indicated that the 0.5% vanadium doped TiO_2 is a useful material to detect SO_2 at concentrations down to 10 ppm. Songara et al [20] synthesized V-doped TiO_2 by using a wet chemical method. They observed that the unit cell volume of doped materials is smaller than that of un-doped materials. Zhou et al [21] showed that the vanadium is mainly found in the V^{5+} valance. They observed that the vanadium in TiO_2 promotes crystal growth as well as decrease in crystal c-lattice parameter.

In this work, molybdenum-doped TiO_2 as well as vanadium-doped TiO_2 are fabricated using our technique of laser ablation of metal foils immersed in titanium tetra-isopropoxide (TTIP) precursor. Their performance in photocatalytic reactions is considered in this study. Heat treated nanopowders are carefully investigated to study the crystal structure of TiO_2 after doping with the metal ions. The results show that the doped samples are more photocatalytically active than that of un-doped samples, Figure (8).

5.2 Experimental and Setup

Nanostructured powders of Mo-TiO_2 and V-TiO_2 are synthesized by pulsed-laser ablation of a molybdenum/vanadium foil (0.05 mm thick, 99.95% purity), respectively, immersed in liquid titanium tetra-isopropoxide (TTIP, 99.5% purity). In this process, Figure 0.1, the

Mo/V-foil is a rotating target (50 rpm), and an Nd:YAG pulsed laser beam (wave length 532 nm, maximum pulse energy 500 mJ/pulse) ablates the molybdenum/vanadium target, while simultaneously decomposing and vaporizing the liquid precursor. In practice, the laser beam is focused onto the Mo/V-target surface with 100 mJ/pulse, 10 Hz repetition rate, and 5 ns pulse width.

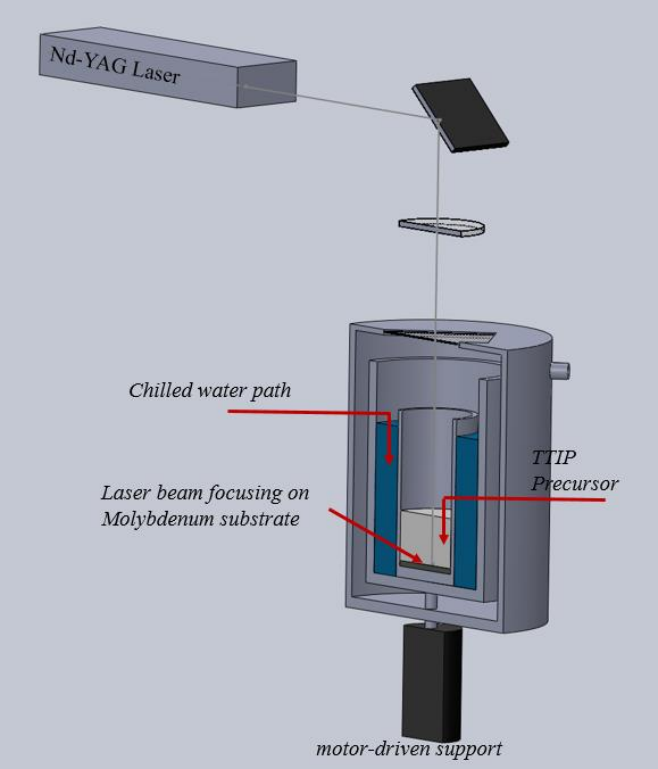

Figure 0.1. Schematic diagram of the experimental setup: (1) Nd-YAG laser; (2) reflecting mirror; (3) laser beam; (4) focusing lens; (5) cover plate (glass slide); (6) liquid TTIP precursor; (7) chilled water bath; (8) N2 gas inlet;(9) N2 gas outlet; and (10) motor-driven support.

5.3 Results and Discussion

5.3.1 Molybdenum-doped TiO_2

The XRD patterns of pure TiO_2 and Mo-doped TiO_2 heat treated at different temperatures are given in Figure 0.2. The samples are heat treated from 400ºC to 1050ºC in air for 2 hours. The as-synthesized Mo-doped nanopowders are observed to be in an amorphous phase. The nanopowders crystallize and become anatase at 400ºC. The diffraction peaks of all samples display that there are no MoO peaks, as shown in Figure 0.2 (a), with all peaks attributable to anatase and rutile phases. This result implies that the molybdenum is incorporated into the TiO_2 lattice structure. As the ionic radius of molybdenum (i.e., 0.62 nm) and titanium (i.e., 0.68 nm) are quite similar, the Mo^{6+} ions can substitute Ti^{4+} ions. It is notable that the phase transformation from anatase to rutile of Mo-doped TiO_2 samples are delayed at a certain temperature, Table 0-1, which means that the molybdenum helps to stabilize the anatase phase. Such retarded phase transformation has been observed by other groups [22].

Table 0-1. Phase formed after heat treatment (A: Anatase and R: Rutile).

Sample	400˚C	600˚C	700˚C	850˚C	950˚C	1050˚C
TiO_2	A	A	A	R	R	R
Mo-TiO_2	A	A	A	A + R	A+R	R

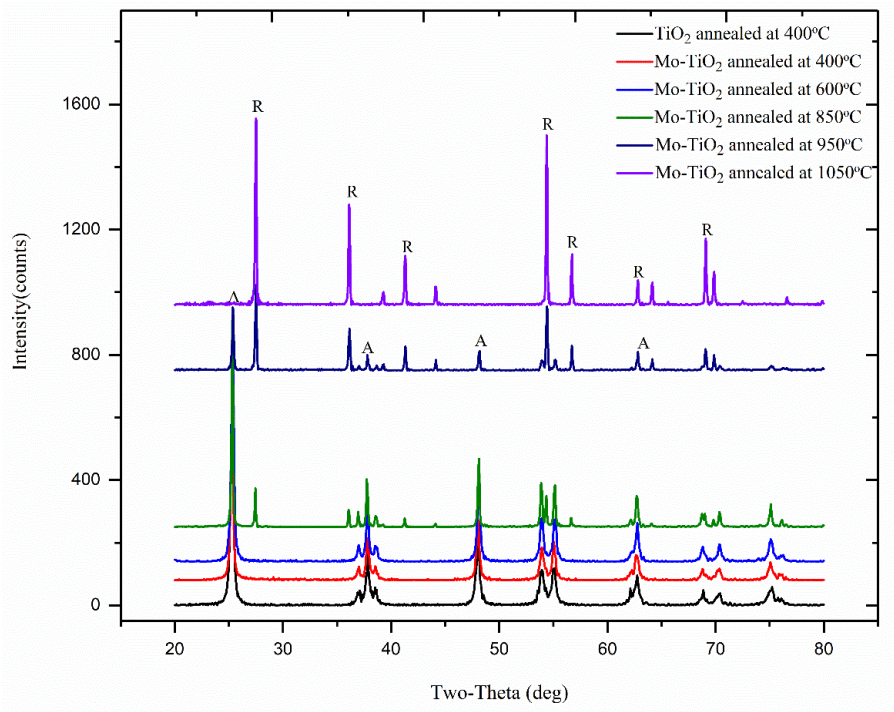

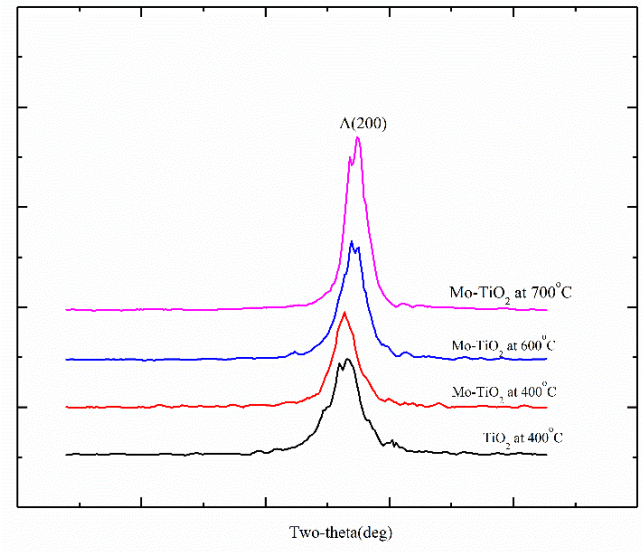

Figure 0.2. **(up)** XRD patterns of Mo-doped TiO_2 annealed at different temperatures (A: Anatase, R: Rutile). **(down)** Slight shift in anatase peak (200) comparing to un-doped TiO_2 sample.

The XPS analyses are carried out to determine the oxidation states of Ti, O, and Mo of the un-doped and Mo-doped TiO_2, which annealed at 400ºC in air for two hours respectively. The oxidation states of Ti are shown in Figure 0.3. The binding energies (BE) of 458.3 eV and 464.02 eV correspond to the Ti *2p3/2* and Ti *2p1/2* states of un-doped TiO_2, Figure 0.3(a), respectively, which are consistent with the values of Ti^{4+} in TiO_2 lattice [23]. As Mo ions have larger electron negativity than that of Ti, the substitution of Mo for Ti in the lattice leads to a right shift in the binding energies of Ti *2p3/2* (458.7 eV) and Ti *2p1/2* (464.39 eV) states, respectively, of the Mo-doped TiO_2 samples, Figure 0.3 (b). This result indicates that the molybdenum atoms substituted titanium atoms. Other researchers have similarly reported shifts in the binding energy of Ti [11, 14, 24].

XPS spectra of O *1s* are shown in Figure 0.4. Interestingly, the state of the O element in Mo-doped TiO_2 samples is different from that of un-doped TiO_2. The un-doped sample shows two peaks located at binding energies of 530.09 eV and 531.81 eV which are related to crystal lattice oxygen and adsorbed oxygen, respectively, Figure 0.4 (a). The Mo-doped TiO_2 sample gives three peaks located at binding energies of 530.34 eV, 531.77 eV, and 532.83 eV, Figure 0.4 (b). The binding energy at 532.83 is attributed to adsorbed water and hydroxyl groups [11]. Comparison between Figure 0.4 (a) and Figure 0.4 (b) reveals that there is much more "absorption O" on the surface of Mo-doped TiO_2 than there is on un-doped TiO_2. After doping of Mo into TiO_2, the TiO_2 lattice is in the oxygen deficiency state (as one titanium atom needs two O atoms, while one molybdenum atom needs three O atoms. The surface deficiency of O can be complemented by absorbing more O atoms,

so more absorbed O can be detected on the surface of Mo-doped TiO_2 in comparison with that of un-doped TiO_2.

The range of binding energies of Mo *3d* electron in the spectrum show the presence of a doublet peak structure at 232.31 eV and 235.51 eV, Figure 0.5, characteristic for Mo^{6+} ion [25]. The separation between the two peaks is 3.2 eV, in agreement with the values reported in the literature [26, 27]

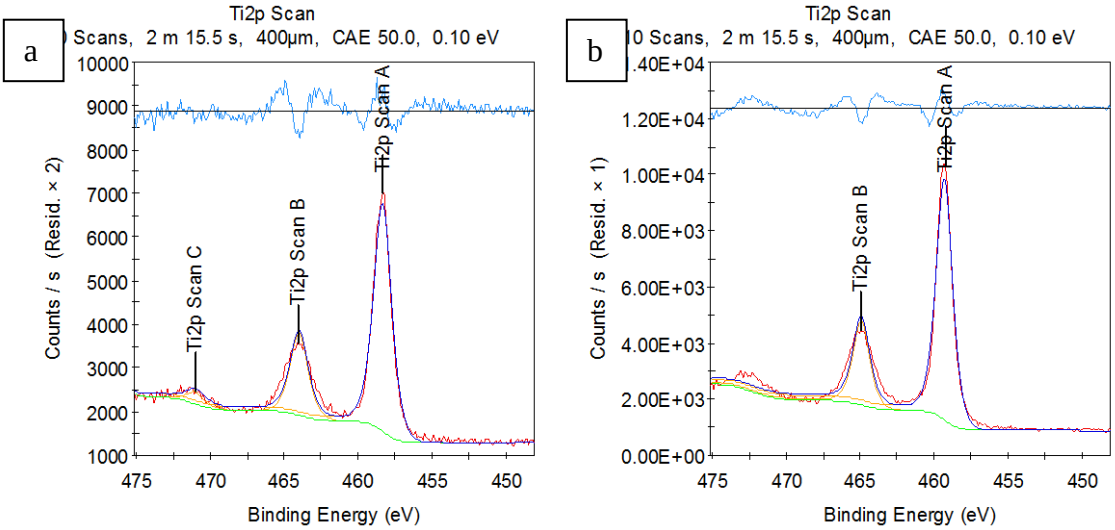

Figure 0.3. XPS spectra of Ti 2*p* binding level energy of (a) un-doped sample and (b) molybdenum-doped TiO_2 sample, both are annealing at 400 °C for 2 hours.

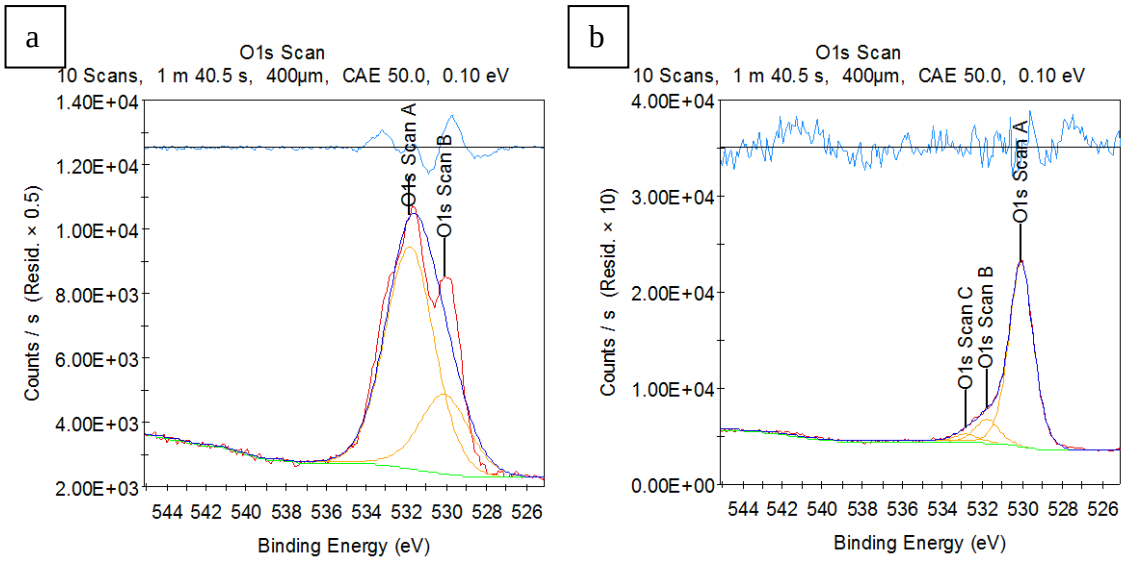

Figure 0.4. XPS spectra of O 1*s* binding level energy of (a) un-doped sample and (b) Molybdenum-doped TiO_2 sample, both are annealing at 400 ˚C for 2 hours.

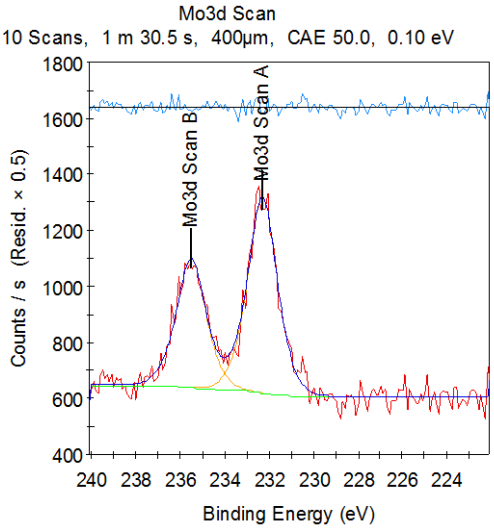

Figure 0.5. XPS spectra of Mo 2*p* binding level energy of molybdenum-doped TiO_2 sample, annealing at 400˚C for 2 hours.

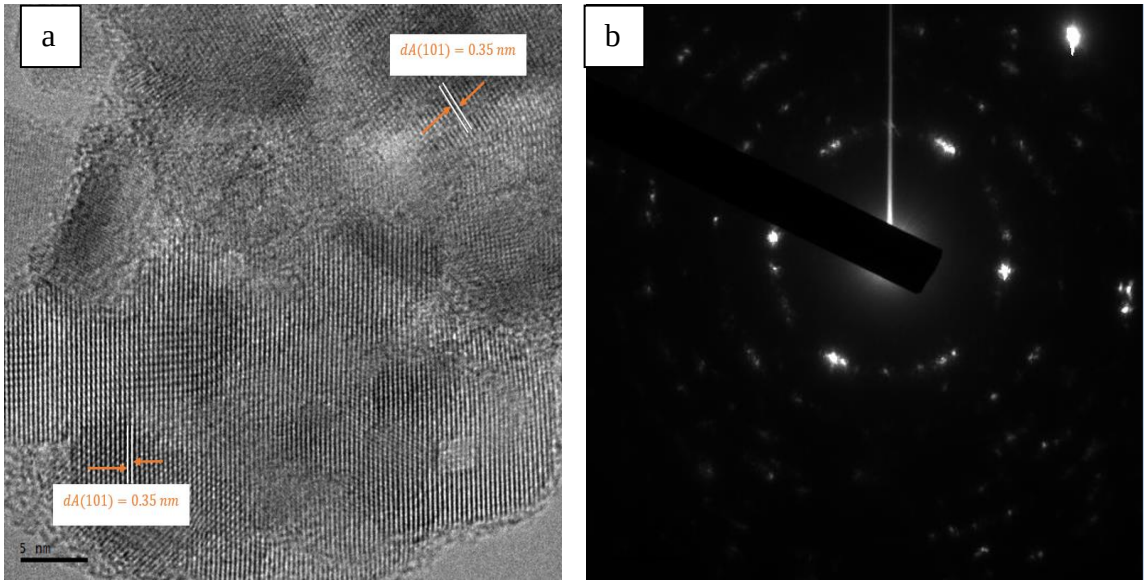

Figure 0.6. (a) Lattice image of a well-crystallized nanoparticle, showing d-spacing of 0.35 nm, in agreement with XRD, and (b) spotty-ring pattern indicative of a random nanocrystalline structure.

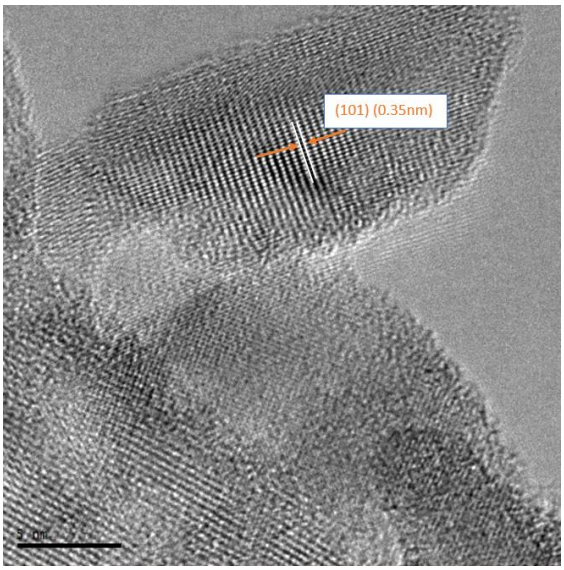

Figure 0.7. Mo-doped TiO_2 nanoparticles, after annealing at 400ºC/2 hrs in air, showing radially-symmetric nanocrystalline structure.

As-synthesized amorphous Mo-doped TiO_2 nanoparticles, post-annealed at 400ºC for 2 hrs in air, transform into nanocrystalline anatase-TiO_2. As discussed in a previous chapter, this phase transformation occurs layer-by-layer in its crystalline-growth mechanism, starting at the nanoparticle surface and propagating uniformly into the interior. The resulting image shows a radially-symmetric crystalline structure. Lattice imaging of a well-crystallized nanoparticle, with corresponding SAED pattern is displayed in Figure 0.6. The measured *d* spacing is 0.35 nm, which corresponds to (101) in anatase-TiO_2. A STEM image of partially crystallized anatase-TiO_2 nanoparticles is presented in Figure 0.7.

5.3.2 Optical Properties of Mo- doped TiO_2 nanopowder.

The optical property of molybdenum-doped TiO_2 is analyzed after different annealing tempertures using a UV-Visible Sprctrophotometer. The absolute diffuse reflectance of the sample is collected and converted to Kubelka Munk, the analog to absorbance for diffusely reflected samples, Figure 0.8. The band gap energy (BGE) of the samples are determined both by the traditional Tauc method, where $Tauc^{1/2}$ determines the indirect band gap energy, as well as via the more accurate derivative peak fitting (DPR) method, which determines the direct BGE much more precicely than $Tauc^2$. Doping of molybdenum ions decreases the indirect BGE of laser synthesized anatase from 3.04 eV to 2.80 eV, when annealed at 400°C, Table 0-2. Increasing the annealing temperature of the molybdenum-doped samples diminishes the effect of decreasing the indirect BGE. While using DPR to measure the direct BGE, it is noted that the annealing temperature of the samples doped with molybdenium plays a role in the resultant direct BGE. Mo-TiO_2

annealed to 400 °C has a larger direct BGE, likely because of its low crystallinity, whereas Mo-TiO_2 annealed to 500 °C causes the direct BGE to shrink to 3.09 eV. Increasing the anealing temperature even higher (600-700 °C), the direct BGE remains relativly unchanged from the annealed laser synthesized sample (3.19 eV), indicating that the molybdenum helps to shrink the indirect BGE thereby increasing its absorbance of visible light.

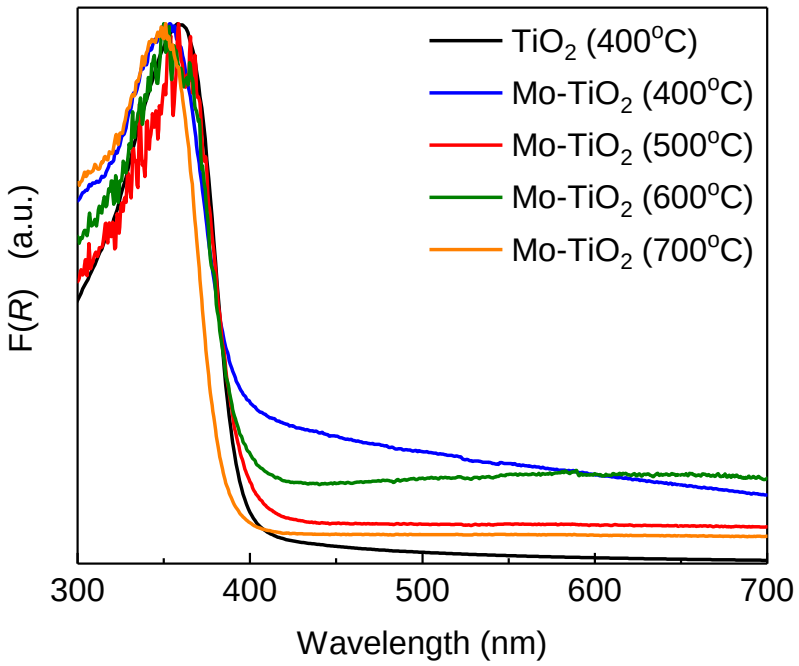

Figure 0.8. Kubelka Munk, F(*R*), of laser synthesized un-doped TiO_2 annealed to 400°C (black) and Mo-doped TiO_2 annealed to 400°C (blue), 500°C (red), 600°C (green), and 700°C (orange). *Data collected with the help of Ashley Pennington*

Table 0-2. The band gap energies of TiO_2 and Mo-doped TiO_2 samples annealed in an oven under stagnant conditions at different temperatures.		
Samples	Tauc$^{1/2}$ Band gap (eV)	DPR Band gap (eV)
TiO_2 as prepared	3.19 eV	3.35 eV
TiO_2 (400°C)	3.04 eV	3.19 eV
Mo-doped TiO_2 (400°C)	2.80 eV	3.24 eV
Mo-doped TiO_2 (500°C)	2.87 eV	3.09 eV
Mo-doped TiO_2 (600°C)	2.89 eV	3.16 eV
Mo-doped TiO_2 (700°C)	3.00 eV	3.23 eV, 3.08 eV

5.4 Vanadium doped TiO_2

As synthesized V-doped TiO_2 nanopowder exhibits an amorphous-like structure similar to that of as-synthesized Mo-doped TiO_2. In the previous chapter (four) of tungsten-doped TiO_2, the as-synthesized nanopowder exhibits amorphous structure as well. XRD patterns of V-TiO_2, after heat treatments at 400-950ºC are shown in Figure 0.9. The peak at 25.2° corresponds to anatase phase (101), and the peak at 27.3° relates to rutile phase (110). An amorphous-to-anatase phase change occurs at 400ºC; and an anatase-to-rutile phase change occurs at 950 ºC, with no indication for any other phases. The evidence supports the widely accepted view that V^{5+} ions substitute for Ti^{4+} in both anatase- and rutile-TiO_2 phases [18, 28]. Moreover, a peak shift to higher two-theta, Figure 0.10, indicates that the unit cell volume of V-doped TiO_2 decreases compared with that of un-doped TiO_2. Since the ionic radius of V^{5+} (i.e., 0.054 nm) is smaller than that of Ti^{4+} (i.e., 0.060 nm) [21, 29], vanadium ions can readily replace titanium ions in the TiO_2 lattice.

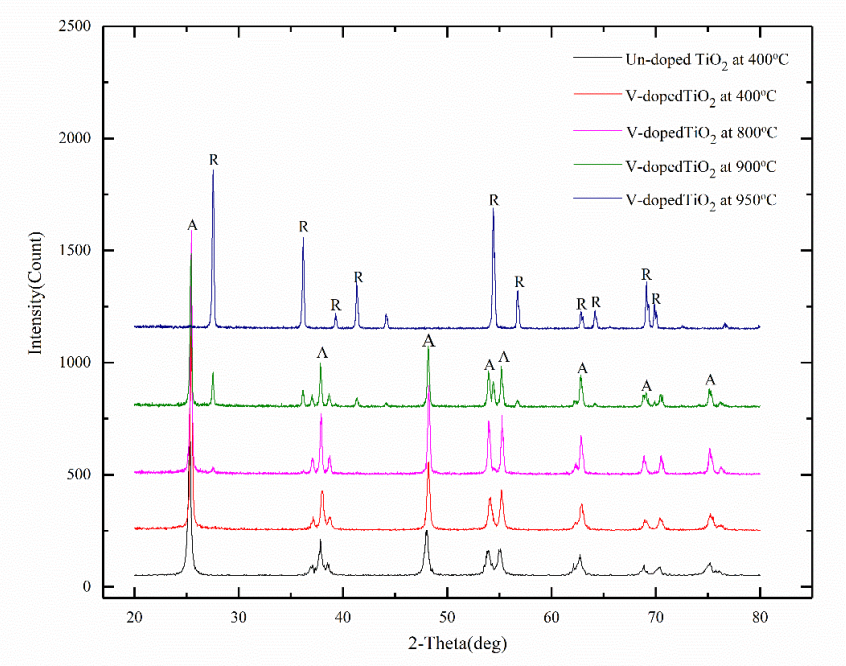

Figure 0.9. A series of XRD spectra for as-synthesized TiO_2 nanoparticles, and Vanadium-doped TiO_2 after post annealing at 400 -950 ºC for 2 hr in air. (A-anatase, R-rutile).

Songara et al. [20] found a decrease in the lattice constant values of TiO_2 after doping with vanadium. Nguyen et al. [17] reported that the anatase peak (101) position shifted to the higher two-theta in the V-doped TiO_2 samples. Table 0-3 shows the differences in the unit cell volume at different annealing temperatures. As the annealing temperature is raised to 800°C, V_{cell} increases, approaching that of un-doped TiO_2. It is believed that the vanadium ions are incorporated into the anatase crystal to result in the decrease of the c-axis lattice parameter and the formation of a V–Ti oxide solid state solution. This agrees with previously reported studies on vanadium-doped TiO_2, where a constant a-axis and a decrease in c-axis lattice parameters were obtained with increased V doping [20] [30].

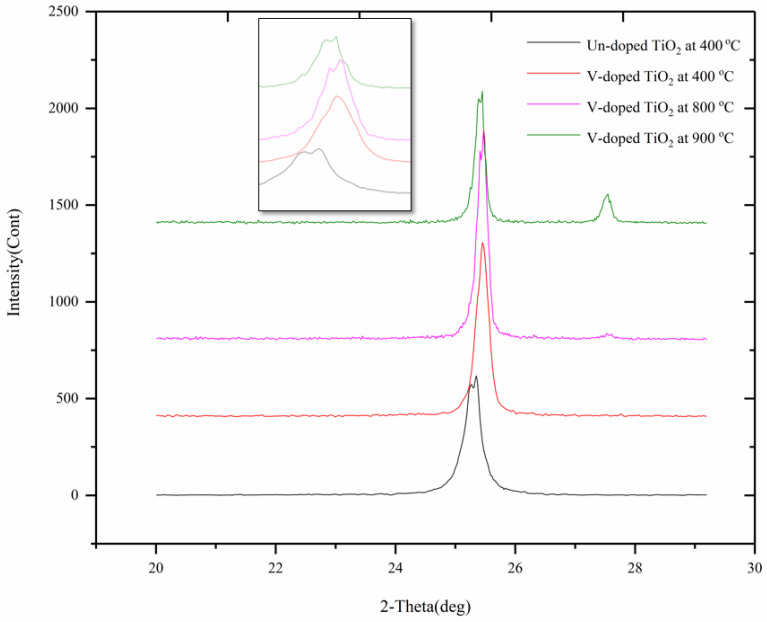

Figure 0.10. Peak shift of Vanadium-doped TiO_2 at varying annealing temperatures. The peak shifting to higher 2-theta indicate the incorporation of vanadium to the TiO_2 lattice structure.

Table 0-3. Decrease in the unit cell volume of V-doped TiO_2 as compared to un-doped TiO_2.

Parameters	Un-doped TiO_2 400°C	V-doped TiO_2 400°C	V-doped TiO_2 800°C	V-doped TiO_2 950°C
a (A)	3.783	3.777	3.772	3.769
c (A)	9.447	9.325	9.425	9.321
V_{cell} (A)	1.352	1.331	1.341	1.326

5.5 Summary

In this chapter, molybdenum and vanadium ions are successfully doped into the TiO_2 structure by using the novel process of laser ablation in liquid precursor. Titanium tetra-

isopropoxide (TTIP) is used as a precursor, and a laser beam is focused on a Mo/V foil immersed within the liquid precursor. The XRD results show there are no MoO peaks, indicating that the molybdenum ions are incorporated into the TiO_2 structure. The phase transformation from anatase to rutile phase is retarded in the doped TiO_2 samples, suggesting that molybdenum may stabilize the anatase phase. In addition, the band gap energy of the doped TiO_2 samples is reduced to lower binding energies, helping to increase absorbance of visible light.

Vanadium-doped TiO_2 nanopowders show decreases in the unit cell volume of TiO_2 in comparison to that of un-doped TiO_2, reaching the maximum reduction at 950^{o}C. Peak shifting to higher two-theta is observed in the V-doped TiO_2 sample.

References

(1) Fujishima, A.; Hashimoto, K.; Watanabe, T., *TiO2 photocatalysis: fundamentals and applications*. ed.; BKC Incorporated: 1999.
(2) Hadjiivanov, K. I.; Klissurski, D. G., Surface chemistry of titania (anatase) and titania-supported catalysts. *Chemical Society Reviews* **1996,** 25, (1), 61-69.
(3) Liu, N.; Chen, X.; Zhang, J.; Schwank, J. W., A review on TiO 2-based nanotubes synthesized via hydrothermal method: formation mechanism, structure modification, and photocatalytic applications. *Catalysis Today* **2014,** 225, 34-51.
(4) Diamandescu, L.; Vasiliu, F.; Tarabasanu-Mihaila, D.; Feder, M.; Vlaicu, A.; Teodorescu, C.; Macovei, D.; Enculescu, I.; Parvulescu, V.; Vasile, E., Structural and photocatalytic properties of iron-and europium-doped TiO 2 nanoparticles obtained under hydrothermal conditions. *Materials Chemistry and Physics* **2008,** 112, (1), 146-153.
(5) Benoit, A.; Paramasivam, I.; Nah, Y.-C.; Roy, P.; Schmuki, P., Decoration of TiO 2 nanotube layers with WO 3 nanocrystals for high-electrochromic activity. *Electrochemistry Communications* **2009,** 11, (4), 728-732.
(6) Cao, L.; Wang, D.; Xu, L.; Li, X., First-principles study on the synergistic effects of Mo–C codoped anatase TiO 2. *Solid State Communications* **2014,** 185, 5-9.
(7) Chen, X.; Mao, S. S., Titanium dioxide nanomaterials: synthesis, properties, modifications, and applications. *Chem. Rev* **2007,** 107, (7), 2891-2959.
(8) Lee, S.; Cho, I.-S.; Lee, J. H.; Kim, D. H.; Kim, D. W.; Kim, J. Y.; Shin, H.; Lee, J.-K.; Jung, H. S.; Park, N.-G., Two-step sol− gel method-based TiO2 nanoparticles with uniform morphology and size for efficient photo-energy conversion devices. *Chemistry of Materials* **2010,** 22, (6), 1958-1965.
(9) Zaleska, A., Doped-TiO2: a review. *Recent Patents on Engineering* **2008,** 2, (3), 157-164.
(10) Devi, L. G.; Murthy, B. N., Characterization of Mo doped TiO2 and its enhanced photo catalytic activity under visible light. *Catalysis letters* **2008,** 125, (3-4), 320-330.
(11) Wang, S.; Bai, L.; Sun, H.; Jiang, Q.; Lian, J., Structure and photocatalytic property of Mo-doped TiO 2 nanoparticles. *Powder technology* **2013,** 244, 9-15.
(12) Luo, S.-Y.; Yan, B.-X.; Shen, J., Enhancement of photoelectric and photocatalytic activities: Mo doped TiO 2 thin films deposited by sputtering. *Thin Solid Films* **2012,** 522, 361-365.
(13) Khan, M.; Xu, J.; Chen, N.; Cao, W., First principle calculations of the electronic and optical properties of pure and (Mo, N) co-doped anatase TiO 2. *Journal of Alloys and Compounds* **2012,** 513, 539-545.
(14) Huang, J.-g.; Guo, X.-t.; Wang, B.; Li, L.-y.; Zhao, M.-x.; Dong, L.-l.; Liu, X.-j.; Huang, Y.-t., Synthesis and photocatalytic activity of Mo-doped TiO2 nanoparticles. *Journal of Spectroscopy* **2015,** 2015.
(15) Mardare, D.; Cornei, N.; Luca, D.; Dobromir, M.; Irimiciuc, Ş. A.; Pungă, L.; Pui, A.; Adomniţei, C., Synthesis and hydrophilic properties of Mo doped TiO2 thin films. *Journal of applied physics* **2014,** 115, (21), 213501.

(16) Khan, M.; Xu, J.; Cao, W.; Liu, Z.-K., Mo-doped TiO2 with enhanced visible light photocatalytic activity: a combined experimental and theoretical study. *Journal of nanoscience and nanotechnology* **2014,** 14, (9), 6865-6871.
(17) Thuy, N. M.; Van, D. Q.; Hai, L. T. H., The visible light activity of the TiO2 and TiO2: V4+ photocatalyst. *Nanomaterials and Nanotechnology* **2012,** 2, 14.
(18) Avansi, W.; Arenal, R.; de Mendonca, V.; Ribeiro, C.; Longo, E., Vanadium-doped TiO 2 anatase nanostructures: the role of V in solid solution formation and its effect on the optical properties. *CrystEngComm* **2014,** 16, (23), 5021-5027.
(19) Morris, D.; Egdell, R., Application of V-doped TiO2 as a sensor for detection of SO2. *Journal of Materials Chemistry* **2001,** 11, (12), 3207-3210.
(20) Songara, S.; Patra, M.; Manoth, M.; Saini, L.; Gupta, V.; Gowd, G.; Vadera, S.; Kumar, N., Synthesis and studies on photochromic properties of vanadium doped TiO 2 nanoparticles. *Journal of Photochemistry and Photobiology A: Chemistry* **2010,** 209, (1), 68-73.
(21) Zhou, M.; Huang, F.; Wang, X.; du Plessis, J.; Murphy, A. B.; Caruso, R. A., Porous vanadium/titanium oxides—synthesis, characterization, and photocatalytic activity. *Australian journal of chemistry* **2007,** 60, (7), 533-540.
(22) Amores, J. M. G.; Escribano, V. S., Anatase crystal growth and phase transformation to rutile in high-area TiO 2, MoO 3–TiO 2 and other TiO 2-supported oxide catalytic systems. *Journal of Materials Chemistry* **1995,** 5, (8), 1245-1249.
(23) Wang, C.-y.; Böttcher, C.; Bahnemann, D. W.; Dohrmann, J. K., A comparative study of nanometer sized Fe (III)-doped TiO 2 photocatalysts: synthesis, characterization and activity. *Journal of Materials Chemistry* **2003,** 13, (9), 2322-2329.
(24) Zhang, T.; Yu, B.; Wang, D.; Zhou, F., Molybdenum-doped and anatase/rutile mixed-phase TiO 2 nanotube photoelectrode for high photoelectrochemical performance. *Journal of Power Sources* **2015,** 281, 411-416.
(25) Shimoda, M., et al., Deconvolution of Mo 3d X-ray photoemission spectraγ-Mo 4 O 11: Agreement with prediction from bond length-bond strength relationships. Journal of materials science letters, 1989. 8(9): p. 1089-1091.
(26) Firment, L. and A. Ferretti, Stoichiometric and oxygen deficient MoO3 (010) surfaces. Surface Science, 1983. 129(1): p. 155-176.
(27) Fleisch, T. and G. Mains, An XPS study of the UV reduction and photochromism of MoO3 and WO3. The Journal of Chemical Physics, 1982. 76(2): p. 780-786.
(28) Le Roy, D.; Valloppilly, S.; Skomski, R.; Liou, S.-H.; Sellmyer, D. J., Magnetism and structure of anatase (Ti1− xVx) O2 films. *Journal of Applied Physics* **2012,** 111, (7), 07C118.
(29) Ichinose, H.; Taira, M.; Furuta, S.; Katsuki, H., Anatase sol prepared from peroxotitanium complex aqueous solution containing niobium or vanadium. *Journal of the American Ceramic Society* **2003,** 86, (9), 1605-1608.
(30) Bucharsky, E.; Schell, G.; Oberacker, R.; Hoffmann, M., Anatase–rutile transformation in TiO 2–V 2 O 5 catalyst coatings for ceramic foams. *Journal of the European Ceramic Society* **2009,** 29, (10), 1955-1961.

Chapter Six

Synthesis of Boron Nitride

Owing to the unique conditions of high temperature, high pressure, and high species density in the plasma-reaction zone, laser ablation in precursor liquid has been developed to synthesize amorphous or metastable phases, which may be difficult to produce using other methods. In this work, pulsed laser ablation of boron bulk immersed in ammonia solution in methanol has been employed to synthesize boron nitride nanoparticles. Interaction between the focused laser beam and the boron bulk generates a submerged-plasma, where ablation of the boron bulk along with decomposition of the adjacent liquid reactant combine to produce BN nanoparticles upon quenching by the surrounding un-reacted liquid precursor. XRD analysis identifies the formed phase. As-synthesized nanoparticles are a mixture of different phases, including hexagonal BN (h-BN), ammonia borane (NH_3BH_3), and different chemi/physisorbed species. Subsequently, a small sample of the as-synthesized powder is heat treated at 1000 ºC for 2 hr to create a more thermally-stable nanocrystalline structure and to remove the surface chemi/physisorbed species. The heat treatment is conducted in an ammonia atmosphere. The heat-treated nanopowder shows a broad peak, indicating poor crystallinity of the nanopowders. TEM results for the heat-treated nanopowders reveals the existence of h-BN nanoparticles (in nanorod morphology) and cubic BN (c-BN).

6.1 Introduction

With their outstanding properties, boron nitride (BN) nano-structures have great potential for various applications, including high performance electronic devices, insulating nanotubular shields, hydrogen storage media, gas absorbents, and reinforcing agents.[1]

Boron nitride occurs in different phases. The stable phase has a graphite-like hexagonal structure (h-BN); and films of this type are relatively soft. Two other phases have diamond-like structure, i.e., zincblende (c-BN) and wurtzite (w-BN) [2]. The two phases are highly-desirable ceramics, offering superior stiffness over many other ceramics and hardness second only to diamond. These phases are superior to diamond in terms of chemical resistance to ferrous alloy. The bonding is a mainly covalent type (sp^3) between the boron and nitrogen atoms [1].

According to Figure 0.1, the hexagonal rings have a uniform bond angle of 120° between each of the atoms. The sp^3 hybridization occurs when puckering compresses the atoms and reduces the overall bond angle resulting in armchair growth from the sp^2 to sp^3. This growth results from the planar spacing along the direction of the h-BN particles being compressed to the point that the induced strain converts the sheets into a cubic structure with the resulting bond angle of 109.5° for the out of plane bond angles. However, these diamond-like phases are metastable and difficult to synthesize. Many attempts have been made in recent years to prepare diamond-like BN films by ion beam techniques[2-4], and by R.F. sputtering [5].

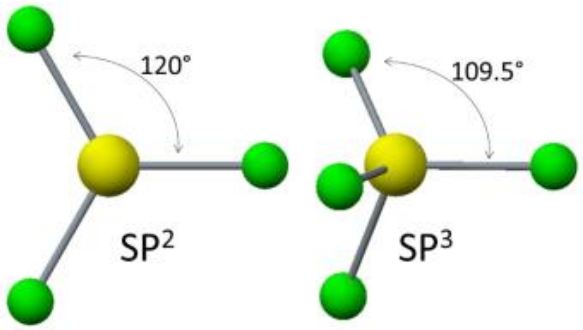

Figure 0.1. Comparison of hBN's sp2 and cBN's sp3 bond geometry [6].

Physical vapor deposition (PVD) and chemical vapor deposition (CVD) techniques have been utilized to synthesize BN [2, 7]. PVD and CVD can deposit nanocrystalline c-BN films, up to about 5 μm in thickness, on a substrate [8]. Samantary et al. [9] and Ichiki et al. [10] claimed that a very thin film of h-BN forms first, which then serves as the substrate for subsequent growth of c-BN. The presence of an initial h-BN growth plane seems to be a consistent feature such synthesis routes, but variations come in the type of BN that grows subsequently upon that initial layer. Plasma-enhanced CVD can employ a focused laser beam to grow c-BN films [11].

In this research, pulsed-laser ablation of boron in ammonia liquid is investigated to synthesize BN nanoparticles. XRD results shows that the initial products are a mixture of different phases including hexagonal BN (h-BN), ammonia borane (NH_3BH_3), and different chemi/physisorbed species. After heat treatment to 1000 °C in an ammonia atmosphere for 2 hrs, a thermally-stable phase of BN is produced.

6.2 Results and Discussion

XRD (Figure 0.2) is used to characterize the phase formation of the as-synthesized and heat-treated nanopowders. As-synthesized nanopowders comprise multiple phases, including hexagonal BN (h-BN), ammonia borane (NH_3BH_3), and different chemi/physisorbed species. These different phases and species result from the high quenching rate of vaporized species from the interaction of the plasma-reaction zone with the surrounding chilled liquid precursor. Heat treating the as-synthesized nanopowders in an ammonia (NH_3) atmosphere at 1000 ℃ for 2 hrs yields the formation of more thermally-stable BN nanoparticles. The diffraction pattern reveals three very-wide, but well-distinguished, peaks at diffraction angles of 26 °, 43 °, and 78 °. The broadening might be due to the presence of an amorphous structure (as in glasses) or to the presence of stress or to small crystal grains. According to TEM analysis, the particles are about 17.4 nm in size. Thus, the main contribution to the observed line broadening is likely caused by the small size of the crystal grains. According to Figure 6.2 and based on the XRD data sheet, the h-BN pattern is characterized by the large peak around 26 °, while the diffraction pattern of c-BN is characterized by the peak around 43 °. The peak observed at 78 ° might be due to h-BN as well as to c-BN. This observation has been observed by Gissler et al. [2]

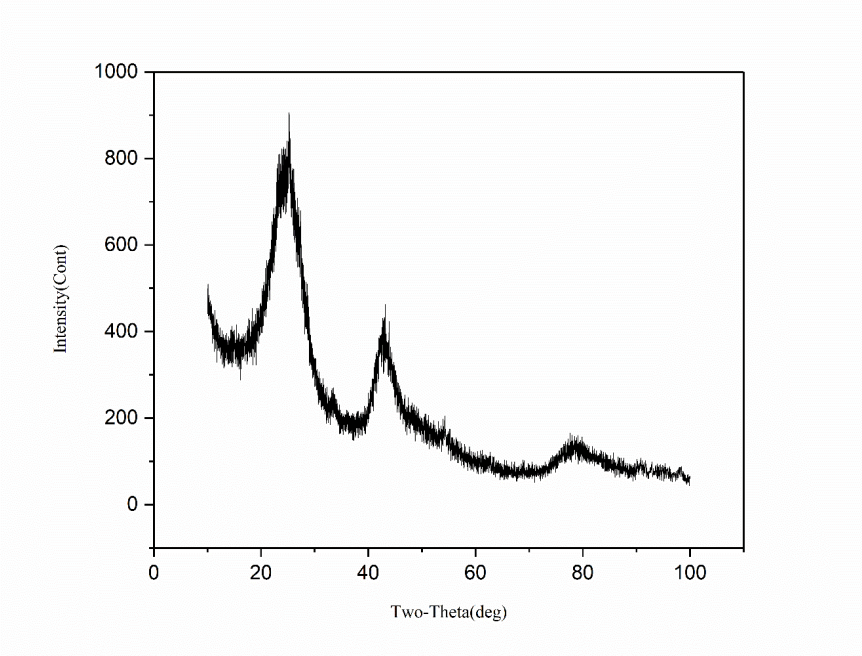

Figure 0.2. XRD profile of BN nanoparticles heat-treated in ammonia (NH3) atmosphere to 1000 °C for 2hrs

Imaging of the powder by TEM is conducted to better understand the specifics of the nanostructure. Figure 0.3(a) shows a nanorod morphology of h-BN with outer diameter of (11.4) nm and inner diameter of (3.4 nm). The SAED pattern of this region is shown as well, where the reflections match those of the planes associated with h-BN (PDF#97-061-4869). The continuous nature of the rings is indicative of the polycrystalline nature of the sample, as can be seen in Figure 0.3(b) a higher magnification. The *d*-spacing of 0.346 nm is correlated with the ring (103) of h-BN, consistent with the XRD results.

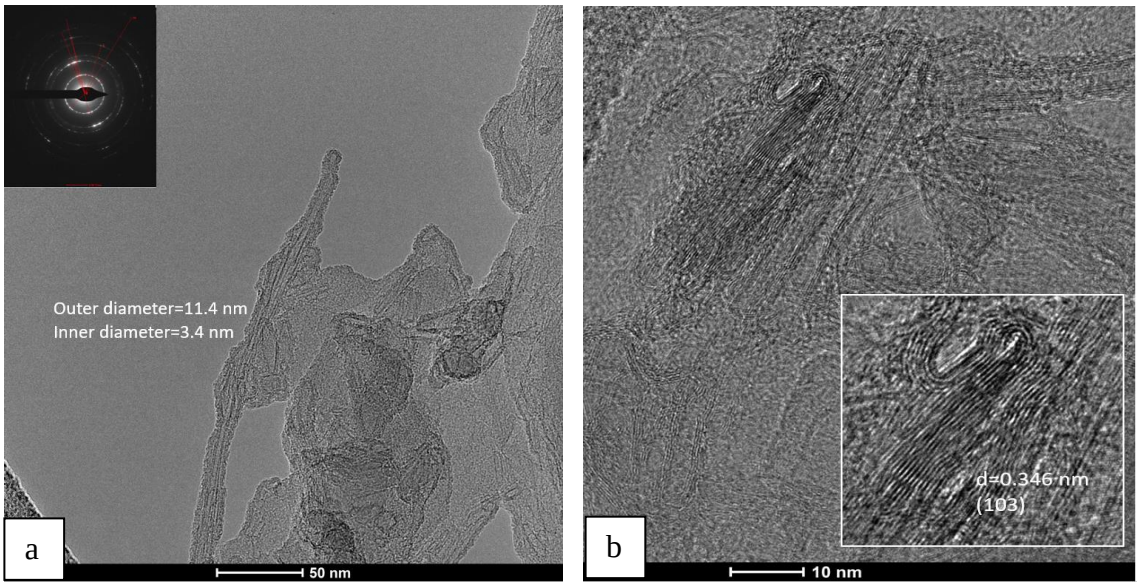

Figure 0.3. TEM image shows (a) h-BN nanorods with outer diameter of 11.4 nm and inner diameter of 3.4 nm (b) higher magnification. TEM images collected with the help of Zhizhong Dong.

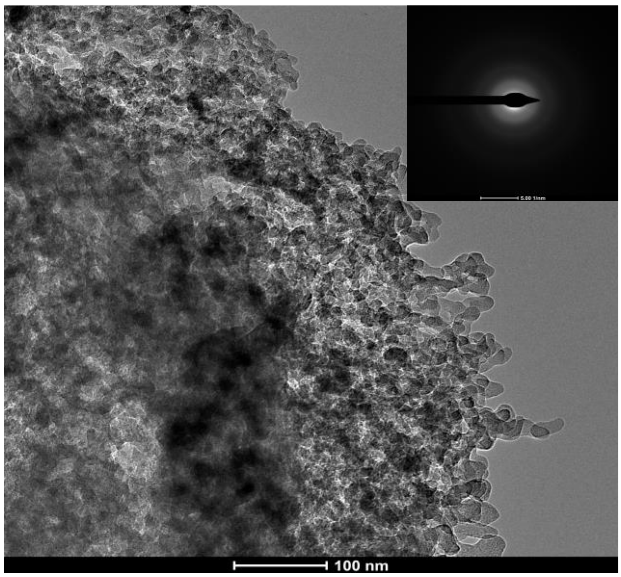

Figure 0.4. TEM image of c-BN nanoparticles with average particle size of 17.4 nm. TEM images collected with the help of Zhizhong Dong

As previously mentioned, c-BN is characterized by the peak around 43 ° in the diffraction pattern (Figure 0.2). The TEM image (Figure 0.4) shows c-BN nanoparticles with average size of 17 nm, although with somewhat poor crystallinity. It is known that c-BN is a metastable phase that is difficult to synthesize. In our case, we believe that due to the unique conditions of high temperature and high pressure induced by the high-power laser ablation, it was be able to synthesis c-BN but with very poor crystallinity. It is important to note that peaks related to c-BN are not present in the as-synthesized materials. Thus, is because the poor crystallinity of the nanopowders and due to impurities of the nanopowders as mentioned in beginning (as there were chemi/physisorbed species).

6.3 Conclusion

Using submerged laser-induced plasma of boron bulk immersed in ammonia solution, we were be able to synthesize BN nanopowder. Upon heat treatment in an ammonia atmosphere (NH_3) at 1000 ^oC for 2hrs, the as-synthesized powder transforms to the more thermally-stable BN. XRD and TEM results indicate that there is a mixture of h-BN and c-BN.

References

(1) Albu, S. P.; Ghicov, A.; Macak, J. M.; Hahn, R.; Schmuki, P., Self-organized, free-standing TiO2 nanotube membrane for flow-through photocatalytic applications. *Nano letters* **2007,** 7, (5), 1286-1289.

(2) Gissler, W.; Haupt, J.; Hoffmann, A.; Gibson, P.; Rickerby, D., Mixed phase nanocrystalline boron nitride films: Preparation and characterization. *Thin Solid Films* **1991,** 199, (1), 113-122.

(3) Weissmantel, C.; Bewilogua, K.; Dietrich, D.; Erler, H.-J.; Hinneberg, H.-J.; Klose, S.; Nowick, W.; Reisse, G., Structure and properties of quasi-amorphous films prepared by ion beam techniques. *Thin Solid Films* **1980,** 72, (1), 19-32.

(4) Sainty, W.; Martin, P.; Netterfield, R. P.; McKenzie, D.; Cockayne, D.; Dwarte, D., The structure and properties of ion-beam-synthesized boron nitride films. *Journal of applied physics* **1988,** 64, (8), 3980-3986.

(5) Seidel, K.; Reichelt, K.; Schaal, W.; Dimigen, H., The preparation of cubic boron nitride films by reactive diode sputtering. *Thin Solid Films* **1987,** 151, (2), 243-249.

(6) Stout, C., *Plasma synthesis and HPHT consolidation of BN nanoparticles, nanospheres, and nanotubes to produce nanocrystalline cubic boron nitride*. ed.; 2017.

(7) Constant, G.; Feurer, R., Preparation and characterization of thin protective films in silica tubes by thermal decomposition of hexachloroborazine. *Journal of the Less Common Metals* **1981,** 82, 113-118.

(8) Uchida, H.; Yamashita, M.; Hanaki, S.; Kurihara, A., Synthesis of cBN films by ion mixing and vapor deposition technique. *Materials Science and Engineering: A* **2008,** 483, 695-697.

(9) Samantaray, C.; Singh, R., Review of synthesis and properties of cubic boron nitride (c-BN) thin films. *International Materials Reviews* **2005,** 50, (6), 313-344.

(10) Ichiki, T.; Momose, T.; Yoshida, T., Effects of the substrate bias on the formation of cubic boron nitride by inductively coupled plasma enhanced chemical vapor deposition. *Journal of applied physics* **1994,** 75, (3), 1330-1334.

(11) Feng, P.; Zhang, H., Properties of nanostructured cubic boron nitride films prepared by the short-pulse laser plasma deposition techniques. *International Journal of Refractory Metals and Hard Materials* **2009,** 27, (5), 823-828.

Chapter Seven

Conclusions and Future Work

The growing need to develop alternative sources of clean and renewable energy has become increasingly important recently. To satisfy increasing energy demand, photocatalysis has received attention because of its potential applications in environmental remediation and clean-energy production. Titanium dioxide has been reported as one of the most suitable semiconductor materials in a wide range of technology applications, such as photo-catalyst, because of photocatalytic activity through the irradiation of light at the surface. It has been embraced as an inexpensive, with high surface to volume ratio, and non-toxic material.

Titanium dioxide exists naturally in three crystalline phases: rutile, anatase, and brookite. Of the three, brookite is the only photochemically inactive one, and is unimportant in the field of photocatalysis from a reactivity standpoint. Anatase-TiO_2 is preferable for solar-cell applications because of its high electron mobility, low dielectric constant, and lower density. Anatase-TiO_2 also has a slightly higher Fermi level, a lower capacity to adsorb oxygen, and a higher degree of hydroxylation compared with other phases. These properties increase the photoactivity of TiO_2.

The remarkable physical and chemical properties of TiO_2 enable applications in many promising areas ranging from photovoltaics, photocatalysis, to sensors. TiO_2 is an

excellent photocatalyst because of its structural properties: first due to the valence band of TiO_2 is quite deep; second, the photon generated holes tend to locate on the surface of materials, which makes it easy to be harvested by free electrons from outside, that is, working as an oxidant agent. In term of sensors, TiO_2 is electron rich and belongs to n-type semiconductor. When gas absorbs onto the TiO_2 surface, it could release electrons into TiO_2, leading to the increase or decrease of resistance of TiO_2 materials. TiO_2- based gas sensor has been used for detecting gas or volatile such as H_2, O_2, CO, etc. In addition, it has been used for detecting soluble organics in water environment.

Due to the unique properties of TiO_2, tremendous interest has been shown in studies of TiO_2 nanomaterial synthesis and structure where the properties of TiO_2 are influenced by the crystal structure, surface area, band gap, crystallinity and surface hydroxyl group density. Different roots include hydrolysis precipitation, sol-gel, hydrothermal, flame synthesis are used to synthesis TiO_2. In all these methods, several variables must be considered, with one of the most important being particle size. Factors such as pH of the reaction medium, reaction temperature, natures of the solvent and additive, and reactivity of the metal alkoxide can affect the processing of TiO_2 nanostructures. In addition, various parameters, including flow rate, gas composition, deposition temperature, pressure, and deposition chamber geometry, can be controlled to have nano-forms of the desired TiO_2 material

Pulsed-laser ablation of a liquid phase has become a successful technique for synthesizing experimental quantities of nanostructured materials with various chemistries

and morphologies, including nanospheres, nanocubes, nanorods, and core-shell nanostructures. Laser ablation of solid target immersed in liquid offers some advantage in comparison to other techniques, such as chemical vapor deposition, vapor phase transport, hydrothermal synthesis, and sol-gel synthesis. These advantages include (i) forming phase-pure nanoparticles without by-products nor need for further purification, (ii) ease of experimental setup, and finally, (iii) unique conditions of high temperature, high pressure, and high density in the plasma-reaction zone to enable metastable phase formation.

Pulsed-laser decomposition of titanium tetra-isopropoxide (TTIP) is employed in this work to synthesis titania, and doped-TiO_2 nanoparticles. The laser is focused just below the surface of the liquid-metal-organic precursor, forming a high enthalpy submerged-plasma where precursor decomposition generates vaporized species, which upon subsequent rapid condensation/quenching yields metal-oxide nanopowder.

As-synthesized nanoparticles have non-crystalline or amorphous-like structures. Local compositional variations in the plasma-reaction zone, which are retained during rapid condensation/quenching of vaporized-precursor species, are believed to be responsible for amorphization of the nanoparticles because any significant deviation from the ideal stoichiometric composition of TiO_2 should inhibit its crystallization.

Upon post-annealing at 400ºC for 2 hours in ambient air, transformation of the amorphous-TiO_2 nanoparticles occurs, forming anatase-TiO_2 nanoparticles with little change in particle size. Apparently, at this temperature, there is sufficient atomic mobility to allow rearrangement of quenched-in Ti, O, and C species to form the more stable

anatase-TiO_2 phase. Because diffusion distances are small in nanoparticles, whatever their morphologies, it is not surprising that the amorphous-to-anatase TiO_2 transformation occurs at the relatively low temperature of 400ºC (~ 0.3 T_M). Upon post-annealing at 800ºC for 2 hours in air, anatatase-TiO_2 transforms rapidly to rutile-TiO_2.

After annealing at 400ºC, examination of nanopowder by scanning transmission electron microscopy (STEM) shows partially- and fully-transformed anatase-TiO_2 nanoparticles. Lattice imaging of a *fully-transformed nanoparticle* reveals a radially-symmetric nanograin structure, in which each nanograin is separated from its neighbor by a disordered region, probably containing a high density of edge dislocations to account for the observed tilt-angle between neighboring nanograins. Lattice imaging of a *partially-transformed nanoparticle* reveals a core-shell structure, in which the shell is transformed anatase-TiO_2 and the core is un-transformed amorphous-TiO_2. The shell component is similar in appearance to that of fully-transformed anatase-TiO_2. The core component appears amorphous-like, but upon closer examination at high resolution, there are regions where some degree of short-range ordering occurs.

It is concluded, therefore, that the amorphous-to-anatase phase transformation starts at the surfaces of the nanoparticles, irrespective of their morphologies, and propagates into the interior as in-situ reaction of trapped-in species likely yield gaseous products (e.g., CO, CH_4, H_2O) that diffuse out of the particles, leaving sufficient Ti and O to enable crystallization of anatase-TiO_2. In one remarkable case, such a diffusion-controlled transformation in a nanofiber appears to occur by propagation of anatase-TiO_2

layer-by-layer. Heat treatment was performed for different temperatures, Thermal gravimetric analysis (TGA) during annealing is recommended to determine the composition of a material or its thermal stability.

In this work, different ions, such as W, Mo, and V, are successfully doped into the structure of TiO_2 nanoparticles to enhance the photocatalytic properties of TiO_2. The ability the doping process to form an extended-solid solution phase of W, Mo, and V in the TiO_2 matrix may also be unique. The present work implies that other oxide phases, such as Al_2O_3, MgO and $MgAl_2O_4$, may be doped with normally insoluble metals, such as Pt and Ir. Such a possibility is of particular interest for catalytic applications, where post-annealing of the highly supersaturated metastable nanopowders may yield relatively stable nano-clusters on the surfaces of the oxide nanoparticles, thus rendering them more resistant to coarsening at elevated temperatures. Even though doping ions into TiO_2 structure has been demonstrated; the dopant ratio of the ions has not been confirmed. It has been found that when the doping ratio of the ions increase, the photocatalytic activity of TiO_2 increases as well. It could be recommended to use a soluble metals such as tungsten isoporoxide or tungsten trioxide and mix them with TTIP in order to verify the dopant ratio. In addition, it's interesting to try the co-doping metals into TiO_2 structure by using soluble metal such as tungsten isoporoxide or tungsten trioxide mixed with TTIP solution and use different solid metal such as Mo or Ag to produce W-Mo-doped TiO_2.

As an extension of the novel process to non-oxide systems, boron nitride (BN) powder is produced through pulsed laser ablation of boron bulk immersed in

ammonia/methanol solution. The unique conditions of high temperature, high pressure, and high species density in the plasma-reaction zone with rapid quenching enable amorphous and metastable phase formation. Current conditions yield short-range ordered BN structure. After heat treatment at 1000 ºC in an ammonia atmosphere, the mainly amorphous powder is transformed into h-BN and c-BN nanoparticles, albeit with low crystallinity. The hard BN phase is metastable phase and therefore would be expected to be depleted with increasing temperature in favor of the stable phase.

In summary, a submerged laser-induced plasma in precursor solution process has been developed to synthesize pure TiO_2; W-, Mo-, and V-doped TiO_2 with far-from-equilibrium nanostructures; and BN nanopowders. Potential advantages include the ability to synthesize a broad range of metal-doped ceramics with novel physical and chemical properties and the opportunity of a low-cost scalable robust process that does not required high vacuum equipment.